Advances in neutron optics for high resolution spectroscopy and applications in biologically inspired soft-matter physics

Tilo Seydel

UNIVERSITÉ JOSEPH FOURIER DE GRENOBLE

Habilitation à Diriger des Recherches

Discipline: Physique

présentée et soutenue publiquement par

Tilo SEYDEL

Advances in neutron optics for high resolution spectroscopy and applications in biologically inspired soft-matter physics

– A review –

préparée à l'Institut Max von Laue - Paul Langevin, Grenoble

soutenue le 1er décembre 2011

Composition du jury:

Rapporteurs:	Andreas MAGERL	-	Universität Erlangen-Nürnberg, Germany
	Stuart CLARKE	-	University of Cambridge, United Kingdom
	Theyencheri NARAYANAN	-	ESRF, Grenoble, France
Membre du jury:	Hervé JOBIC	-	IRCE de Lyon, Villeurbanne, France
Président:	Martin WEIK	-	IBS, Grenoble, France

Abstract

Incoherent cold neutron spectroscopy provides a unique non-invasive access to self-diffusion on nanometer length scales and time scales from several nanoseconds down to picoseconds. Combined with its high sensitivity to hydrogen atoms, neutron spectroscopy significantly contributes to the exploration of soft matter and biomaterials. Compared to synchrotron x-ray scattering experiments, neutron scattering experiments are more severely restricted by the available beam brilliance. The maximum achievable neutron source flux in the cold and thermal energy range is limited by first principles, and even future spallation neutron sources will "only" increase the source performance by one or two orders of magnitude compared to the best existing sources. Therefore, considerable effort is devoted to improving neutron spectroscopy instruments for an optimal use of the neutron source. State-of-the-art neutron optical components such as a ballistic neutron guide, and a phase space transformer (PST) based on moving mosaic crystals are reviewed in the context of the future new backscattering spectrometer IN16B at the Institut Laue-Langevin (ILL). The improvement of neutron spectrometers renders new types of experiments feasible. Following a detailed description of the neutron backscattering technique in the context of complementary methods, a brief overview of various recent applications of cold neutron spectroscopy is provided. Some examples in the fields of polymer as well to macromolecular colloid physics are subsequently discussed in more detail. These examples point to the perspective of new insights to be gained by new spectrometers in the future. One example addresses silk fibres, which are mechanically outstanding nanostructured protein polymer fibres. Neutron spectroscopy on different time- and length scales, in part combined with *in situ* tensile tests, contributes to an understanding of the mechanical properties of silk fibres. Another example deals with model globular proteins in aqueous solution as highly monodisperse colloidal suspensions. A particular interest thereby focuses on the effect of molecular crowding and the effect of charges on the molecular mobility. These and other examples illustrate the unique information obtained by neutron spectroscopy. They also point to future perspectives with new soft matter sample environments, allowing for instance for *in situ* tensile testing and *in situ* optical spectroscopy.

"The effect was as if he had twisted the entire world through a billionth part of a billionth part of a degree. Everything shifted, was for a moment minutely out of focus, and then snapped back again as a suddenly different world."

The long dark tea-time of the soul, chapter 24 [2].

Preface

Understanding diffusion on molecular length scales is essential to understand interaction and, thus, to understand function in almost any soft-matter system, be it a liquid, a glass-forming system, a colloidal suspension or gel, a polymer, a membrane, or a biological system. The ongoing effort to improve experimental methods exploring diffusion on molecular length scales is therefore considerable. This effort emerging mainly from soft-matter science has strong implications in the distant fields of the advancement of neutron optics and also engineering and induces significant capital investment. In return, new studies are inspired regarding diffusion in systems that require an ever increasing accuracy in the information on diffusion. It appears timely to attempt a small review of new developments in high-resolution neutron spectroscopy, which is a technique optimized to study diffusion on molecular length scales, in the context of example scientific questions and future perspectives. This holds in particular, since the Institut Laue-Langevin has committed itself to provide one of the best sub-μeV resolution cold neutron spectrometers by building the new instrument IN16B. Neutron optics has moved forward during the several years devoted to this project, since the optimum speed of the so-called phase space transformer has been better understood. In addition, the complex interplay of an approximately "ballistic" neutron guide, a neutron velocity selector, an elliptical focus guide, and the phase space transformer itself were optimized for this new spectrometer. It is emphasized that this type of spectrometer of course not only serves soft-matter science in its broadest definition, and it not only measures diffusion, but also for instance quantum rotational tunneling in suitable crystals. The instrument is also a tool to determine thermal Debye-Waller factors, i.e. a characteristic quantity of the phonon spectrum, in almost any system, and to detect glass and melting transitions, as well as molecular adsorption on surfaces. Further, it serves other types of experiments which require an accurate energy definition at scattering vectors suitable to retrieve information on molecular length scales. For the new instrument, state-of-the-art mechanical engineering reaches its limits at several moving optical components, namely the neutron velocity selector, the phase space transformer, and the moving monochromator Doppler drive.

With the present review, the author intends to put a number of publications which he co-authored in a context of perspectives for future work. Most figures have been taken from these publications. The chapters 5 and 6 contain parts of the articles [18, 56, 72, 167] on instrument developments, which were co-authored by the author of the present review, in an abbreviated and adapted form. Notably, several publications which are discussed within a broader scope in this brief review – including amongst others [72, 134, 135, 138, 143] – emerged in the context of the author's activity in co-supervising thesis students.

Contents

List of abbreviations

BASIS	-	Time-of-flight backscattering spectrometer at the Spallation Neutron Source
BATS	-	Backscattering and time-of-flight spectroscopy
DLS	-	Dynamic light scattering
EISF	-	Elastic Incoherent Structure Factor
ESRF	-	European Synchrotron Radiation Facility, Grenoble, France
FG	-	Focusing Guide
FWHM	-	Full width at half maximum
H112	-	Neutron guide serving IN16B
HR	-	High Resolution (spectroscopy)
ILL	-	Institut Max von Laue - Paul Langevin, Grenoble, France
IN10	-	"First generation" cold neutron backscattering spectrometer at the ILL
IN13	-	"First generation" thermal neutron backscattering spectrometer at the ILL
IN16	-	"Second generation" cold neutron backscattering spectrometer at the ILL
IN16B	-	Cold neutron backscattering spectrometer built at the ILL within the Millennium Programme for instrument renewal
McStas	-	Neutron ray-tracing simulation package (www.mcstas.org)
NMR	-	Nuclear Magnetic Resonance
PST	-	Phase Space Transformation
QENS	-	Quasi-elastic neutron scattering
SNS	-	Spallation Neutron Source, Oak Ridge National Laboratory, USA
TOF	-	Time-of-Flight (spectroscopy)
VCS	-	Vertical Cold Source - one of the two cold neutron moderators at the ILL
XPCS	-	X-ray photon correlation spectroscopy

Mathematical notation and symbols

φ	-	volume fraction of colloids/proteins in solution
D	-	diffusion constant
$\mathbf{k}$	-	wave vector
ω, E	-	energy transfer
Ω	-	solid angle
$\mathcal{R}(\omega)$	-	spectrometer resolution function
$\mathbf{q}$, $\mathbf{Q}$	-	scattering vector (synonymous representations)
$S(\mathbf{q}, \omega)$	-	dynamic scattering function accessible by neutron spectroscopy
σ	-	scattering cross section
T	-	temperature
$\langle u^2 \rangle$	-	atomic vibrational mean squared displacement
$\otimes$	-	convolution

Chapter 1

Introduction

Neutron spectroscopy accesses spatial and time correlations by measuring the van Hove scattering function $S(\mathbf{q},\omega)$ [96, 154, 168] depending on the scattering vector $\mathbf{q}$ and energy ω. Incoherent neutron spectroscopy can be used to obtain the self-diffusion on nanometer length scales [170]. The absence of alternative non-invasive techniques to for instance probe self-diffusion with a high sensitivity to the hydrogen atom predominant in soft matter justifies the considerable cost of neutron spectroscopy. Neutron spectroscopy also provides unique information on spatial restrictions to which diffusion processes may be confined on nanometer length scales through the elastic incoherent structure factor [12, 13]. From this information models of the geometry of confined motions may be derived.

Amongst the most frequently used neutron spectroscopy techniques are cold neutron time-of-flight spectroscopy accessing picosecond time scales and cold neutron backscattering accessing nanosecond time scales. Both techniques access the spatial and time correlations by measuring $S(\mathbf{q},\omega)$ at scattering vectors $\mathbf{q}$ corresponding to nanometer length scales. Time-of-flight and backscattering spectrometers in the absence of polarisation analysis measure both coherently and incoherently scattered neutrons. In the case of samples rich in hydrogen atoms, the incoherent scattering is dominant and the self-diffusion of the scattering atoms can be extracted from $S(\mathbf{q},\omega)$. The complementary neutron spin-echo technique accesses the intermediate scattering function $S(\mathbf{q},t)$ in time t which is similar to the observable in visible and x-ray photon correlation spectroscopy techniques.

Neutron spectroscopy techniques provide information on molecular motion and complement experiments which solely address structural properties. Through the aforementioned concept of the elastic incoherent structure factor [12, 13], neutron spectroscopy in addition contributes information on the local order of soft matter samples. By contrast, diffraction techniques are sensitive to long-range order, which is mostly absent in soft matter. Neutron spectroscopy techniques are mostly applied to relatively large samples with masses on the order of 100 mg in the case of polymers, biological samples or other hydrogen-rich materials. The techniques can also be made sensitive to surfaces and interfaces if these are sufficiently large. This is the case for example for large stacks of surfaces as well as for nanoporous or powder materials with large effective surfaces. The impact of neutron spectroscopy on the study of surface diffusion and catalysis is evident from this option.

The information on molecular motion is essential to for instance understand biological function such as membrane function and molecular transport processes and dynamics-function relationships in soft matter in general. Diffusion is of great interest for the understanding of biological interactions and interaction time scales as well as the transport of information. Diffusion is also important to comprehend the dynamic precursor processes of aggregation from aqueous solution in biological systems, which may occur by way of the

charge-controlled formation of transient clusters. In brief, understanding diffusion is essential to understand interaction. Incoherent neutron scattering thereby provides a unique access to self-diffusion processes as opposed to collective diffusion. The latter, by contrast, is routinely accessed by photon correlation spectroscopy methods which detect nearest-neighbor correlations in colloidal suspensions through the transverse coherence of the impinging radiation. Collective diffusion can also be detected by the neutron spin-echo method where an analog situation to the large transverse coherence of the incident radiation is achieved by the spin-encoding of the incident neutrons. The unique access to self-diffusion is essential to study interactions of diffusing particles with their surrounding media.

The scattering theory underlying the interpretation of quasi-elastic and inelastic neutron scattering experiments has been elaborated some decades ago. This also applies to the standard concepts of neutron instruments. Modern developments, by contrast, concern the enhancement of neutron spectrometers through progress in neutron optics, and of neutron sample environments to broaden the fields of application of neutron spectroscopy. Further, modern theory in neutron spectroscopy aims at understanding diffusion, and although the scattering theory appears to be complete, this does not apply to the theory of diffusing particles in complex systems such as colloidal suspensions or diffusion in geometrical confinement. Whilst neutron time-of-flight spectrometers can access both relatively fast picosecond time scale diffusion processes as well as phonons, high-resolution spectrometers are optimized to study slower diffusion processes which are of great importance in colloid and polymer physics. It is the purpose of the present review to summarize recent instrument and sample environment developments with particular emphasis on high-resolution cold neutron backscattering, and to provide examples of application and future perspectives in bio-related soft matter science. Unprecedented accuracy in the data acquisition will be required to understand diffusion in complex media such as colloidal suspensions, which are extremely sensitive to environmental parameters such as ionic strength and charge distributions. The same necessity of a high experimental accuracy holds when for example minute changes in the molecular diffusion have to be recorded as a function of other external parameters such as the tensile strain applied to polymer fibers, or when the effect of different types of lipid molecules on the fluctuation spectrum of a lipid membrane is to be studied.

The present review is organized as follows: In chapter 2, basic concepts of diffusion relevant for interpreting neutron spectroscopy data will be briefly visited, followed in chapter 3 by an introduction to basic concepts in high resolution neutron spectroscopy and their brief comparison to complementary techniques. These first two chapters are kept extremely concise to conform with the spatial restrictions of this small review. Special emphasis will then be given to the high resolution neutron backscattering technique in chapter 4. This backscattering technique will be implemented in the future spectrometer IN16B at the ILL and will benefit from recent advances in neutron optics summarized in the chapter 5 – addressing in particular the Phase Space Transformation technique – and chapter 6 – addressing other state-of-the-art neutron optical components. Subsequent to these two chapters discussing the neutron optics implemented in IN16B, the chapter 7 deals with new sample environments for an *in situ* combination of neutron spectroscopy and other experiments on soft matter samples. Chapter 8 presents recent, current, and future examples of application of neutron backscattering. Chapter 9 closes this small review with an attempt of a view to the future.

Chapter 2

Concepts in diffusion

The article on Brownian motion [21] by A. Einstein [44] has been cited more frequently [85] than his more famous papers on special relativity [46] and the quantum nature of light [45] which appeared in the same year 1905. This observation underlines the importance of understanding diffusion and general random concepts of motion [107]. Brownian diffusion can be seen as overdamped motion driven by thermal fluctuations in a solvent medium. In modern physics, the concepts of Brownian diffusion have been extended to include so-called anomalous diffusion processes such as subdiffuion and superdiffusion [85]. Recent research has also addressed the "hydrodynamic memory" [51] arising from a diffusing particle acting back on its solvent. Historically, the mathematical description of diffusion goes back to A. Fick [49]. According to Fick's second law, diffusion can be written analogously to the heat equation as a concentration field which changes with time as

$$\frac{\partial \rho}{\partial t} = D \bigtriangledown^2 \rho, \tag{2.1}$$

where ρ is the particle concentration and D the diffusion constant.

High-resolution neutron spectroscopy techniques are the ideal tool to study diffusion on molecular length scales. Due to the existence of spin and isotope incoherent and coherent neutron scattering, neutrons can probe both self- and collective diffusion phenomena. In the present chapter only the most prominent terms and definitions regarding diffusion will be reviewed, mostly restricting the discussion to simple Brownian motion and extensions for confined geometries [12] and crowded colloidal suspensions [11]. For more detailed considerations we refer to the textbooks such as Refs. [34, 133].

2.1 Equation of motion: the Langevin equation

The classical Newton equation of motion can be generalized to describe diffusion in a many-particle system by introducing a time-dependent stochastic force term $F_{\text{fluct}}(t)$ [90]. The Newton equation for a particle with velocity v is then written as

$$\dot{v} + \alpha v = \Gamma(t) \tag{2.2}$$

with $\alpha = \frac{-\gamma}{m}$ and $m\,\Gamma(t) = F_{\text{fluct}}(t)$, where $\gamma = 6\pi\eta_0 a > 0$ is a constant accounting for the drag experienced by the diffusing particle with radius a and mass m in the system (solvent) with viscosity η_0. The stochastic force $F_{\text{fluct}}(t)$, denoted Langevin force, can mostly be written as a delta-correlated function with zero mean and the fluctuation strength ξ

$$\langle \Gamma(t) \rangle = 0, \quad \langle \Gamma(t)\,\Gamma(t') \rangle = \xi\,\delta(t - t'). \tag{2.3}$$

Importantly, the solution of the Langevin equation 2.2,

$$v(t) = v_0 \, \exp(-\alpha t) \, + \, \int_0^t dt' \, \exp(-\alpha(t-t'))\Gamma(t') \tag{2.4}$$

with the initial condition $v_0 = v(0)$, gives rise to the definition of the so-called mean-squared displacement

$$\begin{aligned} W(t) &= \frac{1}{2d} \left\langle (r(t) - r(0))^2 \right\rangle = \frac{1}{2d} \int_0^t \int_0^t dt_1 \, dt_2 \, \langle v(t_1) v(t_2) \rangle \\ &= \frac{1}{2d} \frac{\xi}{\alpha^2} t \left(1 - \frac{(1 - \exp(-\alpha t))}{\alpha t} + \frac{(1 - \exp(-\alpha t))^2}{2\alpha t} \left(\frac{2\alpha}{\xi} \, v_0^2 - 1 \right) \right). \end{aligned} \tag{2.5}$$

Therein, r is the particle position and d the dimension of the system. For $t \longrightarrow \infty$, eq. 2.5 reduces to $W(t) = D_0 t$ with the Brownian diffusion coefficient

$$D_0 = \frac{\xi}{2d\alpha^2} = \frac{k_B T}{\gamma}. \tag{2.6}$$

In equation 2.6 we recognize the well-known Stokes-Einstein relation, assuming that the relation between ξ and γ is given by the equipartition theorem of classical mechanics [133]. For all systems studied with cold and thermal neutron scattering, the above non-relativistic descriptions are entirely sufficient. (Relativistic generalizations of diffusion are subject to ongoing research [43].)

2.2 Diffusion equation: the Smoluchowski equation

The diffusion in general is governed by the Smoluchowski equation [173] which is also known as Fokker-Planck equation and describes the propagation of the probability density function in time, assuming inertia-free particles,

$$\frac{\partial P(\mathbf{r}, t)}{\partial t} = \hat{\mathbf{L}}_{\mathrm{S}} P(\mathbf{r}, t) \tag{2.7}$$

with the probability density function $P(\mathbf{r}, t)$ and the Smoluchowski operator $\hat{\mathbf{L}}_{\mathrm{S}}$ acting on the function $\mathcal{F}$ through

$$\hat{\mathbf{L}}_{\mathrm{S}}(\mathcal{F}) = \bigtriangledown D(\mathbf{r}) \, \left[\beta \left[\bigtriangledown U(\mathbf{r}) \right] (\mathcal{F}) + \bigtriangledown (\mathcal{F}) \right]. \tag{2.8}$$

Therein, $\beta = k_B T$, $\mathbf{r}$ is the vector of all particle coordinates, $U = U(\mathbf{r})$ is the potential energy of the system, and $D(\mathbf{r})$ is the diffusion tensor. The Smoluchowski equation provides more information on the diffusion in a system compared to the Langevin equation, since it in principle allows to calculate ensemble-averaged macroscopic system parameters such as correlation functions which are directly accessible to for instance scattering experiments.

2.3 Self-diffusion

Self-diffusion – synonymously denoted tracer diffusion – is the diffusion of an individual particle seen when disregarding the correlations with surrounding particles, i.e the diffusion of an individual particle through the environment consisting of a solvent and/or other particles. Neutron time-of-flight and backscattering spectroscopy techniques provide access to the incoherent scattering function $S_{\mathrm{inc}}(Q, \omega)$ from hydrogen-rich soft-matter and bio-related samples. $S_{\mathrm{inc}}(Q, \omega)$ contains information on the ensemble-averaged single-particle correlation function of the hydrogen atoms (see figure 2.1). When diffusion is present in the sample, $S_{\mathrm{inc}}(Q, \omega)$ thus accesses the self-diffusion.

2.4 Collective diffusion

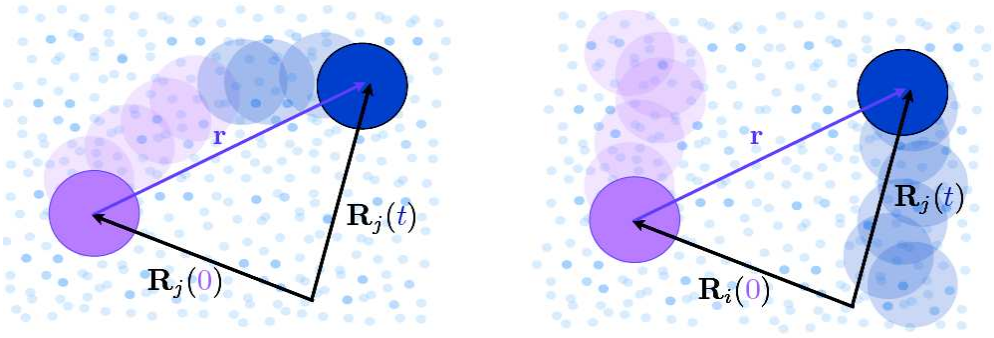

Figure 2.1: Sketch illustrating the difference between collective difusion and self-diffusion: To determine the self-diffusion (left), the single-particle self-correlation function of the spatial coordinate $\mathbf{R}_j(t)$ for particle j is measured and the ensemble average is taken. Using neutrons, this is achieved by recording the incoherent scattering. For collective difusion, the particle-particle correlation function of the particles with the coordinates $\mathbf{R}_i(t), \mathbf{R}_j(t)$ is measured and the ensemble average is taken. Using neutrons, this is achieved by recording the coherent scattering. (Figure from [71])

The isothermal relaxation of the particle density function $\rho(r,t)$ to equilibrium is denoted collective diffusion. Formally, the collective diffusion coefficient $D_c(r,t)$ is introduced through the solution of the continuity equation

$$\frac{\partial \rho(r,t)}{\partial t} = - \bigtriangledown j(r,t) \tag{2.9}$$

with the particle flux $j(r,t)$,

$$j(r,t) = - \int dr' \int_0^t dt' \, D_c(r-r', t-t') \bigtriangledown \rho(r',t'). \tag{2.10}$$

Collective diffusion can be measured with coherent neutron scattering for $Q \longrightarrow 0$, or for suitable systems with dynamic light scattering, which automatically fulfills $Q \longrightarrow 0$.

2.5 Diffusive time scales, short-time and long-time diffusion

When models for diffusion are considered, time scales have to be observed which restrict the applicability of these models.

Free or Brownian diffusion leads to a mean squared displacement $W(t)$ linear in time,

$$W(t) = 6 \, D_{\text{app}} \, t, \tag{2.11}$$

with an apparent diffusion constant D_{app}. For interacting particles such as colloid particles dispersed in an aqueous solution, equation 2.11 still holds on sufficiently short time scales τ such that

$$\tau_D \ll \tau \ll \tau_I = \frac{a^2}{D_0}, \tag{2.12}$$

where a is the radius of the particle and D_0 is the dilute-limit diffusion constant. $\tau_D = M\,\gamma$ with the particle mass M and the friction parameter γ defines the diffusive time scale above which diffusive motion takes place. Diffusion when equation 2.12 holds is termed short-time diffusion. In the short-time regime, the diffusing particle does not encounter neighboring particles through collisions and only reacts to its environment via hydrodynamic interactions [11]. For $\tau \gg \tau_I$, long-time diffusion is observed, which is governed by both hydrodynamic and direct interactions, i.e. for instance by particle collisions.

For particles with the size of a few nanometers radius in aqueous solution, the high-resolution neutron backscattering technique accesses the short-time self-diffusion regime, making it a unique tool to for instance study interactions in protein solutions.

2.6 Rotational diffusion

Particles in solution undergo both translational and rotational diffusion. From a formal point of view, the models of diffusion may be extended to include rotational diffusion by including angular coordinates. Thus, in Fick's law (equation 2.1) for rotational coordinates the $\bigtriangledown^2$ operator is written in the spherical angles Θ and Ψ

$$\bigtriangledown^2 = \frac{1}{\sin\Theta}\frac{\partial}{\partial\Theta}\left(\sin\Theta\,\frac{\partial}{\partial\Theta}\right) + \frac{1}{\sin^2\Theta}\,\frac{\partial^2}{\partial\Theta^2}. \tag{2.13}$$

The development of the theory for the rotational and translational diffusion of non-spherical objects has been initiated by F. Perrin [116, 117] by introducing hydrodynamic friction factors known as Perrin factors.

2.7 Confined diffusion

Incoherent quasi-elastic neutron scattering is often used to explore diffusion in confined geometries. Thereby, the dependence of the ratio of the elastic scattering and the quasi-elastic scattering on the scattering vector $\mathbf{q}$ gives information on the geometry to which a diffusing particle is confined [12, 13]. This so-called elastic incoherent structure factor (EISF) is an important observable to quantify spatially confined diffusion. As stated in the introduction, the concept of the EISF thereby provides information on the local order of a system as opposed to long-range order. Pioneering work in modeling such confinement has been carried out by Volino and Dianoux [171] who provided an analytical framework to describe the diffusion of a particle inside a potential of spherical geometry. The investigation of dynamics in confinement has thus triggered an entire field of research, applying QENS to a multitude of different complex systems [14, 104]. For the first time, deviations from simple Brownian diffusion have been observed in the neutron scattering signals from simple fluids and quantified by the introduction of the jump-diffusion model [151, 27] which was subsequently applied with significant success to the description of the self-diffusion of water molecules which takes place on picosecond time scales at ambient conditions [160, 126], but also to hydrogen atoms interstitiated in Palladium crystals and diffusing on up to nanosecond time scales [24]. At present, the diffusion of adsorbed water in geometrical confinement is frequently investigated in polymer and biomaterials science [15]. A recent example addresses the effects of tensile deformation on the confinement geometry of adsorbed water in silk fibers [143] (see also section 7.2).

Chapter 3

High resolution neutron spectroscopy in the context of complementary techniques

Within a few decades from the experimental confirmation of the existence of the neutron [25], the first neutron scattering experiments were carried out at fission reactor neutron sources [176], neutron spectroscopy was introduced [20], and finally, neutron spectroscopy at a very high energy resolution was proposed [99]. Using cold neutron scattering, energy resolutions on the order of 1 μeV FWHM can routinely be achieved. This is due to the low energy of cold neutrons on the order of 2 meV, such that a 1 μeV energy resolution only requires an energy definition $\Delta E/E \approx 1/2000$.

Using high-resolution neutron spectroscopy, diffusion is observed through a broadening of the elastic scattering signal. This broadening, denoted quasi-elastic scattering [170], in general depends on the scattering vector. Quasi-elastic neutron scattering can for example be used to measure the molecular diffusion of water [160]. High resolution neutron spectroscopy can further be applied to determine the hydrodynamic radius of nanometer scale colloid particles in solution via their diffusion and the Stokes-Einstein relation even for opaque samples. By contrast, dynamic light scattering only accesses diffusion in dilute solutions that are transparent to light and cannot reach molecular length scales. Small-angle scattering can in principle also access information related to the hydrodynamic radius of a colloid particle, but it is not possible to separate the structure factor and form factor of particles with a complex shape in a model-free approach by this method. An important asset of thermal and cold neutron techniques is that radiation damage to the samples is entirely circumvented, because the neutron energy is several orders of magnitude below the energy required for ionization. Also, the thermal heat load of the neutrons can be neglected in this context. A further asset is that both coherent and incoherent scattering occur, depending on the nuclear isotope composition of the sample.

The size of all neutron instruments is essentially determined by the length it takes to moderate a neutron emerging with an energy of the order of 10^6 eV from a fission or spallation process down to a few 10^{-3} eV. The size of a typical moderator is several 10^{-1} m, and the typical spot diameter on the surface of a moderator illuminating any sample in a neutron instrument is 10^{-1} m. In neutron spectrometers, this spot size is usually focused down to approximately $3 \cdot 10^{-2}$ m in diameter, corresponding to the size of the sample. In the design of neutron spectrometers, an optimum compromise between beam divergence, i.e. angular information, and beam intensity is pursued. To best match the finite sample size and beam divergence effects and record the best possible angular information, the standard sample-to-

detector or sample-to-analyzer crystal distance is of the order of 2 m. The latter distance is also important to separate neutrons with different speeds according to their arrival time at a detector in time-of-flight spectrometers (see the next section). These fundamentals define the physical appearance of neutron spectrometers.

3.1 Neutron time-of-flight spectroscopy

Due to the low speed of thermal and cold neutrons, which is on the order of magnitude of the speed of sound in ambient air, the energy dispersion of neutrons can simply be detected by their flight time over a given path length. This type of neutron spectroscopy experiment and the feasibility of recording quasi-elastic neutron scattering with it has been pioneered by B. Brockhouse in the 1950ies [20]. Technically, the recording of the time can be achieved using pulsed beams generated by rotating chopper disks. Neutron time-of-flight spectroscopy is a convenient method to obtain the scattering cross section of a sample in time t and solid angle Ω, $\frac{\partial^2\sigma}{\partial\Omega\partial t}$, which is related to the scattering function through

$$S(\Omega,\omega) \propto \frac{k_i}{k_f}\frac{\partial^2\sigma}{\partial\Omega\partial\omega} \propto t^4\,\frac{\partial^2\sigma}{\partial\Omega\partial t}. \tag{3.1}$$

With the time-of-flight method using cold neutrons, the typical scattering vector range $0.4\,\text{Å}^{-1} < Q < 2.5\,\text{Å}^{-1}$ can be explored with an energy resolution of approximately 80 to 100 μeV FWHM.

3.2 Neutron spin-echo techniques

The neutron spin-echo technique can be seen as a time-of-flight technique with an improved precision on the flight time determination. This precision is achieved by using the neutron spin precession to encode for the flight time [106]. Essentially, the incoming polarized neutron beam travels through a magnetic field upstream from the sample, and the elastic energy is defined by a certain number of spin precessions which the neutrons undergo during this operation. An elastic scattering process is then detected by an equivalent operation inversed in time following the sample, where the elastically scattered neutron arrives with the original polarization. Conversely, an inelastic scattering process is measured by a change in the polarization of the detected neutron. Importantly, the method only detects velocity changes and not absolute neutron velocities, and the information on these velocity changes can be used to obtain the intermediate scattering function $I(Q,t)$ of the sample, which is related to the scattering function $S(\mathbf{q},\omega)$ through a Fourier transform. The method has some distant resemblance to interferometry, and the idea of exploiting spin precessions alludes to nuclear magnetic resonance experiments (subsection 3.6). Since no absolute neutron velocity needs to be measured, the instruments can operate with a relatively broad incident wavelength distribution $\Delta\lambda/\lambda \approx 0.1$ for the benefit of the neutron flux. The maximum accessible relaxation times of diffusion processes in the samples exceed several 100 ns [48].

3.3 Triple-axis neutron spectroscopy

Triple axis spectrometers are crystal monochromator and analyzer spectrometers where these crystals are mounted on movable axes to define pairs of wave vectors $(\mathbf{k}_i, \mathbf{k}_f)$ where the scattering intensity is recorded. The three axes of rotation are given by the monochromator,

sample, and analyzer. These spectrometers are well suited for single-crystal studies due to the very high precision in the definition of the scattering vector. They serve for example to explore phonons. Standard (Q, ω)-ranges explored by cold neutron triple axis instruments are similar to those explored by time-of-flight spectrometers.

3.4 Neutron backscattering

Neutron backscattering is equally a crystal monochromator and analyzer technique which can be seen as a limiting case of the triple-axis technique in that the incidence of the neutrons on both the monochromator and analyzer crystals is always in the crystal normal direction. Here, the energy resolution routinely reaches $1\,\mu$eV FWHM or an even better value, covering the typical scattering-vector range $0.4\,\text{Å}^{-1} < Q < 2\,\text{Å}^{-1}$. The high energy resolution comes at the cost that compared to time-of-flight spectrometers, the maximum detectable energy transfer range is severely restricted. Similar to the case of time-of-flight spectrometers, in standard operation the neutrons are detected in parallel for the entire accessible scattering angle range by using a detector array. No polarization analysis takes place in this standard operation, i.e. both coherently and incoherently scattered neutrons are recorded. Further details will be reviewed in the following chapter.

3.5 Photon correlation spectroscopy

Photon correlation techniques using coherent light sources access dynamic information by measuring the speckle fluctuation on the illuminated sample giving rise to an intensity autocorrelation function in time

$$g_2(t) = \frac{\langle I(t+t_0)\, I(t_0)\rangle}{\langle I\rangle^2}. \tag{3.2}$$

The coherent light source can be a visible or X-ray light source, and the advantage of X-ray light sources is that large scattering vectors can be accessed and that opaque samples may be probed. g_2 is related to the intermediate scattering function $S(q,t)$ by the Siegert relation [93]

$$g_2(q,t) = 1 + \beta(q)\ |S(q,t)|^2\,, \tag{3.3}$$

where $\beta(q)$ is the speckle contrast. Photon correlation spectroscopy in the x-ray range (XPCS) has been pioneered during the 1990ies [37, 162, 108, 63]. The future development of XPCS techniques will be strongly influenced by the advent of free electron laser x-ray sources [81]. These x-ray sources are characterized by a sub-picosecond time structure, and one of their main goals is to enable ultrafast x-ray science. XPCS at free-electron laser sources will often be combined with delay-line techniques to increase the dynamic range of XPCS [65]. Another technique related to photon correlation spectroscopy is fluorescence correlation spectroscopy, which is often applied in biochemistry to record "tracer" diffusion using fluorescence markers [163].

Photon correlation spectroscopy using visible laser light, known is dynamic light scattering (DLS), is a standard laboratory technique to measure diffusion in colloidal suspensions, including protein solutions. Like neutron scattering, it does not create radiation damage. DLS, like XPCS, can be used to measure collective diffusion. It is extremely useful to determine diffusion constants in dilute solutions which are not accessible to neutron spectroscopy. By contrast, highly concentrated, opaque suspensions cannot easily be probed

using DLS. For instance, applying standard multi-angle DLS, the highest protein concentration of Bovine Serum Albumin in water which was safely accessible has been found to be around 150 mg/ml [68]. Comparing photon correlation to neutron spin echo experiments, it is noted that both methods access collective diffusion in particle suspensions through coherent scattering. Photon correlation is based on photon statistics and therefore is an intrinsically "photon hungry" technique. The faster the time scale to be observed, the higher the photon flux needs to be. By contrast, in neutron spin echo spectroscopy the observable is determined by polarization analysis rather than intensity autocorrelation.

3.6 Nuclear magnetic resonance

Nuclear magnetic resonance (NMR) experiments are based on recording the response of the nuclei in a sample to an externally applied radio frequency. For this purpose, the nuclear spins are aligned using a magnetic field. Modern NMR is a highly sophisticated technique which cannot be addressed in any detail in the present concise review and is only mentioned for completeness. Intrinsically, it detects angular correlation functions rather than spatial correlation functions, whilst the latter are accessible to neutrons. It is noted that NMR can be seen as a scattering technique in terms of a suitable coordinate transformation [50]. In practical terms when addressing for instance *in situ* combinations with other experiments (cf. chapter 7), we emphasize the necessity to apply an external magnetic field and in some cases the necessity to rotate the sample during an NMR experiment (magic angle spinning NMR). These requirements impose geometrical restrictions in NMR experiments. By contrast, geometrical restrictions are in general less severe in neutron experiments, where samples can usually be accessed *in situ* from above and below the scattering plane.

Similar to neutron scattering, NMR can provide both structural and dynamic information on a molecular level, and it also does not induce radiation damage in samples. NMR detects self-correlation functions of spins and can therefore measure self-diffusion. Due to the accessible time scales, for nanoscale colloid particles such as proteins in solution this self-diffusion is typically recorded in the long-time limit [95] (cf. section 2.5). Hence, NMR complements neutron backscattering, which can access the self-diffusion in the short-time limit on such samples [135]. It also complements dynamic light scattering which can detect collective diffusion in the long-time limit.

3.7 Raman scattering

With view at the interest in characterizing soft-matter samples *in situ* not only with neutrons but also using Raman scattering (see section 7.1), we briefly mention this technique here. Raman scattering is an inelastic light scattering technique which relies on illuminating the sample with intense monochromatic light usually originating from a laser source [60]. From the wavelength shift of the scattered light, molecular vibrations can be detected. Raman scattering is related to vibrational spectroscopy using neutrons. Due to the long wavelength of the radiation, Raman scattering does not provide accurate Q-information, i.e. it is restricted to the center of the Brillouin zone in crystallographic terms. From the experimental point of view, it is a quite robust technique which can be carried out in a near-backscattering geometry. For this reason, it is suitable for a combination with neutron spectroscopy (see section 7.1). One of its drawbacks is the thermal heat load which the laser light source imposes on the sample.

Chapter 4

Concepts for high resolution backscattering spectroscopy

Amongst the cold neutron spectroscopy techniques, backscattering from perfect crystals achieves a particularly high resolution in energy. Backscattering was invented during the late 1960ies [4, 16, 99] and developed into an established spectroscopy method during the following decades [67]. A review of the history and basic principles of the technique can be found on the backscattering web site by B. Frick and A. Heidemann [54]. Notably, backscattering is a special case of the triple-axis spectroscopy technique which uses single crystals to define both the incident wave vector $\mathbf{k}_i$ and the wave vector $\mathbf{k}_f$ at which scattered neutrons are recorded. Neutron backscattering is a highly specialized technique with only on the order of 10 instruments of this type being operational worldwide.

4.1 Basic idea

The backscattering technique is based on the observation that the highest definition of a wavelength λ using a single crystal is achieved at a Bragg angle [19] $\Theta = 90°$, as in this case the error obtained from the first derivative of the Bragg equation

$$\frac{\Delta\lambda}{\lambda} = \frac{\Delta\Theta}{\tan\Theta} + \frac{\Delta d}{d} \tag{4.1}$$

attains a minimum due to the divergence of $\tan\Theta$. Therefore, only the error in the lattice spacing d of the monochromator crystal remains, which is related to the Darwin width [30, 31]. A setup implementing an inelastic scattering experiment with highest energy resolution using this observation requires both a monochromator and an analyzer crystal to be aligned in exact backscattering. In this case, unlike on triple-axis spectrometers, the tuning of the Bragg angle of the crystals is no longer available as a degree of freedom to define the scattering vectors and thus to scan the energy transfer. On current reactor-based backscattering spectrometers, the scan of the monochromator Bragg angle is replaced by either a mechanical Doppler shift or a detuning of the lattice constant through a temperature change [29]. Both the Doppler shift and the temperature change alter the length of $\mathbf{k}_i$, and $\mathbf{k}_f$ is always recorded at fixed length but at various angles simultaneously given by the static analyzer crystals (figure 4.1). During the late 1960ies and early 1970ies, so-called first-generation backscattering instruments such as IN10 and IN13 at the ILL allowed for a slight deviation from exact backscattering on the order of 2° to geometrically separate the beams incident on and returning from the monochromator crystal.

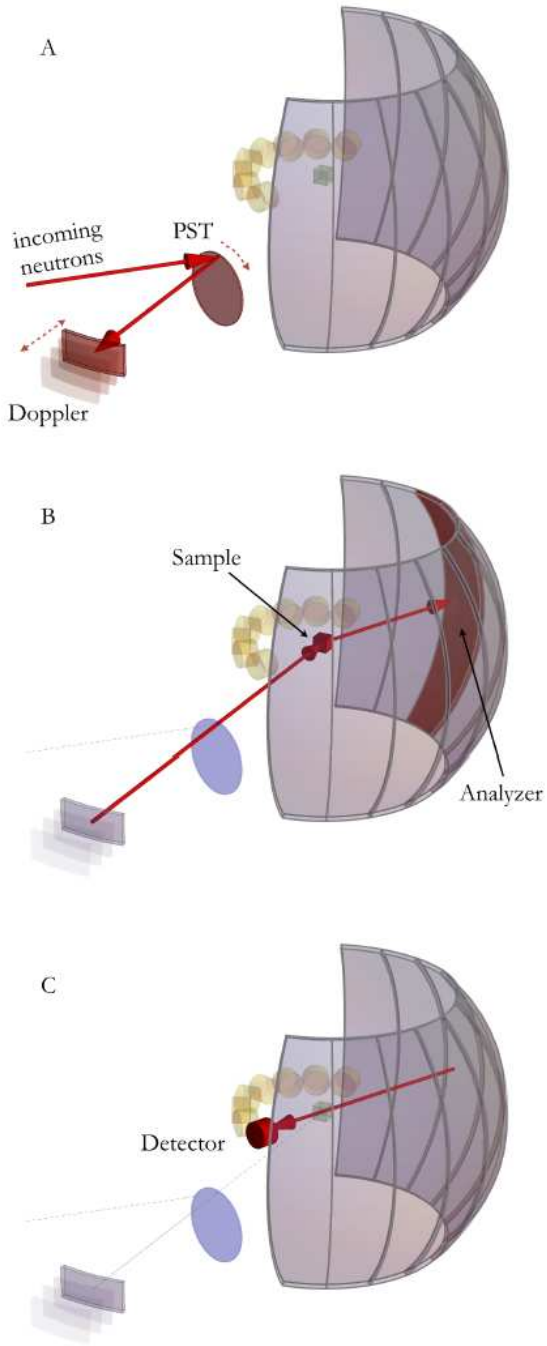

Figure 4.1: Sketch of the basic principle of a cold neutron backscattering spectrometer at a reactor source. (A) The incident beam from the neutron source impinges on the chopper disk denoted "PST". This chopper disk takes the role of a deflector chopper in the old IN16 spectrometer and the role of the Phase Space Transformer (PST) in the new IN16B (for detailed explanations see text). From the PST, the beam is reflected towards the Doppler monochromator. (B) A highly monochromatic beam is backscattered from the Doppler monochromator. The beam passes through an open segment in the PST disk and illuminates the sample. Scattered neutrons from the sample are backscattered at the analyzer crystals if they possess the suitable wavelength and hit the detector (C). Note that the incident beam is pulsed by way of a "background chopper" (not shown) to allow for a discrimination of analyzed and diffracted neutrons in the detectors. (Figure from [71])

4.2 Implementation

A combination of exact backscattering and focusing optics has first been achieved on the IN16 spectrometer at the ILL [55, 53] (figures 4.1 and 4.2). IN16 is thus a second-generation backscattering instrument. It uses a Doppler rather than a heatable monochromator, and the geometrical separation of the impinging and returning beams from the Doppler monochromator is replaced by a separation in time using a rotating deflector chopper disk (figure 4.1). It is only in this configuration that focusing optics can reasonably be achieved since the larger beams cannot be separated geometrically anymore without significant loss in resolution.

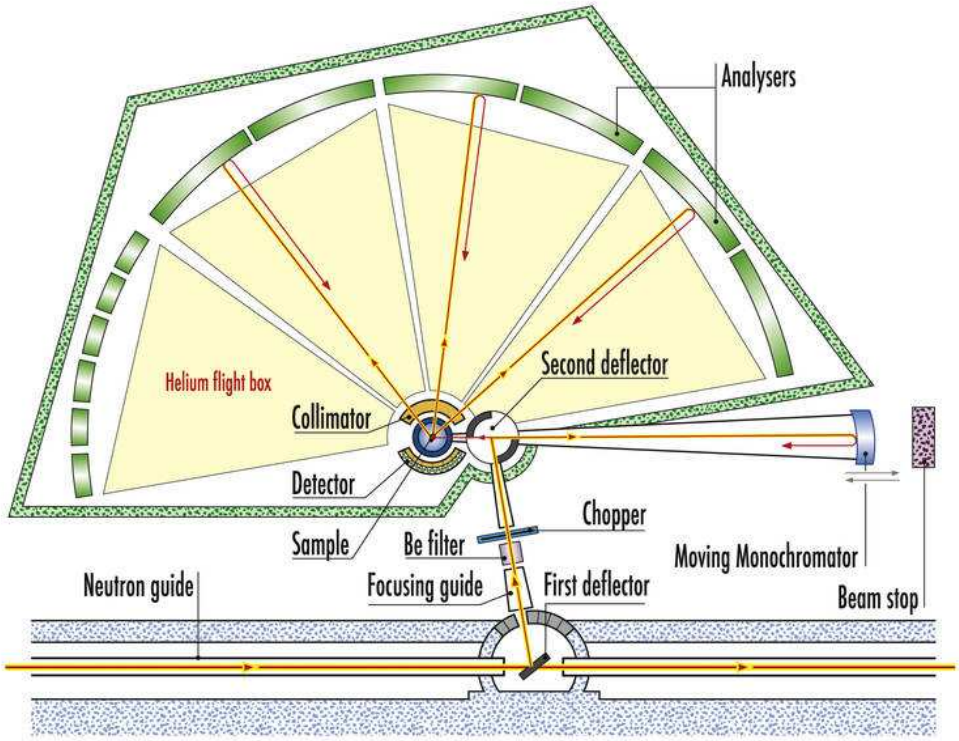

Figure 4.2: Schematic top view of the IN16 backscattering spectrometer at the ILL. IN16 is located at a side position next to a neutron guide such that only a relatively narrow wavelength band $\Delta\lambda/\lambda$ is deflected towards the focus guide by a graphite mosaic crystal ("first deflector"). The remaining neutrons in the main guide travel through the graphite crystal downwards towards other instruments. The neutrons for IN16 pass through a beryllium-filter to remove higher-order reflections from the graphite. The subsequent background chopper generates a pulsed beam with a 50 % duty-cycle and a pulse frequency matched to the total travel time of the neutrons through the secondary spectrometer. The background chopper prevents non-monochromatic neutrons from entering the secondary spectrometer. The deflector chopper carries graphite mosaic crystals on its circumference ("second deflector") and its frequency and phase are such that the neutron pulses from the background chopper are reflected towards the Doppler monochromator, whilst the neutrons from returning from the monochromator can pass through an open deflector chopper segment and illuminate the sample. (Figure from [18])

Most existing backscattering spectrometers use Si(111) analyzer single crystals which set the elastic energy to $E_0 = 2.08\,\mathrm{meV}$ and the maximum scattering vector given by the highest

geometrically accessible scattering angle to $q \approx 2\,\text{Å}^{-1}$. The energy resolution on a cold neutron backscattering spectrometer is in general primarily limited by finite beam size and divergence effects [53]. As a compromise between a high neutron flux and a reasonably good Gaussian energy resolution function, the Si(111) crystals are usually slightly deformed [127] such that the crystal surface lies on a sphere with a radius of 1.5 m (IN10) or 2 m (IN16). The typically achieved energy resolution using such deformed Si(111) crystals at both the monochromator and analyzers is 0.9 μeV FWHM, which is an order of magnitude higher than the theoretical limit given by the primary extinction for Si(111) [67].

State-of-the-art Doppler drives cover an energy transfer range of $-35\,\mu\text{eV} \leq \Delta E \leq +35\,\mu\text{eV}$ at $E_0 = 2.08\,\text{meV}$ by moving the position $s(t)$ of the monochromator along the crystal normal direction on a sinus velocity profile with a maximum amplitude of $s_{\max} = 75\,\text{mm}$ and maximum speed of $\dot{s}_{\max} = 4.7\,\text{m/s}$. The maximum ΔE or maximum speed is mechanically limited by the maximum jerk $\frac{\partial^3 s}{\partial t^3} \approx 300\text{m/s}^3$ to which the payload consisting of the focusing monochromator (surface area typically $25 \cdot 50\,\text{cm}^2$) including its carbon fiber support (approximately 1 kg) can be exposed.

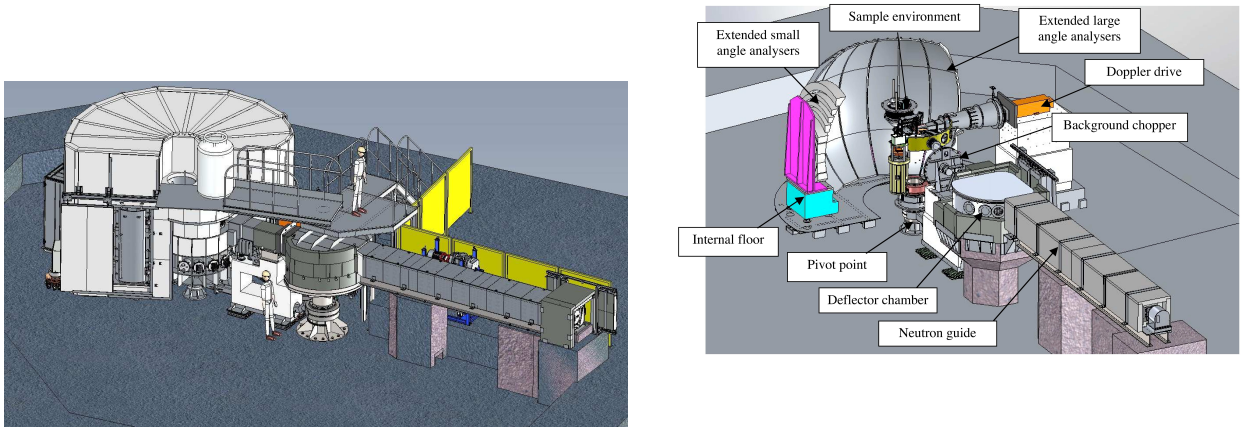

Figure 4.3: General view of the IN16B spectrometer at the ILL (left) and principal optical components (right). One of the main new characteristics compared to the predecessor instrument IN16 (figure 4.2) is the end position of a neutron guide. This end position is necessary to deliver a large wavelength band $\Delta\lambda/\lambda \approx 12\%$ to the phase space transformer chopper disk (see also figure 4.1). The principal structural element is the large vacuum chamber housing the secondary spectrometer, visible far left on the left image. The neutrons are delivered through a neutron velocity selector (far right on the left image) and then through a converging elliptically shaped focus guide (only the shielding is visible on the images). The large vacuum chamber contains the principal optical components (right image), notably the PST, sample, analyzers, and detectors. By contrast, the background chopper and Doppler monochromator are located outside the big vacuum chamber. (Figure from [76])

The emerging so-called spallation neutron sources will complement reactor neutron sources. The spallation sources use high-energy proton beams to decompose heavy nuclei and thus generate neutrons whilst circumventing the self-sustaining fission process. These spallation sources are usually pulsed, i.e. discontinuous in time, with the notable exception of the Swiss spallation source SINQ. At the pulsed neutron sources the dispersion of a source pulse in time can be used to replace the Doppler or heatable monochromator crystal in so-called time-of-flight backscattering spectrometers. This design is useful to extend the dynamic range of the spectrometer at the expense of the energy resolution (see also section 6.5).

The backscattering technique is evolving considerably with the implementation of new backscattering spectrometers at spallation and reactor neutron sources [56]. The first backscattering spectrometer using Silicon crystal analyzers at a pulsed spallation source is BASIS at the SNS in Oak Ridge [101]. At reactor neutron sources, third generation backscattering spectrometers are being implemented [83, 84, 82, 105, 52, 18] which include the phase-space transformation (PST) technique. The following chapter will report on the PST in some detail. The ILL has committed itself to commission the new backscattering spectrometer IN16B (figure 4.3) which will contain a PST. The principal structural element of this new spectrometer is the large vacuum chamber made from Aluminum which will contain the single crystal analyzer spheres on a sample-to-analyzer radius of 2 m. The considerable height of the chamber is chosen to accommodate large analyzer elements to maximize the usable solid angle. The PST, sample, and analyzers are all located inside the chamber. The Doppler drive, by contrast, will be located outside the vacuum chamber since the linear motor moving the monochromator on the Doppler machine cannot operate in vacuum. IN16B is designed to accommodate different sets of monochromator and analyzer crystals, namely Si(111), Si(311), and GaAs(200). For this reason and also to change over to the so-called BATS-mode (section 6.5), the vacuum chamber can be rotated around the vertical axis through the PST (figure 4.3, right) to move to the appropriate take-off angle from the PST and to allow to move out of the reflecting mode from the PST entirely for the BATS-mode. The deflector chamber (figure 4.3, right) permits to operate IN16B on an optional side position. This side position will move the PST disk out of the direct sight of the delivering neutron guide and thus allow for data acquisitions at a reduced background. By contrast, in this position, the spectrometer will not benefit from the flux increase by the PST (chapter 5).

In terms of real-space dimensions, backscattering spectrometers access nanosecond time scales and nanometer length scales and are thus ideally suited to study self-diffusion in glass systems, polymers, lipids, humidified proteins, nanoscale porous systems and nanoscale colloidal suspensions such as protein solutions. Since backscattering spectrometers in the absence of polarization filters record both coherent and incoherent scattering, they can also be used to study collective diffusion as opposed to self-diffusion in suitable sample systems with sufficiently strong coherent scattering. Furthermore, due to the extremely high energy resolution and in the case of reactor-based backscattering spectrometers the nearly Gaussian line shape of the energy resolution function, backscattering can be used for quantum rotational tunneling spectroscopy. This technique has been used widely to quantify chemical potentials [123]. At present, tunneling spectroscopy is still used to map surface potentials in molecular adsorption, for instance in the science of catalysis. The relatively low neutron flux at the sample position (on the order of 10^5 neutrons/cm^2/s at IN16) due to the high energy definition poses limitations to the application of the backscattering technique.

4.3 Data acquisition modes

When diffusive motions are investigated using a neutron backscattering spectrometer, these motions manifest themselves through a broadening of the resolution function. This broadening is denoted quasi-elastic scattering (QENS). Such a line broadening can equivalently be understood in terms of an overdamped motion or relaxation process. The underlying models describing this broadening may become very complex [12]. An example QENS spectrum recorded on IN16 is depicted in figure 4.4. Here, a model globular protein in aqueous solution was studied [135] (see also section 8.5). This example spectrum can be modeled by a superposition of protein internal diffusive and vibrational modes and the protein translational

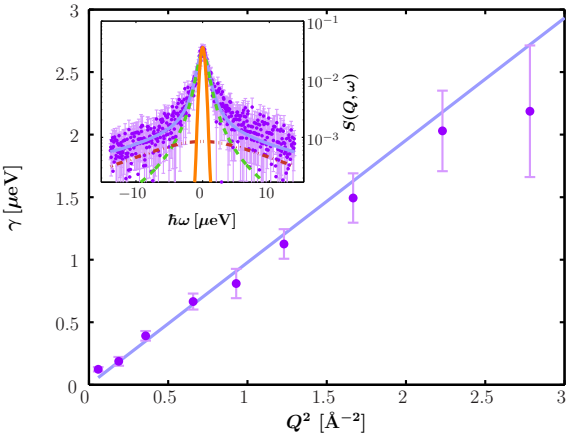

Figure 4.4: Inset: Example backscattering spectrum $S(Q,\omega)$ (symbols) recorded at IN16 for BSA proteins in an aqueous (D_2O) solution (concentration 500 mg/ml, T = 300 K, individual detector at $Q = 0.81\text{Å}^{-1}$). The magenta solid line denotes a fit of a model according to equation 4.2. These two Lorentzians are indicated by the dashed and dash-dotted lines, respectively. The orange solid line denotes the resolution function. Main figure: Fitted linewidth of the narrow Lorentzian γ (symbols) versus Q^2 for the full Q-range of the example data. The fit of $\gamma = D\,Q^2$ (blue line) is consistent with simple diffusive behavior. For statistical reasons the fit range is restricted to $Q^2 < 1.5\,\text{Å}^{-2}$. (Figure from [135])

and rotational diffusion. The fit describing the data consists of two Lorenztian functions $L_\gamma(\omega)$ and $L_\Gamma(\omega)$, a Dirac function $\delta(\omega)$, the instrumental resolution function $\mathcal{R}(\omega)$, and a flat background B [155, 135]:

$$S(Q,\omega) = \mathcal{R}(\omega) \otimes \mathcal{L}_\gamma(\omega) \otimes [\beta_1\,\delta(\omega) + \beta_2\,\mathcal{L}_\Gamma(\omega)] + B. \tag{4.2}$$

Therein, $\delta(\omega)$ accounts for the elastic scattering from the proteins, B for the signal from the water molecules which move by an order of magnitude faster than detectable by IN16, and the width Γ of the broader Lorentzian function accounts for internal diffusion modes of the proteins. The width γ of the narrow Lorentzian contains both the translational and rotational diffusion contributions of the entire protein in the solution. Using this relatively simple model, the apparent self-diffusion coefficient D can be obtained assuming simple Brownian diffusion, i.e. $\gamma = D\,Q^2$ (figure 4.4, see also chapter 2). $D = D(D_t, D_r)$ contains both the translational and rotational components of the diffusion. These contributions can be separated using further models and mathematical methods [135].

Besides the QENS spectra, which are recorded to model diffusion processes, we briefly mention a second acquisition mode using backscattering. In this mode, the incident energy is not scanned using the Doppler shift, but kept constant. This constant incident energy for this type of scan usually is the same energy as the analyzed energy. Therefore, in this mode, only the elastically scattered neutrons within the very narrow energy resolution window $\Delta\omega$ of the spectrometer are detected, namely $S\,(Q, |\omega| < \Delta\omega) = \mathcal{R}(\omega) \otimes S(Q,\omega)|_{\omega=0}$. This mode mostly serves to study the temperature-dependence of the thermal Debye-Waller factor of a sample, but also for other more complex problems. For instance, in humid proteins this scan can be used to quantify the plasticizing effect of water (see also sections 8.3 and 8.5.3).

Finally, when inelastic scattering is caused by a sample, e.g. through rotational tunneling (see e.g. Ref. [123]), inelastic peaks evidently appear in the backscattering spectra. However, this type of experiment shall not be further discussed in the present review.

Chapter 5

New developments in neutron optics – the Phase Space Transformer (PST)

The low speed of cold neutrons allows to mechanically implement a Bragg reflection in a moving reference frame with significant impact on the neutron phase space coordinates $(\mathbf{r}, \mathbf{k})$. This chapter is based on the reference [72].

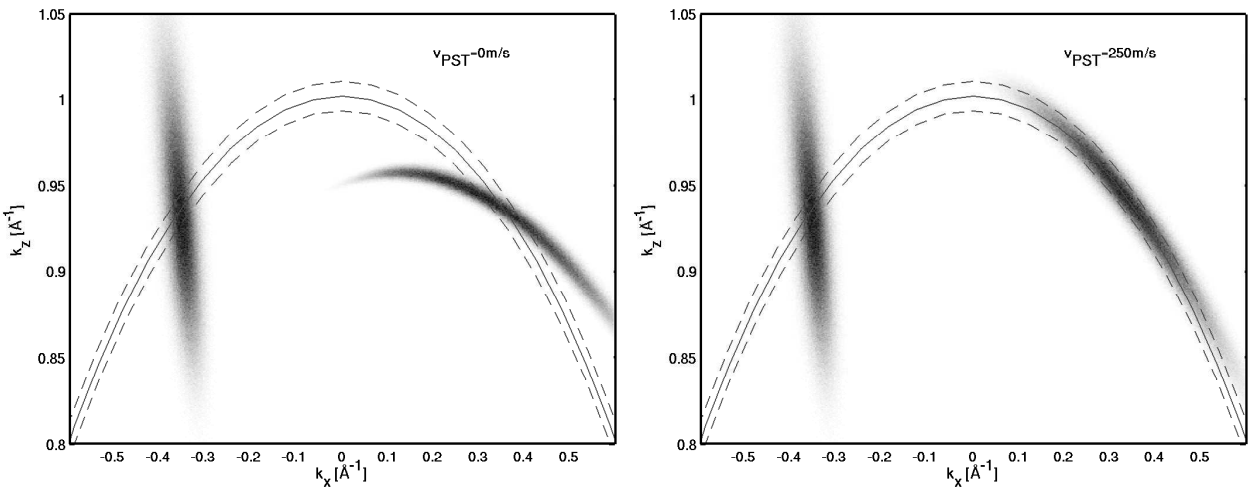

Figure 5.1: Simulated incident and reflected neutron density distributions in $\mathbf{k}$-space. Plotted is the 2-dimensional projection of a phase space element prior (left clouds) and subsequent (right clouds) to the reflection from a mosaic crystal at rest (left figure) and at $v = 250\,\mathrm{m/s}$ (right figure), respectively. The point density is proportional to the neutron density. The solid line denotes the elastic line at the monochromator, and the dashed lines mark the limits of the acceptance range of the moving monochromator. For the simulation, a gaussian mosaic with 6.6° FWHM in the horizontal direction of motion of the PST crystal and 2.2° FWHM in the vertical direction has been assumed. The Gaussian incident beam divergence in the model was 3° FWHM horizontally and 6° FWHM vertically. The Gaussian incident wavelength spread was $\Delta\lambda/\lambda = 12.5\%$. (Figure from [72])

5.1 The PST - definition

Backscattering spectrometers profit from significant progress in neutron optics. The most prominent amongst the advances made in recent years is the Phase Space Transformation

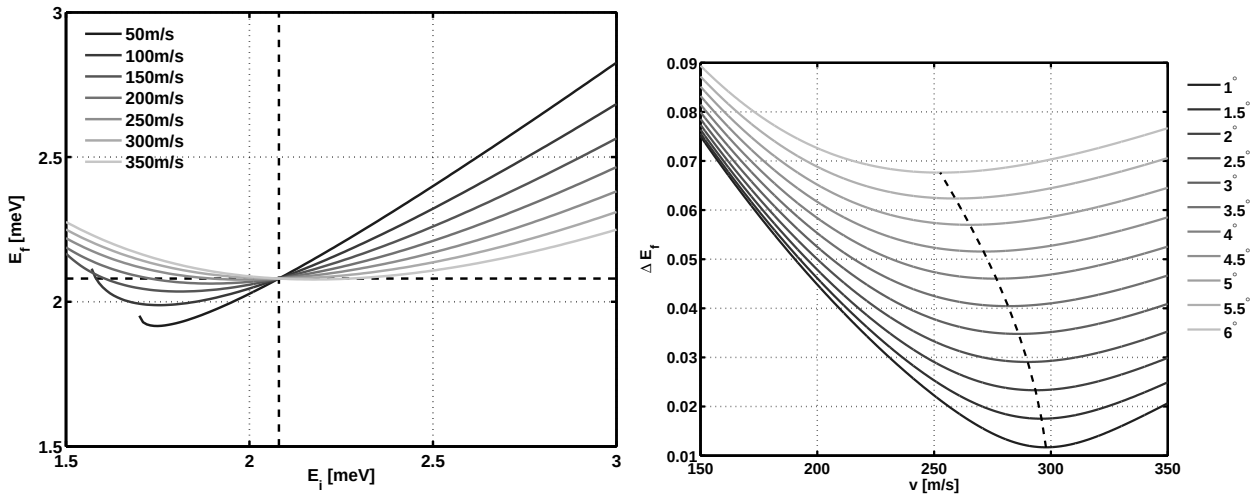

Figure 5.2: Left: Final energy E_f after a G(002)-Bragg reflection from a moving graphite crystal as a function of the incident energy E_i of the impinging neutron according to equation 5.8 for different crystal speeds $\mathbf{v}_{\mathrm{PST}} = v_{\mathrm{PST}}\mathbf{e}_x$ as specified in the legend. The dashed lines indicate the energy $E_0 = 2.08\,\mathrm{meV}$ corresponding to the Si(111) wavelength $\lambda = 6.27\,\text{Å}$. The angular divergences in the $(\mathbf{k}_x, \mathbf{k}_z)$ and $(\mathbf{k}_y, \mathbf{k}_z)$ planes, respectively, were fixed to $\Delta\Theta_{xz} = 3°$ and $\Delta\Theta_{yz} = 6°$ Gaussian FWHM, respectively. (Figure from [72]) Right: Estimated error ΔE_f in the final energy E_f as a function of the crystal speed v for different divergences ("errors") $\Delta\Theta_{xz}$ (given as Gaussian FWHM in the legend) of the impinging neutron beam according to equation 5.17. The "error" in the incident wavelength is assumed to be $\Delta\lambda = 0.125\,\lambda$, and $\Delta\Theta_{yz} = 6°$ FWHM. The dashed line indicates the optimum speed for the PST resulting from the analytical estimate. (Figure from [72])

(PST). This technique has already been proposed some time ago [139] and successfully been implemented at the backscattering spectrometer at NIST [105]. It has also successfully been applied to ultra-cold neutrons [103]. The PST is a coordinate transformation on the impinging neutron beam which is achieved by a Bragg reflection from a moving mosaic crystal: Be $\mathbf{k}_i$ the incident wavevector and $\mathbf{k}_f$ the scattered wavevector in the laboratory frame of a neutron scattering event from a crystal. Then we can write the Bragg reflection in the laboratory frame

$$\mathbf{k}_f = \mathbf{k}_i + \mathbf{Q}, \tag{5.1}$$

where $\mathbf{Q}$ is the reciprocal lattice vector of the scattering event. Be $\mathbf{v}$ the non-relativistic speed of the crystal relative to the laboratory frame, m the mass of the neutron, and

$$\mathbf{K} = \frac{m}{\hbar}\mathbf{v}. \tag{5.2}$$

Then

$$\mathbf{k}'_i = \mathbf{k}_i - \mathbf{K} \tag{5.3}$$

is the incident wavevector in the moving frame of the crystal, and the scattering event in the moving frame can be written as

$$\mathbf{k}'_f = \mathbf{k}'_i + \mathbf{Q}(\mathbf{k}'_i). \tag{5.4}$$

By transforming back to the laboratory frame using

$$\mathbf{k}_f = \mathbf{k}'_f + \mathbf{K} \tag{5.5}$$

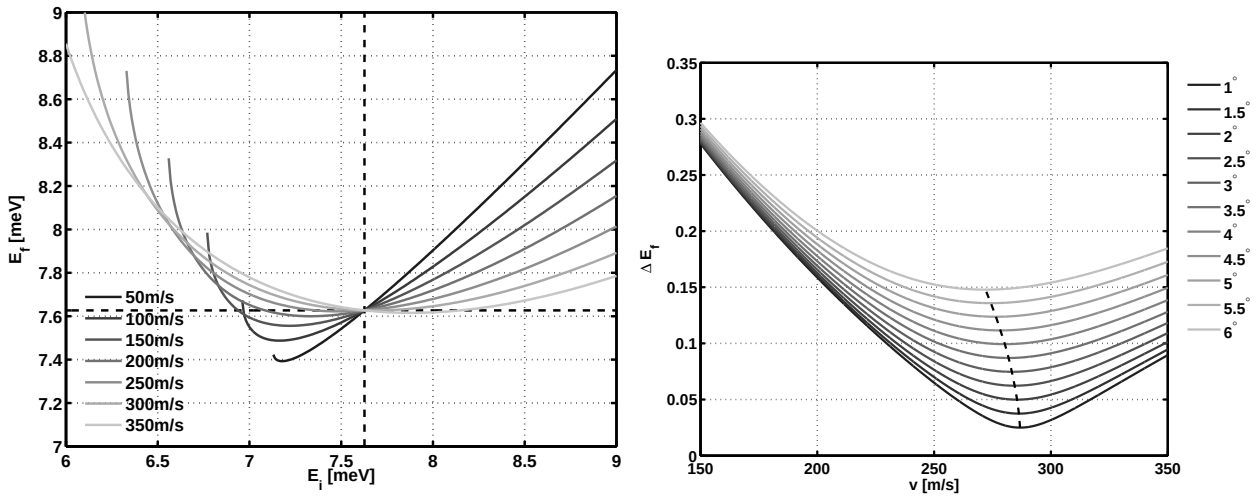

Figure 5.3: Left: Final energy E_f after a G(004)-Bragg reflection from a moving graphite crystal as a function of the incident energy E_i of the impinging neutron according to equation 5.8 for different crystal speeds $\mathbf{v}_{\mathrm{PST}} = v_{\mathrm{PST}}\mathbf{e}_x$ as specified in the legend. The dashed lines indicate the energy $E_0 = 7.68\,\mathrm{meV}$ corresponding to the Si(311) wavelength $\lambda = 3.28\,\text{Å}$. The angular divergences in the $(\mathbf{k}_x, \mathbf{k}_z)$ and $(\mathbf{k}_y, \mathbf{k}_z)$ planes, respectively, were fixed to $\Delta\Theta_{xz} = 1.5°$ and $\Delta\Theta_{yz} = 3°$ Gaussian FWHM, respectively. Right: Estimated error ΔE_f in the final energy E_f as a function of the crystal speed v for different divergences ("errors") $\Delta\Theta_{xz}$ (given as Gaussian FWHM in the legend) of the impinging neutron beam according to equation 5.17. The "error" in the incident wavelength is assumed to be $\Delta\lambda = 0.125\,\lambda$, and $\Delta\Theta_{yz} = 3°$ FWHM. The dashed line indicates the optimum speed for the PST resulting from the analytical estimate.

and inserting equations 5.3, 5.4 we obtain

$$\mathbf{k}_f = \mathbf{k}_i + \mathbf{Q}(\mathbf{k}_i - \mathbf{K}). \tag{5.6}$$

The beneficial consequences for the neutron flux at the sample position of a backscattering spectrometer result from the effect of the PST on the energy distribution. This effect can be visualized by calculating the final energy E_f behind the PST [72]. For this purpose, we write the final energy of a neutron after a Bragg reflection from a moving mosaic crystal according to equation 5.6:

$$E_f = \frac{\hbar^2}{2m}\,|\mathbf{k}_f|^2 = \frac{\hbar^2}{2m}\,|\mathbf{k}_i + \mathbf{Q}(\mathbf{k}_i - \mathbf{K})|^2. \tag{5.7}$$

Let us simplify the notation by assigning $\mathbf{k} = \mathbf{k}_i$, hence

$$E_f = \frac{\hbar^2}{2m}\|\mathbf{k} + \mathbf{Q}\|^2. \tag{5.8}$$

The effect of the PST on the final energy E_f of the neutrons and energy spread ΔE_f can be calculated on the "back of an envelope" [72], and the results are depicted in the figures 5.2 and 5.3 for Si(111) and Si(311) monochromators, respectively (see also section 5.3). It is thereby important to note that in a backscattering spectrometer, the PST is applied to a divergent incident beam (right parts of figures 5.2 and 5.3). This divergent incident beam is further characterized by a spread $\Delta\lambda$ of the wavelength λ or, synonymously, length of $\mathbf{k}_i$ (cf. figure 5.1).

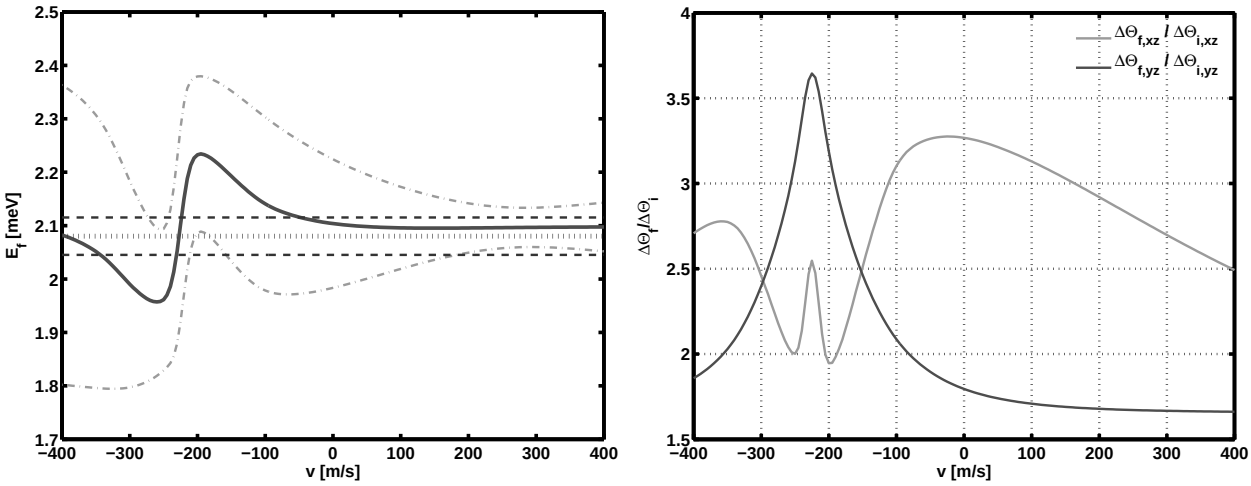

Figure 5.4: Left: Expectation value $\langle E_f \rangle$ (solid line) and spread in E_f (dash-dotted lines) computed from the variation by $\langle E_f \rangle \pm \langle (E_f - \langle E_f \rangle)^2 \rangle$ as a function of the crystal speed v obtained from Monte Carlo simulations. The dotted line denotes the elastic energy, and the dashed lines mark the energy acceptance range of the Si(111) Doppler monochromator, respectively. (Figure from [72]) Right: Ratio of the impinging $\Delta\Theta_i$ and reflected $\Delta\Theta_f$ angular beam divergences at the PST device as a function of the PST crystal speed $\mathbf{v}_{\mathrm{PST}} = v_{\mathrm{PST}}\mathbf{e}_x$ assuming a mosaic spread of 2.2° Gaussian FWHM in the (x, y)- and 6.6° in the (x, z)-plane, respectively, obtained from the numerical simulations for the Si(111) setup. The incident beam divergence was $\Delta\Theta_{i,xy} = 3°$ in the horizontal and $\Delta\Theta_{i,xz} = 6°$ FWHM in the vertical direction, respectively. (Figure from [72])

5.2 Numerical implementation

The implementation of Monte Carlo simulations of the PST in *MATLAB* is straight-forward based on equation 5.6 [70]. For the mosaic crystal reflectivity we employ the Sears equations [141, 142]. We assume Gaussian distributions for the incident wavelength spread and angular beam divergence as well as for the mosaic distribution. Plots from example simulations (figure 5.1) illustrate the rotation of a phase space element upon Bragg reflection from the moving mosaic crystal relative to the same phase space element reflected from a crystal at rest. The optimum relative flux gain is achieved when the reflected phase space element best matches the phase space acceptance range of the neutron backscattering spectrometer (dashed lines in figure 5.1) given by the Doppler monochromator (cf. section 4.2).

The numerical simulations also illustrate the dependence of the energy expectation value $\langle E_f \rangle$ and standard deviation $\langle (E_f - \langle E_f \rangle)^2 \rangle$ subsequent to the PST as a function of the crystal speed (figure 5.4). The optimum crystal speed is achieved when $\langle E_f \rangle \pm \langle (E_f - \langle E_f \rangle)^2 \rangle$ best matches the energy acceptance range of the spectrometer. It also becomes evident that the direction of the velocity vector is essential. Further, the numerical simulations provide information on the change in the beam divergence by the PST (figure 5.4, right). Remarkably, the reflected beam divergence decreases with increasing speed.

Finally, we compare the relative flux gain at the sample position as obtained from the numerical simulations with the gain resulting from analytical estimations discussed in the following section (figure 5.5). The analytical estimate of the gain (figure 5.5, left) implies an analytical inversion of the PST [72]. This inversion is only easily achievable based on a first-order Taylor expansion of the PST function. In addition, the analytical approximation is based on the assumption that Gaussian distributions transform into Gaussian distributions

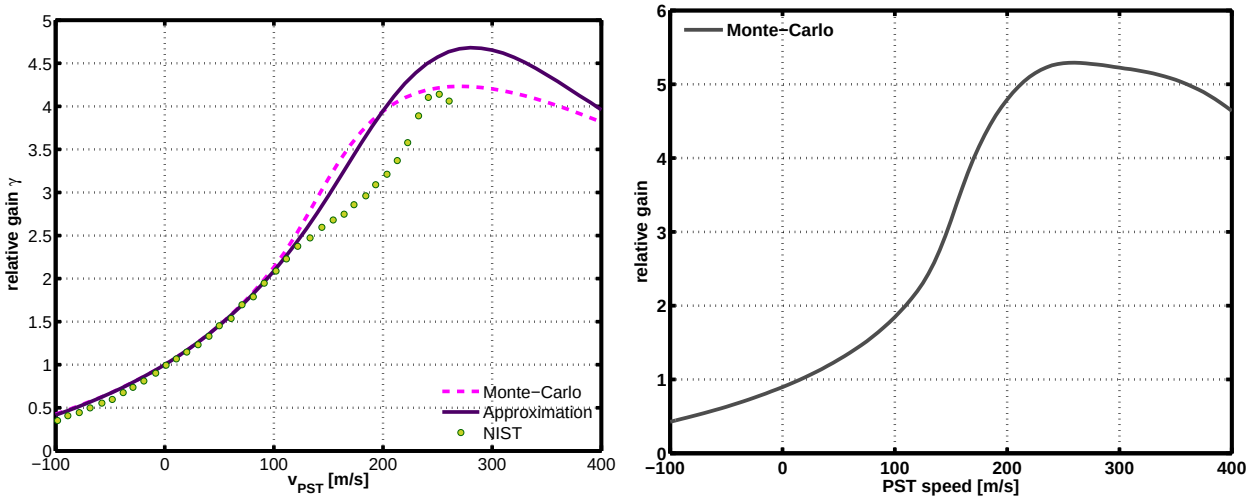

Figure 5.5: Left: Comparison of the analytical estimate and Monte Carlo simulations of the flux gain at the sample position as a function of the PST speed v relative to the flux at $v = 0$ (solid lines), assuming an energy acceptance range of the moving monochromator of $|E - E_0| \leq 35\mu$eV. For these Monte Carlo simulations, we have assumed the same mosaic crystal and impinging neutron beam properties as for the simulations depicted in figure 5.2. For the analytical estimation, we have used the horizontal beam divergence from the numerical simulations for $\Delta\Theta$ in eq. 5.17, i.e. 3° FWHM. The symbols are experimental data of the NIST backscattering spectrometer taken from [105]. The incident horizontal beam divergence at this spectrometer is approximately 3° FWHM [105]. (Figure from [72]) Right: Simulated gain curve for the Si(311) configuration of IN16B, using the same parameters as given in the caption of figure 5.3.

following the PST. The analytical estimate is therefore only an approximation, and the deviation of the estimate from the Monte Carlo simulation result (figure 5.5, left) can be attributed to the limited Taylor expansion. The analytical estimate also takes into acount the Sears equations.

5.3 Analytical estimate

Here, we introduce some simple considerations to analytically estimate the PST gain based on concepts of error propagation. A more sophisticated approach is described in Ref. [72]. Technically, the PST is carried out in the scattering plane of the spectrometer only, i.e. in the horizontal plane $(\mathbf{e}_x, \mathbf{e}_y)$. Hence, the problem can to a good approximation be reduced to two dimensions. For simplicity and to elucidate the basic principle, we therefore restrict the discussion to two dimensions in the following. The generalization to three dimensions can be found in Ref. [72], and all simulations depicted in the figures of this chapter are based on the three-dimensional generalization. In the two-dimensional case, for a moving system with crystal speed $\mathbf{v}_{\mathrm{PST}}$ and $\mathbf{K} = m\mathbf{v}_{\mathrm{PST}}/\hbar$, the momentum transfer is

$$\mathbf{Q} = \frac{Q}{\Gamma} \begin{pmatrix} \cos\phi & -\sin\phi \\ \sin\phi & \cos\phi \end{pmatrix} \mathbf{\Gamma}. \tag{5.9}$$

Therein, $\mathrm{Q} = 2\pi/d$ with d being the lattice spacing of the moving crystal, and ϕ is defined by

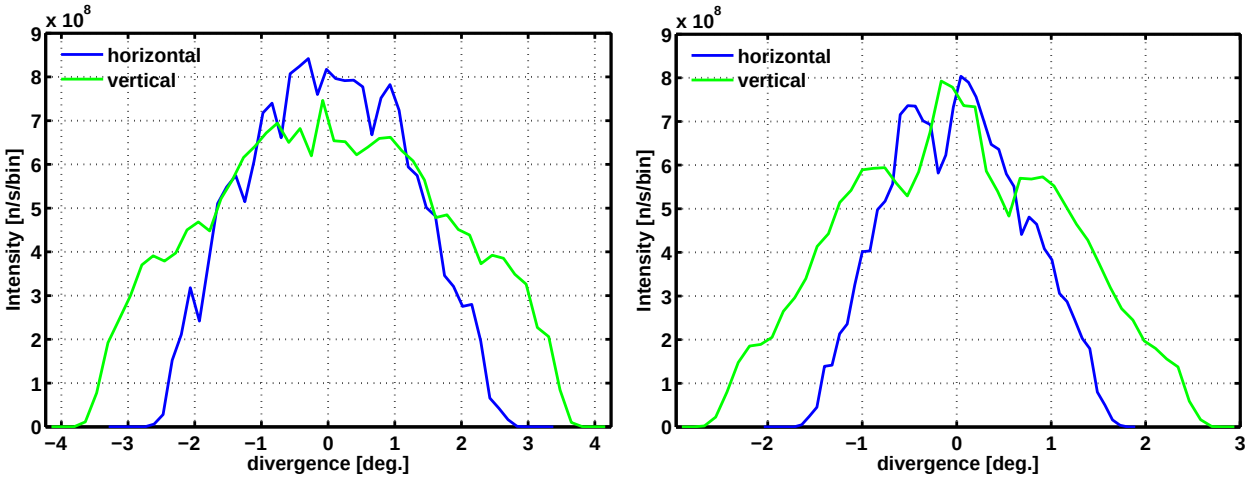

Figure 5.6: Divergence of the beam impinging on the PST for the Si(111) (left) and Si(311) (right) configurations, respectively, obtained from McStas simulations for IN16B. The full angle range is divided in 50 discrete channels (bins).

$$\cos\phi = -\frac{Q}{2\Gamma}, \tag{5.10}$$

and $\mathbf{\Gamma} = \mathbf{k} - \mathbf{K}$ (eq.5.3). The norm of the momentum vector in equation 5.8 can be written as

$$\|\mathbf{k} + \mathbf{Q}\|^2 = k^2 + Q^2 + 2\langle \mathbf{k}, \mathbf{Q}\rangle . \tag{5.11}$$

We simplify the dot product in the above expression using the fact that $\mathbf{v}_{\mathrm{PST}} = v_{\mathrm{PST}}\mathbf{e}_x$, hence $\mathbf{K} = K\mathbf{e}_x$. Furthermore we assume that

$$\mathbf{k} = k\left(\cos\theta, -\sin\theta\right), \tag{5.12}$$

where θ is the angle between the impinging neutron beam and the crystal surface. We then obtain

$$\langle \mathbf{k}, \mathbf{Q}\rangle = \frac{Q}{\Gamma}\left\{k^2\cos\phi - kK\left(\cos\theta\cos\phi - \sin\theta\sin\phi\right)\right\}. \tag{5.13}$$

Using this expression for the dot product and the definition for ϕ we finally obtain for the energy of the scattered neutrons

$$E_f = \frac{\hbar^2}{2m}\left\{k^2 + \frac{Q^2}{\Gamma^2}\left[K^2 + kK\left(\sin\theta\sqrt{\frac{4\Gamma^2}{Q^2} - 1} - \cos\theta\right)\right]\right\}. \tag{5.14}$$

The energy of the impinging neutrons is linked to k by

$$E_i = \frac{\hbar^2}{2m}k^2. \tag{5.15}$$

The error of E_f is computed by Gaussian error propagation and linearizing E_f, hence

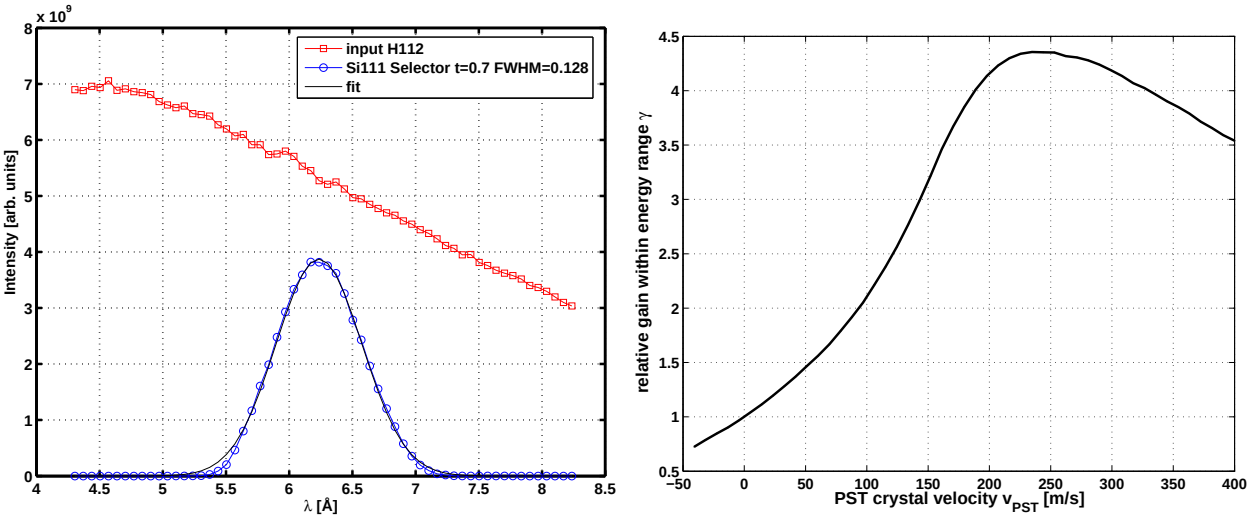

Figure 5.7: Left: Spectral distribution of the incoming and transmitted neutron beam at the Si(111) neutron velocity selector. Right: Simulated gain curve at the Phase Space Transformer for the Si(111) configuration taking into account the actual impinging $\Delta\lambda/\lambda$, beam divergence, crystal mosaic, and energy acceptance range of the Doppler drive.

$$\Delta E_f^2 = \left(\frac{\partial E_f}{\partial E_i}\Delta E_i\right)^2 + \left(\frac{\partial E_f}{\partial \theta}\Delta\theta\right)^2, \tag{5.16}$$

or in three dimensions taking into account the different angles Θ_{xz} and Θ_{yz} between the incident wavevector components $(\mathbf{k}_x, \mathbf{k}_z)$ and $(\mathbf{k}_y, \mathbf{k}_z)$, respectively,

$$\Delta E_f^2 = \left(\frac{\partial E_f}{\partial E_i}\Delta E_i\right)^2 + \left(\frac{\partial E_f}{\partial \Theta_{xz}}\Delta\Theta_{xz}\right)^2 + \left(\frac{\partial E_f}{\partial \Theta_{yz}}\Delta\Theta_{yz}\right)^2. \tag{5.17}$$

The figures 5.2, and 5.3 illustrate the equations 5.14, 5.17 and the resulting optimum crystal speed for the Si(111) and Si(311) monochromators, respectively. Note that the PST needs a certain minimum ΔE_i to function properly, since it is the "compression" of the impinging neutrons in energy which creates the increase of the flux in the useful energy range of the spectrometer. We assume $\Delta E_i = 0.12E_i$, which is close to the optimum resulting from our detailed numerical simulations [70].

We calculate the mean E_f and the standard deviation ΔE_f from equation 5.8 and 5.17, respectively, using the mean values for E_i, Θ_{xz} as well as Θ_{yz}. Assuming that the incident neutrons are normally distributed by ρ_i and that the reflected neutrons are normally distributed by ρ_f, this simplification allows us to estimate the relative gain γ by

$$\gamma = \frac{\Phi_f}{\Phi_i} = \frac{\int_{E_0\pm\Delta E_0} \rho_f(\epsilon)\, d\epsilon}{\int_{E_0\pm\Delta E_0} \rho_i(\epsilon)\, d\epsilon} \tag{5.18}$$

with the flux within the monochromator acceptance range

$$\Phi_\alpha = \frac{\Phi_0}{2}\left\{\mathrm{erf}\left(\frac{\Delta E_0 + E_0 - E_\alpha}{\sqrt{2}\Delta E_\alpha}\right) + \mathrm{erf}\left(\frac{\Delta E_0 + E_0 + E_\alpha}{\sqrt{2}\Delta E_\alpha}\right)\right\} \tag{5.19}$$

where Φ_0 is the total flux and $\alpha = i, f$ denotes the initial and reflected neutrons, respectively. The resulting estimated gain curve as a function of crystal speed is depicted in figure 5.5

(left) for the Si(111) configuration of IN16B together with the gain curve obtained from the Monte Carlo simulation. At high crystal speeds the estimate becomes inaccurate, because the PST function is expanded in a Taylor series to first order only prior to inversion. Figure 5.5 (left) also illustrates the good agreement of both the Monte Carlo simulations and the analytical estimate with experimental data on the existing PST at NIST. Figure 5.6 depicts the beam divergences impinging on the PST in the actual IN16B instrument according to McStas simulations of the entire upstream neutron optics. The transmission of the neutron velocity selector upstream from the focus guide of IN16B is given in figure 5.7(left) (cf. section 6.3), and figure 5.7(right) provides the anticipated PST gain curve for IN16B taking into account all upstream neutron optical parameters. It is stressed, however, that simulations always represent an idealized situation, and that the gain is relative. Therefore, the actually achievable performance may be considerably lower.

The PST will provide a significant increase of the neutron flux at the sample position of the new spectrometer IN16B compared to its predecessor instrument IN16. This flux improvement will be achieved at the expense of an acceptably increased angular beam divergence. Further flux gains at IN16B will arise from an augmented analyzer surface area, the use of a vacuum chamber for the secondary spectrometer, as well as from an optimized neutron guide and focus optics. The latter will be described in the following chapter.

Chapter 6

Further developments and observations in neutron optics for backscattering

The Phase Space Transformer will be mounted inside the vacuum chamber of IN16B as a compact disk with only 43 cm radius [52] (cf. figure 4.1) carrying the graphite mosaic crystals at its circumference, resulting in a centrifugal crystal acceleration on the order of $10^5\,\mathrm{m/s^2}$ at the optimum PST speed as derived in the previous chapter, and thus being at the limit of mechanical feasibility. The small disk radius is chosen to minimize the shade created on the high-angle analyzer crystals. Around the PST as key optical component, several other optical elements have to be optimized for an ideal performance of the new backscattering spectrometer IN16B. The focusing optics imposes that the PST and the sample are located close to each other, because both require a small beam size. Conversely, the beam is large at the monochromator. This chapter is based on the references [18, 56, 167].

6.1 Instrument siting

The proper placement of a backscattering spectrometer induces various requirements which put a challenge to neutron optics. The first requirement is to obtain a high flux at the most frequently used wavelengths, namely 6.271 Å, corresponding to Si(111) analyzers, and 3.28 Å, corresponding to Si(311) analyzers.

The spectral distribution of the neutron intensity inside a neutron guide is difficult to obtain. Only the integral intensity is directly accessible by so-called neutron capture measurements using the activation of gold foils placed in the neutron guide. Information on the spectral distribution can be obtained at instruments along the guide which can measure the dispersion in energy through monochromators or time-of-flight choppers. However, the spectral information gained at such an instrument is difficult to correct for the spectral influence of the instrument itself and spectral sensitivity.

Our simulations [18] were carried to points in the ILL's guide system where capture flux data were available (figure 6.2, left), and comparisons at these points were difficult due to the different coatings of the neutron guide up to these points. Nevertheless, taking these factors into account, from our simulations and in agreement with detailed simulations by K.Andersen [6] based on energy-dispersive data from different instruments, we conclude that the two cold sources existing at the ILL are equivalent at least for wavelengths $\lambda < 10\,\text{Å}$.

The second important criterion for the placement of a third generation backscattering

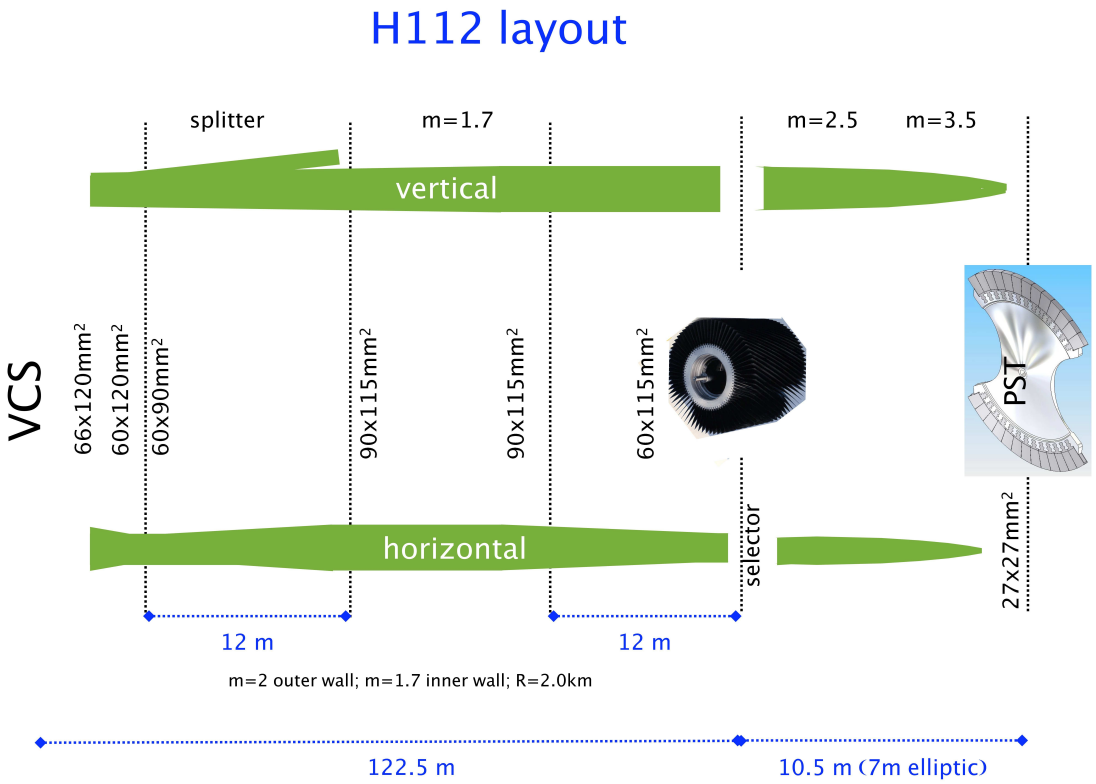

Figure 6.1: Sketch of the layout of the H112 neutron guide serving the instrument IN16B, displaying both a vertical (top) and horizontal (bottom) view. m denotes the critical scattering vector of total external reflection of the guide coating relative to the critical scattering vector of a Nickel coating. The neutrons emerge from the vertical cold source (VCS), which is one of the two cold neutron moderators within the reactor vessel of the ILL. (Figure from [56])

spectrometer comprising a phase space transformer is the required incident energy or wavelength spread which must be delivered to the PST. From our simulations it resulted that the optimum performance of the PST is reached at a spread of $\Delta\lambda/\lambda = 12.5\%$ in the case of the Si(111) configuration (see chapter 5). This $\Delta\lambda/\lambda$ results from the energy acceptance range of the moving monochromator and the flux gain optimum of the PST. This large wavelength spread requires to place the instrument at a guide end position. The space occupied by the secondary spectrometer in addition requires that the instrument is located at a large distance from the neutron source.

The above considerations in summary and the few available possible guide end positions have resulted in an extremely long neutron guide, denoted H112, for IN16B (figure 6.1). The principal neutron optical elements along the H112 guide are depicted in this sketch, namely the Vertical Cold Source (VCS), which is one of the two cold neutron moderator sources at the ILL, a beam splitter which diverts the top 30 mm of the initial vertical guide height of 120 mm upwards to a beam position for a future second instrument on the same guide. These are followed by optical components that only serve IN16B and that will be discussed in the following sections.

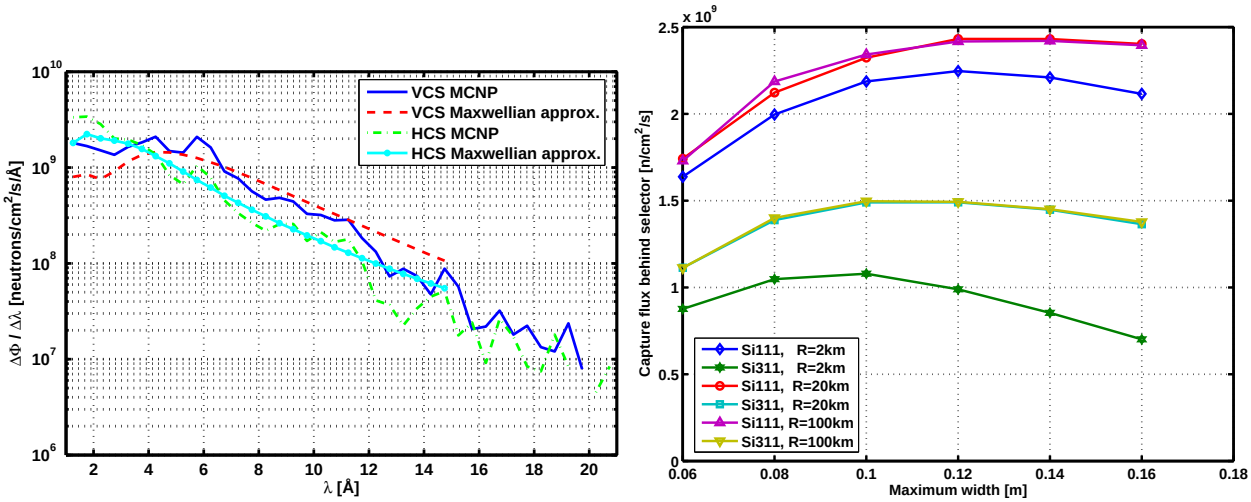

Figure 6.2: Left: Simulated spectral distribution at the respective "safety valve" positions of the guides denoted H112 emerging from the "vertical cold source" and H53 emerging from the "horizontal cold source", respectively. The distance of the safety valve from the source is approximately 2.5 m in vacuum plus 9 m of guide in a direct line of sight. Please note that H53 is coated with $m = 1.2$ supermirror coating whilst H112 is coated with $m = 2$, to a large part explaining the difference in the spectra. Please note also that the flux $d\Phi/d\lambda$ has been discretely sampled into $\Delta\Phi/\Delta\lambda$ with a sampling into 0.5 Å-wide channels without capture-weighting. Right: Simulated capture flux downstream from the neutron velocity selector as a function of the maximum ballistic width for different centre wavelengths corresponding to the Si(111) and Si(311) configuration of IN16B, respectively, and different radii of curvature for the future guide H112. The length of the linearly diverging and converging sections both is 16 m in each case in this model. The radius of 100 km is chosen to approximate a straight guide. (Figure from [18])

6.2 Ballistic neutron guide, velocity selector, and focus guide

To reduce the total number of reflections of the transported neutrons, the neutron guide H112 serving IN16 be will be approximately ballistic [1]. The idea is to adiabatically transform the phase space of the neutrons by gently expanding the neutron guide cross section area over a long distance (12m, see figure 6.1) starting from the neutron source and thereby reducing the angular divergence of the neutrons. The subsequent main part of H112 has a constant cross section area, followed by a gently converging part which "mirrors" the expanding initial part and adiabatically back-transforms the neutron phase space to the original shape. This converging section equally has a length of 12 m. The chosen width of the H112 guide (9 cm) is a compromise of the optimum performance (figure 6.2, right) and the required curvature radius R of the guide. Since the instrument shall also operate using Si(311) crystals, i.e. at a wavelength of 3.28 Å, the H112 neutron guide requires a critical or cutoff wavelength λ^* [100] which is sufficiently far below this wavelength. The radius $R = 2000$ m is given by geometrical requirements in the neutron guide hall. Therefore, a maximum ballistic width of 9 cm was pre-defined in order to obtain a sufficiently small λ^*.

The ballistic neutron guide is followed by a neutron velocity selector which will be discussed in more detail in the following section. The selector has to be placed downstream from the adiabatic "re-compression" of the neutrons in the H112 guide, because the maximum

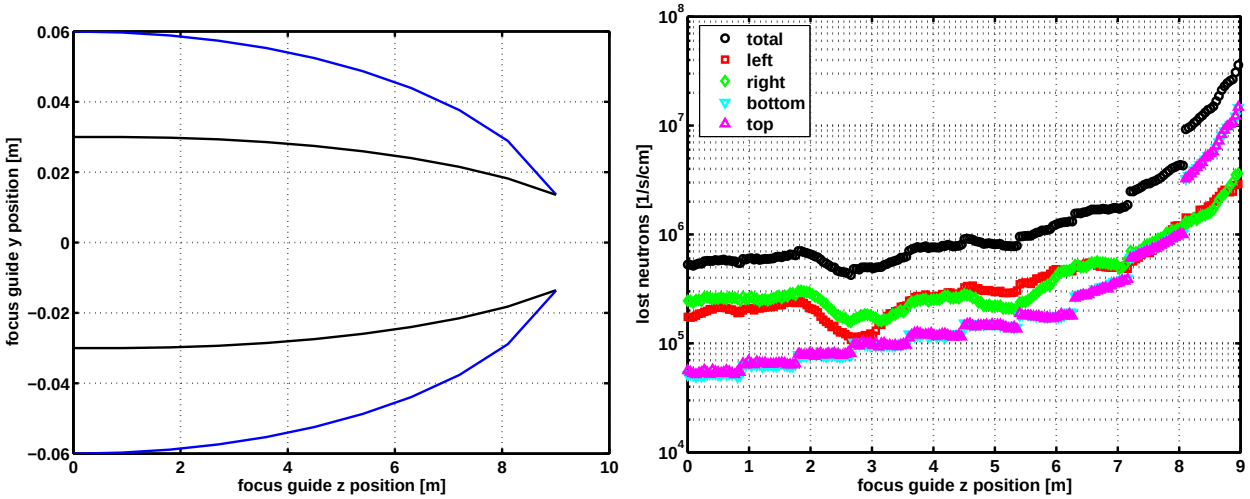

Figure 6.3: Left: Sketch of the layout of an elliptical focus guide, approximated by a polygon consisting of 10 straight segments of equal length. The total length in this example is 9 m. The actual IN16B focus guide in the final design will be shorter (7 m) for optimized performance at the employed wavelengths. The two pairs of lines denote the horizontal (black) and vertical (blue) dimensions of the guide, respectively. Right: Neutrons lost per cm and second along the optical axis of the FG for the layout sketched in the left part of the figure. The total loss (black circles) as well as the losses on each individual wall are given (assumption: $m = 3.5$ coating with a maximum reflectivity of 95%). (Figure from [18])

guide cross section that can be transported through a selector is technically limited.

The velocity selector is followed by a focus guide, which compresses the guide cross section of 115 by 60 mm down to the spot size desired at the sample, 27 by 27 mm. The focus guide has an elliptical shape (figure 6.3, left), and in the final design, which slightly differs from figure 6.3, a length of 7 m has been chosen. The layout of the focus guide, thus, is a compromise to accommodate both the Si(111) and Si(311) crystal configurations of IN16B. The focus guide with an $m = 3.5$-coating near the tip can be expected to have a transmission between 50 % and 60 % of the incoming neutrons for both crystal configurations. Most of the neutron losses are generated near the tip of the focus guide, i.e. near the phase space transformer (figure 6.3, right). This poses a challenge to the shielding of both the focus guide and the phase space transformer.

6.3 Neutron velocity selector design criteria

In parallel to an optimized guide filling at the desired wavelength range, neutrons outside the useful wavelength range (resulting from ΔE_i in chapter 5) must be suppressed in order to reduce the background scattering at the spectrometer, which is achieved by a neutron velocity selector. The neutron velocity selector is a high-speed rotor drum carrying radial neutron adsorbing blades resembling in its layout to the wheel of a worm gear. The neutron optical axis is parallel to the drum axis, and the selector is non-transparent at standstill. When the selector is operated, its rotation frequency is set such that the position of the blades is constant in the rest system of any neutron having the desired speed in the laboratory system to be selected, whilst neutrons having a speed sufficiently far from the desired speed are absorbed by the moving blades [18]. As a result solely the neutrons in a certain speed range (wavelength range) given by the geometrical properties, for instance the angular acceptance

given by the distance of the blades, are selected. For further details, we refer to the dedicated studies published in Refs. [57, 174, 10]. Here we only note that for the purposes of an optimized instrument design, the following observations are relevant:

1) The peak transmission of a neutron velocity selector is essentially defined by its rotation frequency: The higher the rotation frequency, the higher the transmission. Thus, in order to optimize the instrument for two distinct wavelength ranges, namely the Si(111) and Si(311) configurations, two velocity selectors will be necessary. Both selectors run at the highest achievable rotation speed, respectively, and differ only in the blade screw angle and possibly the number of blades. As a compromise, a selector running at the speed limit at the shorter wavelength can be used at the longer wavelength by turning more slowly at the cost of a reduced performance.

2) The blade fixation and thus the maximum radial blade length, as well as the maximum rotor mass are technically limited. The limit for the radial blade length restricts the guide cross section at the selector position to 12 cm height and 6 cm width. For cost reasons due to the standard size available for the glass supports, the neutron guide H112 will have a height of 115 mm at the selector entrance.

Figure 5.7(left) depicts an example transmission spectrum of a selector optimized within the assumed manufacturing constraints using McStas for the Si(111) setup of IN16B on H112 as described in the previous sections. The peak transmission in this case is approximately 72%, the selector spins at 26000 rotations per minute, and the screw angle is 61.8°. For the Si(311) setup, the best screw angle is 34.3° with all other parameters unchanged. Due to the lower divergence in the guide at the shorter wavelength, the peak transmission then is 82%, whilst due to the higher neutron velocity, the width of the transmitted spectrum approximately doubles.

6.4 Expected backscattering instrument performance

Absolute flux numbers at neutron instruments are difficult to predict from numerical simulations, because the spectral distribution of the neutron source is not accurately known (see section 6.1). The Monte Carlo simulations for IN16B predict that on the order of 10^{10}n/s can be delivered through the tip of the focus guide towards the Phase Space Transformer in the Si(111) configuration. This number is integrated over the focus guide tip surface section area ($27 \times 27\,\mathrm{mm}^2$). It takes into account an upstream background chopper duty cycle of 50 % and is not weighted by the gold foil activation spectral sensitivity, but gives the absolute number of neutrons. At the sample position of IN16B, a flux of 2 to 2.5 $\times\, 10^6$n/cm^2 in the Si(111) configuration can be deduced from the simulation for the beam center (area $1\,\mathrm{cm}^2$) in an idealized situation neglecting significant losses from window materials, crystal reflectivity, and air scattering. A comparable number for the related instrument SPHERES has been reported as 8×10^5n/cm^2/s [66]. It is emphasized that the aforementioned losses due to window materials and other elements such as slits limiting the beam size in the secondary spectrometer cannot be predicted easily, and flux estimates in the secondary spectrometer are therefore significantly more difficult than in the primary spectrometer. It is further emphasized that the average flux integrated over the entire spot size at the sample position is evidently considerably lower than the center flux due to the approximately Gaussian beam profile. In addition, the spot size and therefore the flux at the sample position depend on the position of the Doppler monochromator.

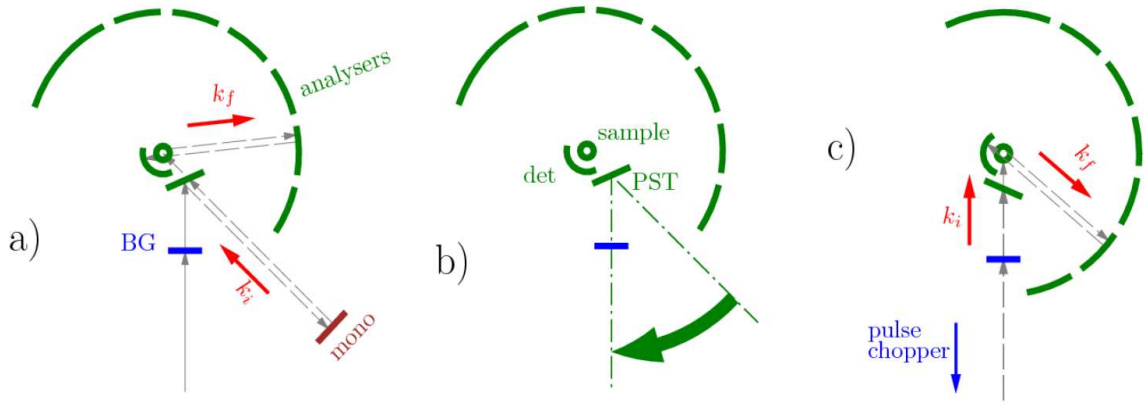

Figure 6.4: Schematic of the BATS transformation: a) Top view of the IN16B backscattering spectrometer in the standard high-resolution configuration which uses the PST and the Doppler monochromator (BG denotes background chopper); b) rotation of the secondary spectrometer and removal of the Doppler drive; c) IN16B in the BATS mode where the incoming beam is shaped by an upstream pulse chopper (not shown). (Figure from [167])

6.5 Future extension: The BATS transformation

Benefiting from the neutron guide end position, IN16B can in the future be upgraded by a time-of-flight option. This option becomes possible by the so-called BATS transformation [167] (BATS: Backscattering and Time-of-Flight Spectroscopy). The BATS transformation is a rotation of the IN16B secondary spectrometer around the PST vertical axis such that the incident beam hits the sample directly through the PST chopper and does not pass via the Doppler monochromator anymore (figure 6.4). The Doppler monochromator, Doppler machine and flight tube are therefore removed prior to the transformation. The incident wavelength is instead defined by a pulse chopper further upstream in the H112 guide. The pulses generated by this upstream chopper become broader in time over the distance to the sample position due to the neutron dispersion relation (figure 6.5, top). In this way, a continuous wavelength band illuminates the sample consecutively, with the shortest wavelength arriving first and the longest last. The maximum wavelength range is limited by the condition of no overlap between different pulses. This condition allows to associate the detected neutrons with their corresponding incident wavelength. To limit the wavelength range in accordance with the no-overlap condition, a bandwidth chopper is required near the sample position. This role can be taken by either the background chopper or the PST chopper. The maximum incident neutron pulse length in the BATS mode is given by the $2 \cdot 2\,\mathrm{m}$ path length from the sample to the analyzers and back, which for the Si(111)-setup is 6.34 ms. The condition of no overlap also defines the position of the pulse chopper in the H112 guide to be 33 m upstream from the sample (figure 6.5, top) [167].

An important question is how IN16B in the BATS mode would compete with equivalent inverted-geometry time-of-flight backscattering spectrometers at spallation neutron sources. An estimate of the neutron flux which may be expected at the sample position of IN16B in the BATS mode can be obtained based on the detailed Monte-Carlo simulations for the cold source, H112 guide, selector, and focus guide as described in the previous sections. The resulting simulated flux in the BATS mode at the sample position is depicted in figure 6.5 (bottom). It is noted that for this simulation, no modifications to the focus guide

were assumed. Since the focus guide is optimized for the PST, a focus guide extension to bring the focus guide end closer to the sample position would further enhance the per-area flux in the BATS mode. The flux at BASIS is given as $5 \cdot 10^4\,\mathrm{n/s/cm^2/\mu eV}$ (resolution $\Delta E \approx 3.5\,\mu$eV FWHM) [102]. The estimated achievable flux at IN16B in the BATS mode (figure 6.5, bottom) is, thus, evidently lower than at BASIS. Nevertheless, the BATS mode will still be very useful, since it can be combined at the same instrument during one experiment with the high-resolution setup of IN16B. The resolution function of IN16B in the BATS mode can be expected to be broader but also to have a higher symmetry than the resolution function of BASIS [167], because the BATS mode will operate in exact backscattering at the analyzers. This resolution function partly explains the significantly lower flux of BATS compared to BASIS, because the primary and secondary spectrometer resolution functions are not well matched in the BATS mode. The second reason for the lower flux of the BATS mode compared to BASIS is the non-optimal use of a continuous neutron source with a pulse chopper at BATS, whilst BASIS is optimized to the source pulse time structure of a spallation source. Importantly, the future BATS mode can help to significantly increase the dynamic range from $-34\mu\mathrm{eV} < E < +34\mu\mathrm{eV}$ in the standard high-resolution setup (see section 4.2) to $-250\mu\mathrm{eV} < E < +250\mu\mathrm{eV}$ (figure 6.5). Evidently, this increase comes at the expense of a broader, but acceptable resolution. By combining both modes, BATS and standard IN16B, samples can in the future be studied with an unparalleled (Q, ω)-range. The BATS mode will close the gap in (Q, ω) towards time-of-flight spectrometers (cf. section 3.1) and for instance allow to determine elastic incoherent structure factors (cf. section 2.7) with unprecedented precision.

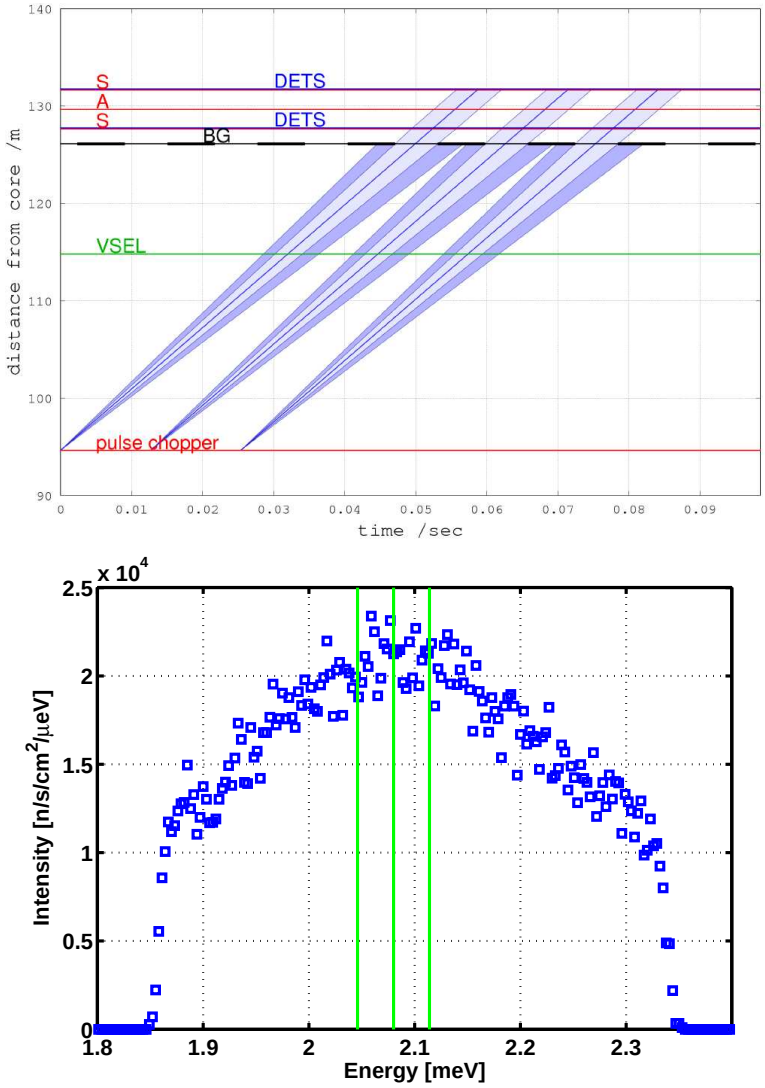

Figure 6.5: Top: Time-distance-diagram for a hypothetical future time-of-flight ("BATS") mode of IN16B using Si(111) analyzer crystals. "S" abbreviates sample, "A" analyzer, "D" detector. "BG" marks the position of the background chopper which in this scheme takes on the role of the bandwidth chopper. "VSEL" denotes the velocity selector. (Figure from [167]) Bottom: Simulated neutron flux at the sample position in the BATS mode using Si(111) analyzer crystals. The vertical lines mark the elastic energy and energy range of the Si(111) Doppler monochromator, respectively. (A better flux/resolution compromise would decrease the average BATS flux to $1.1 \cdot 10^4\,\mathrm{n/cm^2/s/\mu eV}$ at $\Delta E \approx 11\,\mu$eV FWHM [167].)

Chapter 7

In situ experimental techniques

In situ combinations of neutron spectroscopy and other experimental techniques are required when the state of a sample cannot otherwise be known with sufficient accuracy from *ex situ* measurements, e.g. near phase boundaries. Also, when the state of the sample cannot be controlled by standard parameters such as the temperature, pressure, or magnetic field, innovative new sample environments are necessary. Previous research has for instance addressed rheological properties by an *in situ* combination of a flow cell and neutron spectroscopy [177]. The present chapter presents the examples of *in situ* optical spectroscopy and *in situ* tensile testing. One of the technical challenges thereby consists in the vacuum that surrounds most sample environments in neutron spectrometers for background reduction (see also figure 4.3). Soft-matter samples rarely require extreme conditions such as extraordinarily low temperatures. By contrast, they do impose extraordinary stability requirements.

7.1 *In situ* optical spectroscopy

7.1.1 Motivation

Biomolecules such as proteins form some of the most complex entities known. They do this at near ambient temperature and pressure, and self-organization and self-assembly is controlled by "soft" parameters such as interface charge distributions, humidity conditions or concentration in aqueous solution, and ion distributions.

Although establishing ambient temperature and humidity conditions appears trivial, the understanding of for instance protein diffusion or more generally transport processes is severely limited by the nowadays achievable accuracy in defining "ambient" environmental conditions. For example, the accuracy with which the volume occupied by a protein in aqueous solution can be determined up to now is still not sufficient. This limitation restricts the verification of colloid theories, which in turn limits the understanding of diffusion and transport processes in biological systems and thus of biological function at a fundamental yet biomedically relevant level.

It is therefore desirable to combine optical spectroscopy techniques which can characterize the state of a soft matter and in particular biomolecular sample *in situ* with neutron techniques. These optical spectroscopy techniques are for instance UV/vis absorption spectroscopy, infrared, and Raman spectroscopy. The *in situ* combination of neutron and Raman spectroscopy has recently been achieved for the first time at the ISIS facility [3]. A valuable experimental approach will be the *in situ* monitoring of the protein folding state with optical spectroscopy, in particular infrared and Raman techniques, during neutron spectroscopy experiments. The essential role of the protein folding state at ambient conditions is illus-

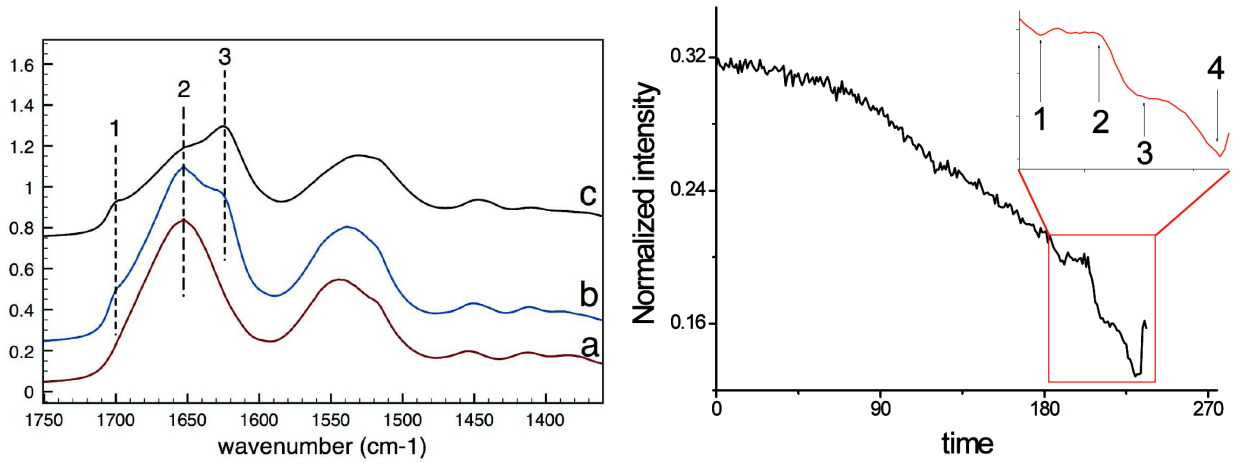

Figure 7.1: Left: FTIR spectra of a fresh silk protein film partially hydrated at ambient atmosphere: after humidification (a); after 3 h at 310 K (b); and after 1 h at 380 K (c). There is a progressive conversion to the β-sheet state (lines 1 and 3) accompanied with a dehydration (line 2). Right: Plot of the elastic scattering intensity recorded on IN10 as a function of time on ambient-humidity silk protein films. The sample temperature was continuously increased from approximately 10 K to 310 K during approximately 12 h. The temperature was subsequently kept constant between the point (1) to (2) at 310 K for 1h. A gain of elastic intensity over time at constant temperature is thus observed. This observation is associated with protein α-helix to β-sheet conversion. Between (2) and (3) the temperature was again increased. Waiting 1 h at (3) at 340 K resulted in no further gain of elastic intensity. Waiting another 1 h at (4) at 380K resulted in more gain of elastic intensity due to protein degradation/water removal. (Figure from [35])

trated by the example of silk proteins. Silk formation is a self-assembly process where a semi-crystalline nanocomposite fiber forms from an aqueous protein solution [36, 128, 172]. Protein aggregation and α-helix to β-sheet conformation transitions contribute essentially to this process and can be monitored using infrared spectroscopy (Figure 7.1, left). Depending on the humidity and temperature of amorphous silk protein films, the amorphous protein α-helices in the silk films convert into semi-crystalline β-sheet structures. This conversion can also be observed using neutron backscattering spectroscopy (Figure 7.1, right), where the silk conversion has a clear effect on the elastic scattering signal. By an *in situ* combination of neutron spectroscopy and infrared spectroscopy, it will in the future be possible to monitor the folding state of the silk proteins and record quasi-elastic data. This will allow to observe the role of water during the conversion process. The hypothesis is that water diffusing on nanosecond time scales plays an essential role in the α-helix to β-sheet conversion in silk fibers. Understanding the self-organisation of silk proteins from aqueous solution in the silk glands of a silkworm or spider towards a hierarchically structured nanocomposite material is of considerable scientific interest. Related topics will therefore be discussed in the sections 8.3 and 8.5.

A second example of the scientific motivation to implement *in situ* optical spectroscopy is given by the phenomenon of the liquid-liquid phase separation (LLPS). This critical behaviour of binary mixtures has been reported for proteins in aqueous salt solutions [77, 182] (see also section 8.5.2 and in particular figure 8.7). The LLPS in protein solutions is extremely sensitive to the parameters protein volume fraction φ, temperature T, and salt concentration in the solution c, such that a parallel photon optical observation of the sample

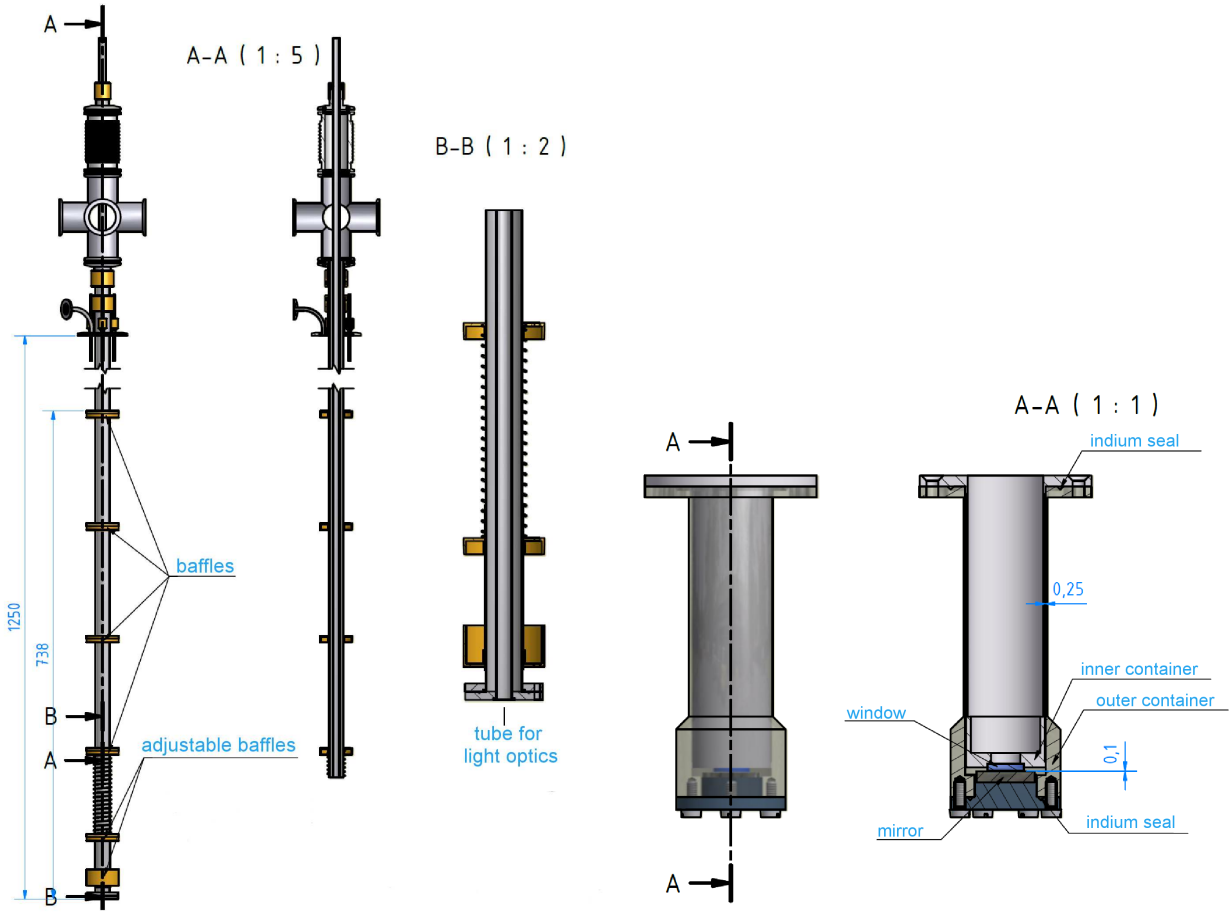

Figure 7.2: Technical drawings of a cryostat center stick (left) and sample holder (right) for *in situ* optical spectroscopy (drawings by A. Treftz, University of Tübingen; reproduction not drawn to scale). The center stick allows for inserting an optical fiber to couple UV/Vis, Infrared, or Raman spectrometers to the sample. The corresponding sample holder for liquid samples (right) is a double-walled Aluminum cylinder where the sample fills the space between the cylinder walls at the sides and at the bottom. The neutron scattering plane is horizontal, and the light scattering experiment is carried out in parallel in the vertical direction, i.e. parallel to the cylinder axis. For this purpose, an optical window and a mirror are inserted in the inner and outer cylinder, respectively.

state during a neutron spectroscopy experiment would be very useful. A deeper understanding of the LLPS may have an important impact in the pursuit to control protein aggregation and protein crystallization.

7.1.2 Approaches to an implementation

In an ongoing project [1], a suitable *in situ* combination of neutron and optical spectroscopy techniques is being developed (figure 7.2). For this purpose, a cryostat center stick (figure 7.2, left) compatible with all standard cryostats has been constructed, which can be used on virtually any neutron spectrometer. This center stick contains a double-walled tube which is temperature-controlled to ambient temperature and thermally insulated against the cold

[1] Collaboration between the ILL (T. Seydel et al.), the Institute for Applied Physics at the University of Tübingen (F. Schreiber, F. Zhang et al.), and the Department of Physical Chemistry at the University of Oxford (R. Jacobs et al.)

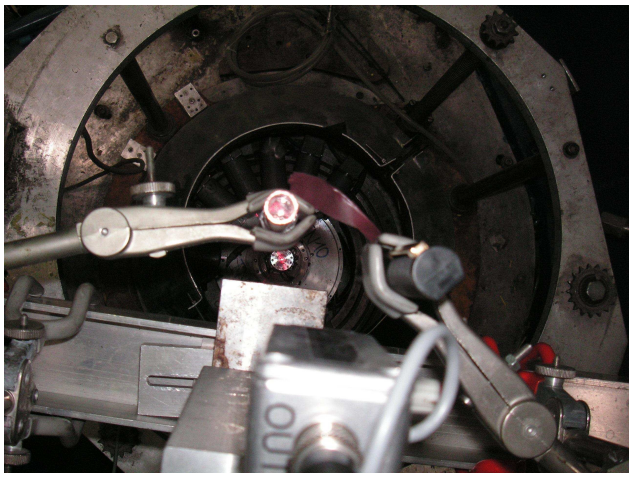

Figure 7.3: Photograph of an optical test setup mounted on top of the instrument platform of the neutron backscattering spectrometer IN10: Top view of the light scattering setup on IN10. The two light spots visible on the photograph mark the optical mirror of the sample cell (see Fig. 7.2, right) which is mounted on the sample table of the spectrometer and a focusing lens in the foreground, respectively. The neutron scattering plane is in the image plane approximately 2 m below the foreground items. (Figure from [140])

cryostat well. This setup allows to insert fragile optical fibers and, thus, to place fiber optical probes next to the sample container on the neutron instrument. A compatible sample container for liquid solution samples has also been developed (figure 7.2, right), which allows for the combination of optical and neutron techniques. The container holds the solution sample between the double walls of the cylinder. The neutrons are scattered in the plane perpendicular to the cylinder axis, whilst the photons follow a backscattering optical path parallel to the cylinder axis. The photon window therefore does not interfere with the neutrons which are transmitted through the Aluminum cylinder walls. The backscattering of the photons can be enhanced by a suitable optical mirror placed inside at the bottom of the outer cylinder. The photon optical gap filled with the liquid sample solution can be varied simply using spacers at the top flange. This does not affect the neutron optical gap between the vertical cylinder walls. In the event that the focal length of the optical beam is shorter than the sample cylinder height, the sample cylinder can also be constructed in an "upside down" configuration where the photon optical window is located on the outer cylinder face. A photograph of a makeshift test setup of the optical sample cell (figure 7.2, right) is depicted in figure 7.3. Additional work will be necessary to fulfill the mechanical stability and precision requirements for the photon optical parts to carry out reliable experiments.

7.2 *In situ* tensile testing and humidity control

Using *in situ* tensile testing, neutron diffraction, small-angle scattering, and spectroscopy techniques can be used to explore the link between the mechanical and the morphological properties of materials. In combination with x-ray diffraction techniques, these investigations for instance contribute to the materials science of wood and silk [111]. In materials where the mechanical properties strongly depend on the amount of adsorbed water, such as silk fibers, an additional control of the environmental humidity level is important. The *in situ* combination of tensile testing, humidity control, and neutron scattering has been achieved

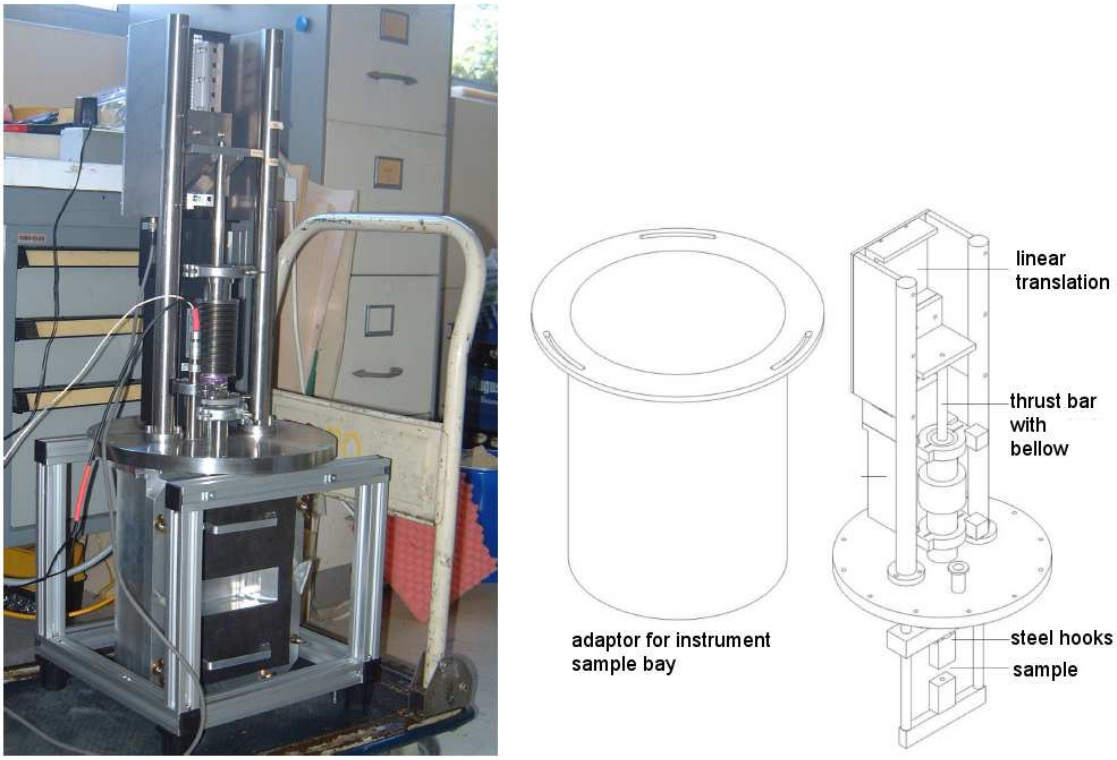

Figure 7.4: Left: Photograph of the tensile machine for *in situ* neutron scattering experiments on fibre materials (see also figure 7.5). The humidity chamber holding the sample is at the bottom. The black neutron-absorbing B_4C cover leaves a rectangular entrance window for the neutron beam. The circular steel flange above the humidity chamber seals the tensile machine such that the humidity chamber is surrounded by the vacuum of the neutron spectrometer sample bay. Right: Schematic explaining some of the components of the tensile machine. The cylindrical adaptor to the spectrometer sample bay has been removed for the photograph. (Figure from [87])

recently [87, 143], figures 7.4 and 7.5. This setup is based on an earlier version combining neutron spectroscopy and tensile testing in vacuum only [88]. It comprises a computer-controlled tensile machine which can generate a tensile force of up to 2500 N and record stress-strain curves *in situ* during the neutron experiment. The fiber sample is therefore held by steel hooks. For a typical neutron spectroscopy experiment, approximately 200 mg of fiber material are required, which translate into on the order of 12000 turns around these hooks, or 1.2 km of fiber for a typical silkworm. For the operation of this setup on a neutron time-of-flight spectrometer, the humidity chamber which contains the tensile apparatus is sealed against the outside vacuum of the spectrometer sample bay. The humidity chamber is designed such that the path of the neutron beam through the humid air inside the chamber is as short as possible to minimize the scattering by the air. The chamber accommodates humidity and temperature sensors. Small troughs containing pure water or saturated salt solutions in water, respectively, define the humidity. More information on silk fibers studied using this tensile humidity chamber will be provided in section 8.3.

A further step into the future will be an accurate control of the amount of water absorbed by the sample through absorption isotherms. This future setup is not trivial to implement due to the temperature-stability requirements of the absorption apparatus.

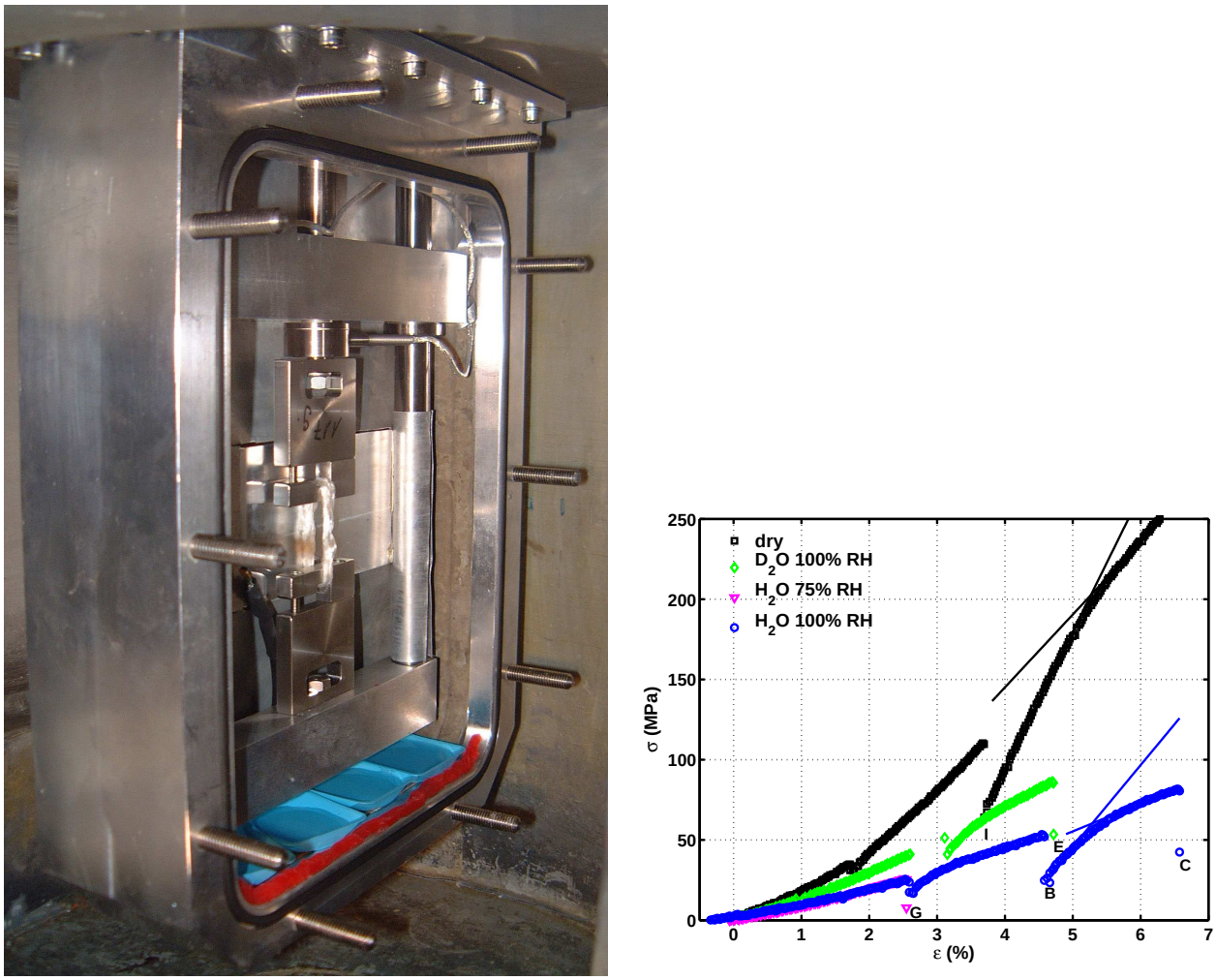

Figure 7.5: Left: Photograph of a silk sample (white fiber bundle in the center of the image) inside the humidity chamber for *in situ* tensile testing mounted inside the sample bay of the time-of-flight spectrometer IN6. The chamber (see also Fig. 7.4) is shown with the front cover removed. The force sensor is visible as a cylindrical metal structure on the upper center of the photograph with the signal cable arriving from the right. The neutron beam impinges on the sample horizontally, arriving from the right edge of the photograph. The blue plastic troughs at the bottom of the chamber contain pure water or saturated salt solutions, respectively, to define the humidity inside the chamber. The edge-to-edge distance between the steel hooks holding the fiber bundle is 3 cm. Right: Stress-strain curves obtained *in situ* during the IN6 experiment using the apparatus depicted in the left part of the figure (humidities see legend). TOF data have been recorded at the positions on the stress-strain curves marked by the capital letters and at $\epsilon \approx 0$ [143]. During these recordings the otherwise continuous tensile elongation was interrupted, resulting in the observed relaxations in the tensile stress σ. The solid lines are linear fits to determine the mechanical moduli. (Figure from [143])

Chapter 8

Examples of application - past, present, and future

A classical application of neutron backscattering is the study of quantum rotational tunneling [123], which is still being used in present times [75, 124]. Highest-resolution inelastic spectroscopy further serves to explore hyperfine interactions (e.g. [26]). Also, the elastic scattering intensity, which can be recorded at an extremely high energy resolution using backscattering spectrometers, provides a wealth of information, e.g. in biological physics [42, 178]. Further, using the elastic intensity, surface adsorption phenomena can efficiently be studied (see e.g. [9, 119]). This holds even more if the information from incoherent elastic scattering can be enhanced by *in situ* diffraction [28]. The above examples are given to emphasize that backscattering spectrometers are not only used to study diffusion, which is in the focus of the present review. Applications mostly addressing diffusion processes include diffusion in inorganic solids (e.g. [33], for a textbook see [69]), in polymers [159], micellar systems [152], thin films on solid surfaces [9], diffusion of proteins in solution [134], membrane fluctuations [132, 129], diffusion in nanoporous media such as zeolites [79, 80], and other complex materials such as clays [61, 17], and also adsorbate surface diffusion on large effective surfaces of powders [23]. Most samples studied in neutron backscattering are in a liquid, amorphous, polycrystalline powder, or otherwise disordered state. Notable exceptions concern for instance lipid membranes, which have been studied in a quasi-2D geometry (see section 8.2). The advent of higher flux backscattering instruments may help to study further systems with higher order.

8.1 Diffusion in general

Backscattering spectrometers are a prime tool to study diffusion on nanosecond time scales and nanometer length scales, as already mentioned in chapter 2 along with the basic concepts of diffusion. Diffusion is the main transport process at low Reynolds numbers [125], and understanding diffusion is essential for understanding interactions in condensed matter. Through nuclear incoherent scattering, backscattering spectrometers can provide an unambiguous access to the self-diffusion in samples with a predominant incoherent scattering cross section. Conversely, collective diffusion phenomena can be accessed in samples with a significant coherent scattering cross section. Understanding and discriminating collective diffusion and self-diffusion in complex media such as membranes, fibers, or colloidal suspensions and biological colloids as e.g. protein solutions is of great current interest. Also, understanding different time scales of interactions and their limiting cases, namely short-time diffusion and

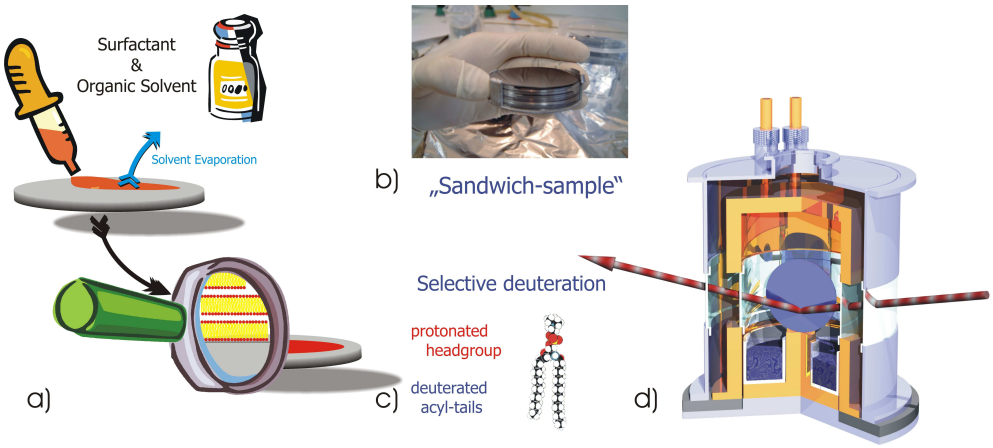

Figure 8.1: Illustration explaining the preparation of oriented stacks of lipid bilayers used in neutron spectroscopy experiments: (a) Sketch of the deposition of lipids from liquid solution on a silicon wafer. (b) Photograph of the "sandwich sample" consisting of a stack of typically 10 to 50 silicon wafers used for the neutron experiments. (c) By selective deuteration, the collective motions of the acyl tails are enhanced over other contributions to the inelastic scattering cross section. (d) Schematic of a humidity chamber that allows controlling temperature and humidity of the bilayers. (Figure from [131])

long-time diffusion (see chapter 2), is crucial to address for instance biological transport processes. The following sections present example sample systems that have a large potential for further research in the future. All example samples are soft-matter systems which are inspired by biological systems and in which diffusion plays an essential role. Regarding these examples, high-resolution spectroscopy has contributed and will further contribute important knowledge. Abstracting from a biological cell as prime biological entity, an understanding of the fluctuations of the outer cell membrane is pursued based on simplified lipid model membranes. This topic will be discussed in the following section 8.2. Subsequently, in section 8.3 we address an example material, silk, which is made up solely of proteins as one of the basic biological building blocks. Here, it is assumed that diffusion will provide a key to understanding mechanical properties. We then return to biological cells and consider the fact that the interior of such a cell predominantly consists of water which serves as a solvent for various intracellular molecules. It is of prime importance to study the behavior of the solvent water in the presence of large molecules which are suspended in it. Gels represent extremely simplified models for this purpose which may provide further understanding regarding the intracellular matrix [166]. Following the discussion of an example gel in section 8.4, the situation of macromolecular crowding inside biological cells will be addressed in section 8.5. Again, diffusion plays a pivotal role, since the transport of macromolecules inside biological cells influences reaction kinetics and information exchange. It turns out that the diffusion of macromolecules is strongly influenced already on nanosecond time scales by the presence of other macromolecules, which together occupy a significant volume fraction of the interior of a cell [135] (subsection 8.5.1). The fundamental role of charges in solution in influencing protein aggregation will be briefly addressed in the subsection 8.5.2. Finally, the access to thermal vibrational and internal diffusive modes using neutron backscattering in protein solutions and related systems will be addressed in the subsection 8.5.3. This latter access is fundamentally linked to an accurate knowledge of the center-of-mass diffusion in solution.

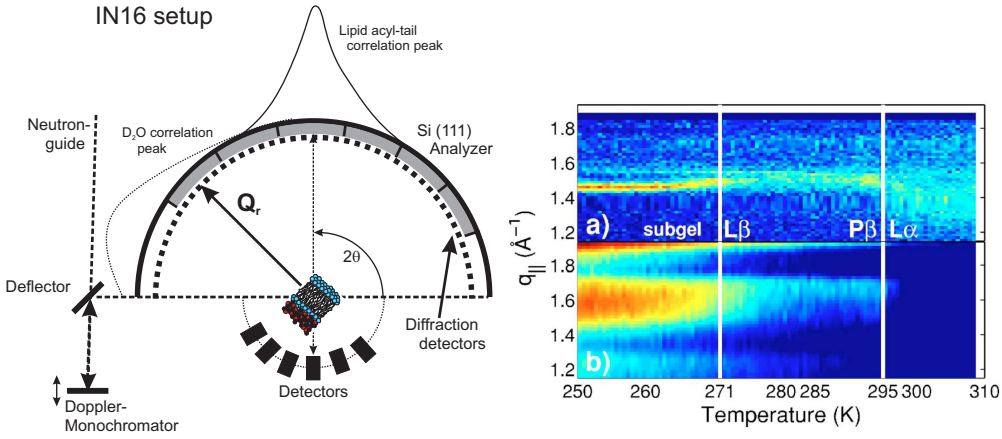

Figure 8.2: Left: Schematic of the scattering geometry (not drawn to scale) for the study of oriented lipid membranes in a backscattering spectrometer. The sample is mounted with the membrane planes vertical, i.e., perpendicular to the horizontal scattering plane of the backscattering spectrometer. The membrane planes are oriented at well-defined angles with respect to the incident beam. The lipid tail inter-acyl-chain correlation peak in the plane of the membranes is located at $Q_r = 1.42\,\text{Å}^{-1}$. Spatially arranged analyzers at a sample-to-crystal distance of 1.5 m (IN10) or 2 m (IN16), respectively, allow to separately but simultaneously probe the dynamics on different length scales. The bulk heavy water correlation peak, which occurs at $Q_r = 2\,\text{Å}^{-1}$, is indicated by the dotted line. (Figure adapted from [130]) Right: IN16 data – a) Energy-integrated diffraction for temperatures 250 K$< T <$ 310 K with a temperature resolution of $\Delta T = 0.3$ K normalized to acquisition time. q is the in-plane component of the scattering vector $\mathbf{Q}$. The phase boundaries for gel Lβ, ripple Pβ', and fluid phase Lα as defined by structural changes, i.e., the change of peak position and width, are marked by the solid white lines. b) Elastic scattering, measured with an energy resolution of 0.9 μeV. The phase transitions are also visible in the energy-resolved diffraction data by following the melting at the lipid acyl chain and water positions. The data are normalized to the incident beam monitor and to the detector efficiency obtained from the scattering signal of a 2-mm-thick vanadium plate oriented at 135° with respect to the incoming beam. Please note that no absorption correction has been done. For geometrical reasons the diffraction detectors have a lower maximum q than the backscattering detectors. (Figure from [132])

8.2 Lipid membranes

Lipid membranes constitute the multi-functional barrier that separates the interior of living cells from the environment. Biological membranes thereby control and regulate the transport of ions and macromolecules into and out of the cell. It is assumed that membrane fluctuations play an essential role in controlling the transport processes and also signal transduction.

A recent achievement using neutron backscattering experiments consists in measuring on aligned and oriented membranes supported by Silicon wafers [130, 132, 129]. This type of geometry is known for a long time from x-ray and neutron reflectivity measurements, where static horizontal and lateral correlations can be recorded. To record quasi-elastic or inelastic scattering data on these oriented samples, large stacks of lipid bilayer films have to be prepared to obtain a sufficient scattering volume (Figure 8.1). Approximately 10 to 50 thin Si-wafers are stacked for this purpose, and each of these Si-wafers supports on the order of 1000 lipid bilayers which form by self-organisation from a solution deposited on the wafer surface [112].

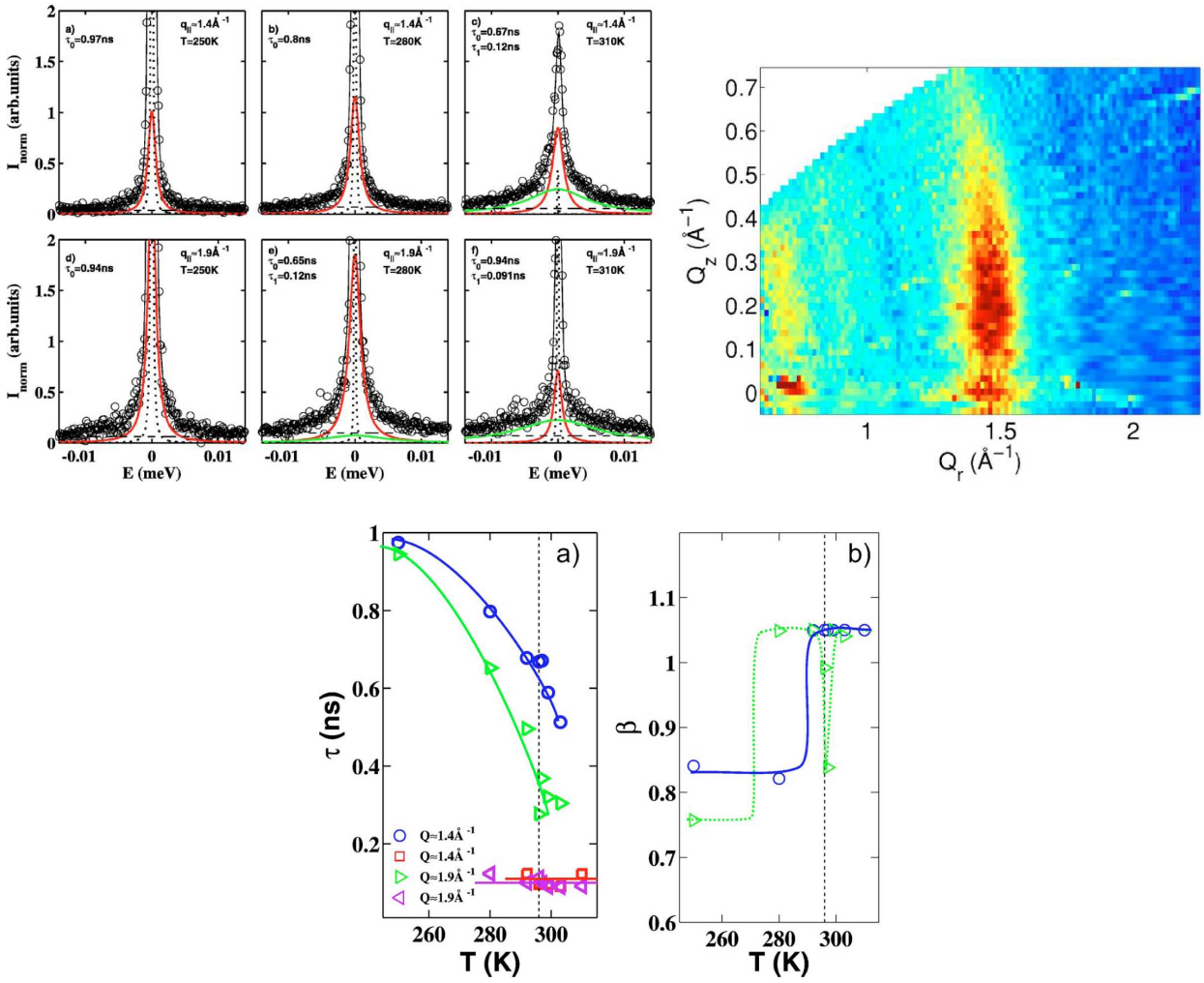

Figure 8.3: Top left: IN16 backscattering data recorded on oriented lipid membranes (figure 8.1) at the positions of the lipid chain ($q_{||} \approx 1.4\,\text{Å}^{-1}$) and water ($q_{||} \approx 1.9\,\text{Å}^{-1}$) correlations, respectively, for temperatures T=250 K, 280 K and 310 K. Detectors have been grouped to increase counting statistics. The lipid tail inter-acyl chain correlation peak is measured by detectors 9-13 (out of 20), which cover a $q_{||}$ range of $1.20\text{Å}^{-1} < q_{||} < 1.60\text{Å}^{-1}$. The water contribution is recorded by detectors 17-20 covering $1.78\text{Å}^{-1} < q_{||} < 1.94\text{Å}^{-1}$. As a model, up to two Lorentzian peak profiles (red and green lines) to describe the quasi-elastic broadening and a Dirac function (dotted line) to describe the elastic intensity were assumed. This model was convoluted with the measured resolution function obtained from a Vanadium standard. A flat background (dashed line) was subsequently added and the result was fitted (fit result: black solid line) to the data (circles). The thus obtained relaxation times are summarized in the bottom part of the figure, (a). The calibration error of the energy scale is approximately 3%. (Figure from [132]) Top right: Diffraction data of a hydrated sample at 18° C recorded on a triple-axis instrument. The correlation peak of the acyl-chains exhibits the shape of a slightly bent Bragg rod, reflecting the quasi-two-dimensional liquid-like short range correlations of the acyl-chain positions. Undulation modes are probed at $q_z = 0$ while at finite q_z contribution, baroclinic modes are probed. The diffraction data have been taken from Ref. [130]. Bottom: (a) Relaxation times at the lipid chain and the water position for all measured temperatures as determined from fits to the quasi elastic data shown in the top left part of the figure. (b) Exponents β of the exponential decay $\exp\left[-(t/\tau)^{\beta}\right]$ as determined from fits of the intermediate scattering function. Solid lines are guides to the eye. (Figure from [132])

The wafers are held in place by spacers and contained in a humidity chamber or other appropriate sealed sample container. When the lipid molecules are at least partially deuterated to give rise to a sufficiently large coherent scattering signal, the recorded signal depends on the orientation of the stacked lipid sample with respect to the beam, i.e. the isotropy of a powder sample is lost.

Using these stacked samples, collective motions parallel to the membrane plane and perpendicular to the membrane plane can therefore be discriminated in the backscattering spectra (Figure 8.2). For this purpose, the sample is measured at two different orientations relative to the incident beam (Figure 8.2, left). The orientation is chosen such that the scattering vector $\mathbf{q}$ is nearly parallel or perpendicular to the membrane surfaces, respectively. Using partially deuterated lipids (DMPC-d54) and hydration with heavy water (D_2O), the lipid acyl-tail correlation peak and the broad D_2O correlation peak can then be detected at an in-plane scattering vector $q_{||} \approx 1.4\,\text{Å}^{-1}$ and $q_{||} \approx 2\,\text{Å}^{-1}$, respectively. When the scattering signal is detected as a function of the sample temperature, a shift of the lipid acyl correlation peak can be observed in the energy-integrated diffraction pattern (Figure 8.2, right). The elastic energy window scan in parallel provides information on immobile-to-mobile phase transitions. Note that the D_2O nearest-neighbor structural correlation peak is isotropic, i.e. it can be detected independently from the sample orientation. The quasi-elastic linewidth at the D_2O correlation peak position is equally isotropic. By contrast, the quasi-elastic linewidths from the oriented, partially deuterated lipid samples become distinctly sensitive to the sample orientation at scattering vectors near the lipid-tail structural correlation peak (figure 8.3). This observation confirms that collective diffusion modes of the lipid tails parallel to the membrane plane can be detected. By combining structural information with neutron backscattering data and computer simulations, correlated dynamics over several lipid distances can be quantified [129]. The lipid samples can be doted with other molecules such as cholesterol, and the effect of such guest molecules which integrate in the membranes can be studied [22].

8.3 Nanocomposite polymer systems, silk fibers

Nanocomposite polymer systems – in nature being represented by for instance collagen and silk fibers and in technology by car tires and nylon fibers – are of prime interest in materials science due to their superior mechanical properties as opposed to homogeneous materials. Understanding the molecular mobility in these systems in addition of their microscopic and mesoscopic structure may help to enhance the understanding of the mechanical properties. This holds in particular for example for silk fibers – which are protein materials –, where adsorbed water molecules change the mechanical properties (see Fig. 7.5, right). On a macroscopic scale, humid silk fibers become more rubber-like compared to dry silk fibers, i.e. their stress-strain curve changes significantly (Fig. 7.5). Physically, the mechanical response at least of dry silk fibers is in agreement with the model of entropy elasticity [62, 148]. In silk fibers, adsorbed water molecules can in parallel be used as spectroscopic probes. Water acts as a plasticizer in most H-bonded polymers and proteins (see e.g. [161]). This plasticizing effect is easily illustrated by an elastic window scan versus the sample temperature on a backscattering spectrometer using a silk sample at different humidities (Figure 8.4). In addition, water selectively only accesses the amorphous regions in semicrystalline nanocomposite polymer materials such as in particular cellulose and silk [110, 144]. Neutron spectroscopy combined with structural information obtained *in situ* by neutron diffraction and *ex situ* by x-ray diffraction can be used to access mechanical function [89, 138, 144, 143]. The neutron

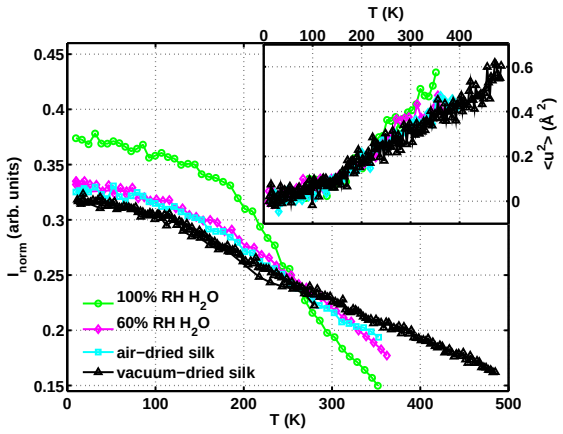

Figure 8.4: Elastic scattering intensities from silkworm silk fibers recorded on the backscattering spectrometer IN10 within the $1\,\mu$eV energy resolution window, integrated over all detectors ($0.4\,\text{Å}^{-1} < Q < 1.9\,\text{Å}^{-1}$). All data have been taken on the same silk sample, and the differences in the intensities at the lowest temperature are therefore a measure of the water contents. The humidity of the sample was defined *ex situ* by a storage in an atmosphere with the relative humidity RH as given in the legend. Inset: Apparent mean-squared displacements $\langle u^2 \rangle$ calculated from the Q-dependence of the intensities $I(Q)$ according to $I(Q) \propto \exp\left(-\frac{1}{3}\langle u^2 \rangle Q^2\right)$. (Figure from [143])

spectroscopy experiments provide information on the dynamical response of the polymer fibers under tensile strain, which can be applied *in situ* [144, 143] (Figure 7.5). The results on humid silk fibers indicate faster relaxations of the confined water and polymer side groups when tensile strain is applied [143]. These results can be seen in the context of other work on "soft confinement", which seems to generally induce faster relaxation [184]. The results on the diffusion in a confined geometry inside water-plastizised silk fibers [143] have been interpreted in terms of standard models for motion in confinement. Future analysis will take into account recent models for fractional Brownian dynamics in proteins [86].

8.4 Colloidal suspensions and gels

When colloid particles are suspended in a liquid solution, the motion of the colloid particles is strongly affected by the occupied volume fraction and by the surface charge pattern of the suspended particles (see section 8.5).

In some cases, suitable colloid particles – denoted gelators – can immobilize the solvent fluid on a macroscopic scale to form so-called gels. Gels have semi-solid mechanical properties and emerge over time from the precursor-stage, the so-called sol, if the gelator concentration is sufficiently high. The sol has the mechanical properties of a highly viscous liquid. Usually, the sol-gel transition can be reversed by an adequate mechanical stimulus (e.g. stirring). The macroscopic immobilization of the solvent fluid in a gel is reflected by a solid-like mechanical modulus, and the gel can in several cases be formed with a remarkably low mass fraction of the gelator [59]. Gelators can consist of inorganic materials such as clay minerals or organic materials such as polymers. For instance, laponite clay mineral nano-particles can immobilize water to form gels at a laponite mass fraction of 2.5 wt.% or less [169, 109] (figure 8.5, left), and these samples can be investigated by both surface-sensitive and bulk neutron scattering [158, 148]. Remarkably, the self-diffusion of the solvent water as detected

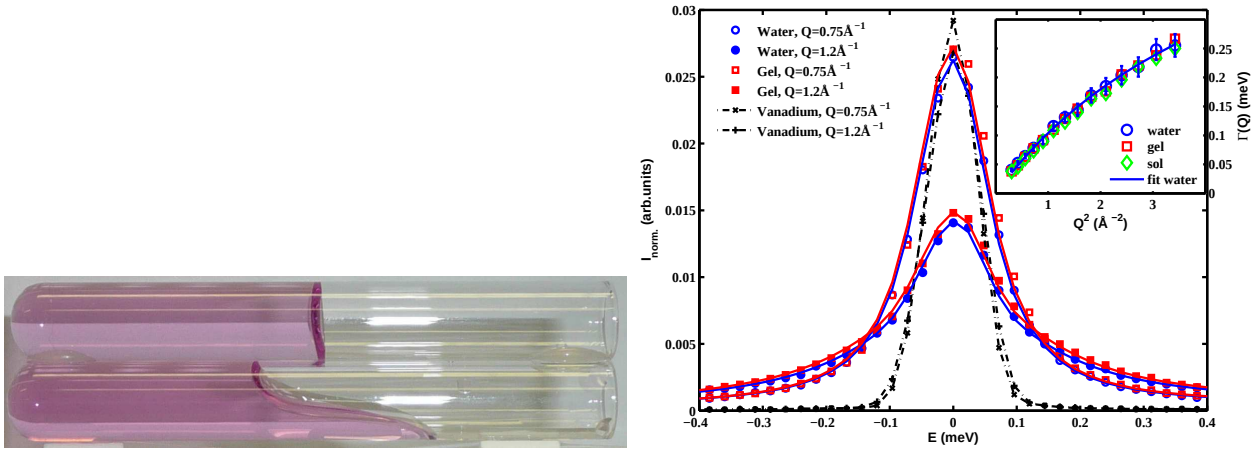

Figure 8.5: Left: Photograph of a suspension of 2 wt.% laponite nanoparticles in water (top), and of a suspension of 1.2 wt.% laponite in water (bottom). The samples were colored with $KMnO_4$ for better visibility. The direction of gravity being perpendicular to the test tube cylinder axis, the photograph illustrates that the 2 wt.% suspension forms a semisolid material – denoted a gel –, while the 1.2 wt.% suspension remains in a highly viscous sol state on the observation time scale on the order of a day. Right: Quasi-elastic scattering from water (circle symbols), and 2wt.% mineral gel samples (square symbols), respectively, and corresponding fits of a jump-diffusion model (solid lines), for two different scattering vectors Q (open and filled symbols). The data were recorded on the time-of-flight spectrometer FOCUS, PSI, Switzerland. The respective instrumental resolution measured by the scattering from vanadium is given in addition (dash-dotted lines). The fit results for the half-width at half maximum (HWHM) of the single Lorentzian function assumed in the model are given in the inset, completed by the result for the 1.2wt.% mineral sol. (Sample temperature $T = 285\,\mathrm{K}$.) (Figure from [148])

by neutron spectroscopy in a scattering vector range of $0.4 < Q/\text{Å} < 2.1$ thereby remains unaffected [148] in the case of laponite gels (figure 8.5, right). In a different example gel system, a so-called nanotube gel based on bile acid, the self-diffusion of the solvent molecules seems to become even slightly faster compared to the pure-solvent reference system [175].

Gels can be responsive to temperature [136]. So-called supramolecular gels also have the ability of immobilizing large amounts of solvent, for instance ethanol-water mixtures, at very low supramolecular volume fractions below 1 % [121]. Applications of such bio-compatible gels can be seen in controlled drug delivery (see e.g. [149]). All the above observations suggest that gel systems need further investigation by incoherent neutron spectroscopy. It is thereby particularly interesting that gels may represent extremely simplified model systems of the intracellular matrix of biological cells [166]. The absence of an effect of the presence of macromolecules on the solvent self-diffusion on molecular length scales has also been observed in biological cells [78].

8.5 Proteins in crowded electrolyte solutions

Moving from gel systems as potential models to comprehend the intracellular solvent diffusion to the macromolecules suspended in such solvents, we here address the topic of macromolecular crowding in aqueous solution. The mobility of hydrated proteins has been investigated comprehensively using neutron backscattering (see e.g. [42, 58, 178]). However, in these

samples the proteins do not undergo any center-of-mass diffusion. By contrast, the present and likely future research focus shifts towards aqueous solution samples. The biological motivation for the study of solution samples arises from the "crowded" solution character of the interior of biological cells. In the intracellular medium, macromolecules and in particular globular proteins occur at volume fractions typically around 40 % [47]. This macromolecular crowding can be assumed to have important implications on transport phenomena and reaction kinetics inside biological cells.

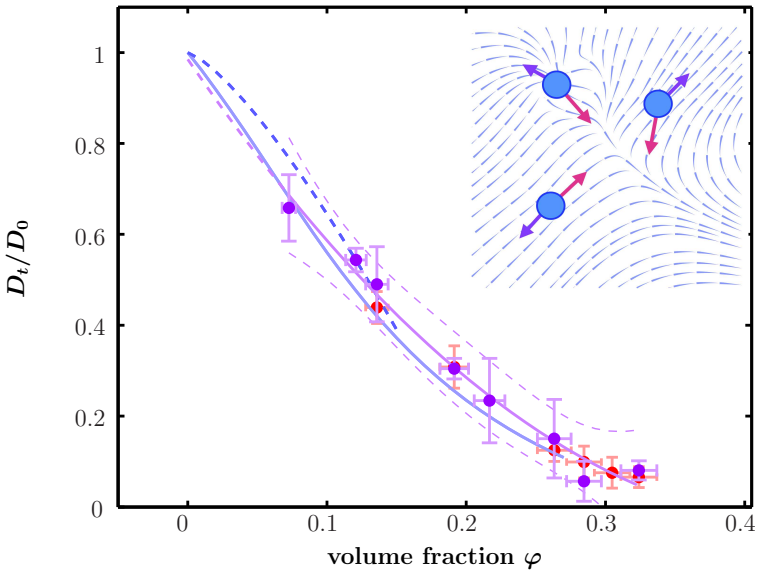

Figure 8.6: Normalized translational self-diffusion coefficients $D_t/D_t(0)$ (circles) of BSA proteins in water (D_2O) as a function of the protein volume fraction φ for two different temperatures (red and purple circles denote 280 and 300 K, respectively) after separation of the rotational contributions. The purple line superimposed on the data is a guide to the eye obtained from a polynomial fit indicating a temperature-independent mastercurve. The upper and lower dashed purple lines indicate the upper and lower 96% prediction bounds, respectively. The blue lines denote the colloidal short-time self-diffusion for hard spheres (light blue, solid) and charged spheres (dark blue, dashed). The inset in the upper right corner illustrates the flow field (light blue stream line plot) generated by the movement of three spheres (velocities are denoted by blue arrows) and therefore experiencing a hydrodynamic force (pink arrows). (Figure from [135])

8.5.1 Protein self-diffusion and colloid physics

Aqueous solutions or suspensions of proteins can be discussed in terms of colloid physics [120]. Pioneering work in terms of interpreting the quasi-elastic neutron scattering data from proteins in solution has been achieved by Pérez et al. [115]. Amongst the most important functions in colloid physics is the dependence of the translational self-diffusion $D_t(\varphi)$ on the volume fraction φ occupied by the colloidal particles. This function can be analytically derived for colloidal suspensions of hard spheres for both the short-time and long-time limits of the self-diffusion [164]. The first step in discussing the behaviour of proteins in aqueous solutions in terms of colloid physics [134] is to compare their diffusion behaviour with charge-stabilized colloid suspensions [113]. The globular protein *Bovine serum albumin* (BSA) in aqueous solution provides a very robust example of a charge-stabilized suspension as long as

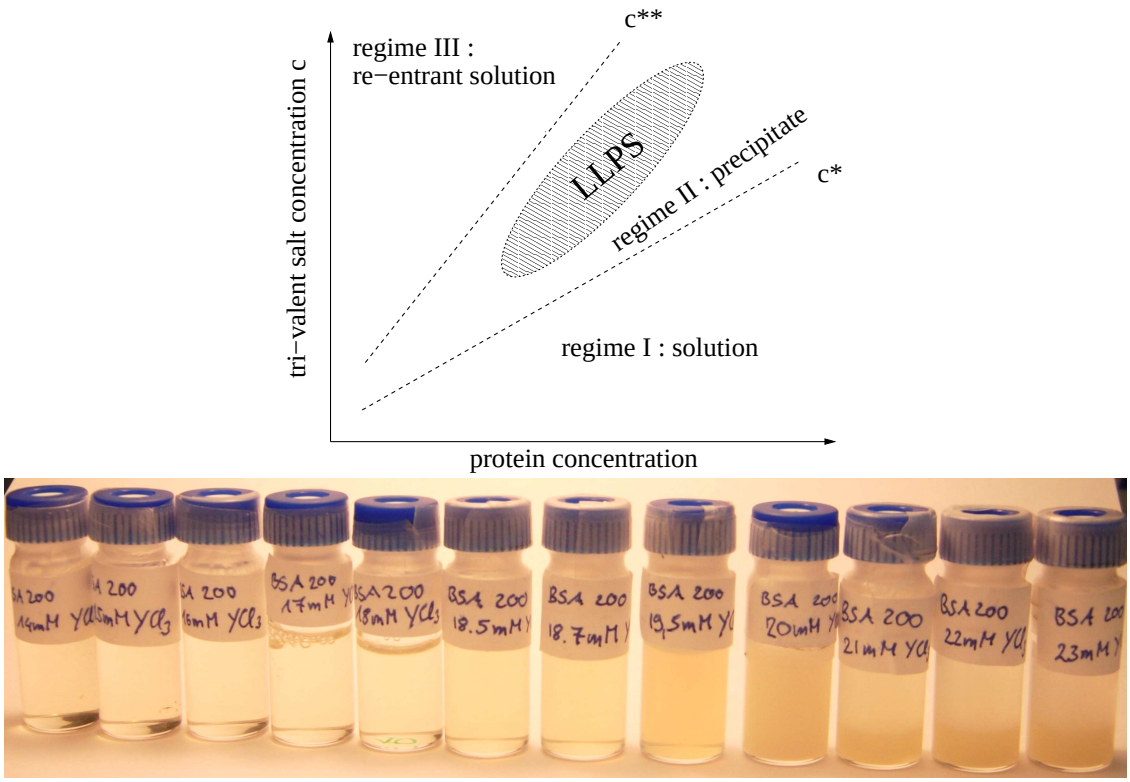

Figure 8.7: Top: Approximate sketch of a phase diagram of BSA proteins in aqueous solution according to [180, 179]. BSA is fully dissolved in the regimes I and III and precipitates in regime II. The regime I is characterized by predominant repulsive interactions. By contrast, in regime II, attractive interactions prevail, and a liquid-liquid phase separation (LLPS) [179] can be observed. The regime III is denoted the re-entrant regime. The critical salt concentrations c^* and c^{**}, respectively, mark the transitions between the different regimes. Both depend on the protein volume fraction, i.e. $c^* = c^*(\varphi)$. Bottom: Photograph of a BSA protein solution at 200mg/ml in D_2O at different YCl_3 salt concentrations showing the transition from a colloidal suspension to a precipitate regime, corresponding to the transition from regime I to regime II, i.e. crossing the phase separation line $c^* = c^*(\varphi)$ in the top part of the figure.

no salts are added to the suspension. For this system, a systematic study of the dependence on the protein translational self-diffusion coefficient D_t on the volume fraction φ occupied by the proteins has recently been carried out [71, 135] (see also figure 4.4 and its discussion in section 4.3). The experimental results $D_t(\varphi)$ for the soft non-spherically shaped proteins have been compared with the predictions from colloid theory for hard-sphere suspensions. By a geometrical transformation of the complex protein shape including its hydration shell to effective spheres, an accurate calibration of the volume fraction φ occupied by the proteins can be achieved. A perfect agreement of experiment and theory for the short-time self-diffusion (cf. chapter 2) has thus been confirmed [71, 135] (figure 8.6). The normalized translational self-diffusion coefficient $D_t(\varphi)/D_t(0)$ with the dilute-limit diffusion coefficient $D_0 := D_t(0)$ thus seems to follow a temperature-independent master curve at physiological temperatures (figure 8.6). It is evident from this work [135] that the translational diffusion coefficient is slowed down drastically by the effect of macromolecular crowding already on nanosecond time scales. This slowing-down has implications regarding physiological transport processes and signal transduction in living cells. Further, the perfect quantitative

agreement of the experiment for protein solutions with the colloid theory for hard spheres confirms the applicability of these theories on nanometer length scales. Remarkably, these neutron backscattering experiments thus prove that the diffusion of soft proteins with an inhomogeneous shape and surface charge pattern can be quantitatively understood in terms of relatively simple models for hard spheres. For this work on the protein self-diffusion under macromolecular crowding conditions, it was essential to accurately model the shape of the protein using small-angle x-ray scattering data. This modeling is the prerequisite to calibrate the volume fraction occupied by the proteins in the solution, which is essential for the comparison with colloid theory. Further, dynamic light scattering data are required to normalize the diffusion coefficients to the dilute limit. This underlines that various types of experiments are routinely necessary to explore a particular system in soft-matter science.

Remarkably, the global short-time diffusion D of the BSA proteins in water can be described by simple Brownian diffusion in this study [134] (see also figure 4.4). Backscattering spectrometers with an increased dynamic range will allow to test up to which temperature this description holds. They will also allow to access more dilute protein solutions, which will be important to discriminate colloid hard-sphere models for non-charged and charged spheres, respectively, within the experimental accuracy. Such experiment options are given at BASIS [101] and also motivate the implementation of the future BATS option for IN16B (section 6.5). It is emphasized that in the previous study on BSA protein solutions [134], the same protein serves both as crowding agent and as tracer particle. Higher flux backscattering spectrometers may in the future also allow to investigate the effect of external crowders, where the tracer particle and the crowding agent are different macromolecules.

8.5.2 Effects of charge, ion valency, and pH

The interior of living cells is characterized not only by macromolecular crowding but also by the presence of salt ions. Suitable charges induced by salt ions or pH can affect the phase diagram of proteins in solution crucially. For instance, it has been shown that the presence of the three-valent salt YCl_3 can induce critical phenomena such as the transition from solution to precipitate regimes of the model protein *Bovine serum albumin* (figure 8.7) [180]. With rising salt concentration, the system leaves the precipitate regime and re-enters an aqueous solution regime. The rising YCl_3-concentration induces an increasing charge-screening. The re-entrance regime is governed by a charge inversion of the proteins by a binding of multivalent counterions [180]. The characteristics of the phase diagram depicted in figure 8.7 can be assumed to hold for a large class of proteins [181].

Within the precipitate regime, a liquid-liquid phase separation [77, 179] can be observed (figure 8.7). Such complex phase diagrams suggest that charges can be assumed to play an important role in tuning biological interactions. The complex surface charge patterns of proteins strongly influence the protein-salt interactions. Also, clustering phenomena are relevant for understanding protein aggregation and crystallization. The formation of dynamic lysozyme protein clusters has been found recently using neutron spectroscopy [122]. Recent experiments indicate the presence of dynamic density fluctuations or clusters also for aqueous *Bovine serum albumin* protein solutions containing YCl_3 ions [71]. These fluctuations can give rise to local crowding and the formation of protein nanoclusters. Dynamic clusters may be a precursor to protein crystal formation. Future systematic studies applying charge-tuning to various aqueous protein-salt solutions will allow to comprehend the phase diagrams in detail. The focus of neutron spectroscopy studies will thereby be on the protein cluster size, density, and life-time as a function of protein and salt concentration in the solution, and the possible existence of universal scaling laws in the spirit of theories of

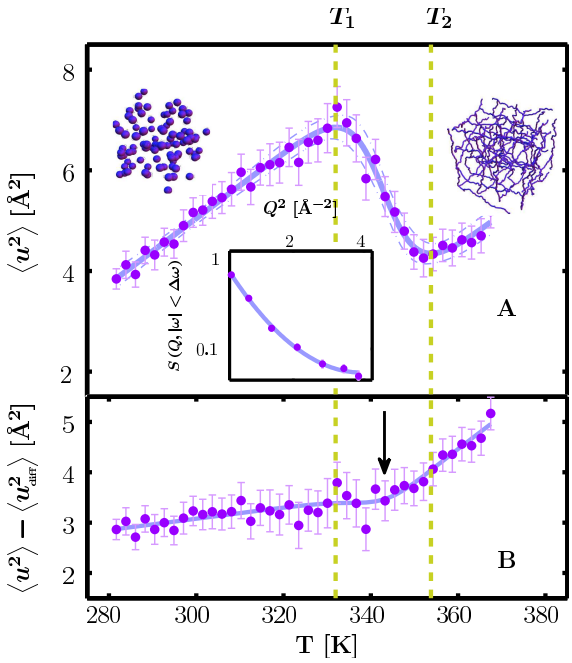

Figure 8.8: (A) Total mean-squared displacement $\langle u^2 \rangle$ (circles) of an aqueous (D_2O) BSA protein solution (concentration 500 mg/ml) versus temperature T. The solution was heated at $7.4 \cdot 10^{-2}$ K/min. Using a phenomenological model [73] we describe the data (solid line superimposed on the data) and determine the denaturing interval $T_1 < T < T_2$ (dotted vertical lines). The upper images illustrate a colloidal suspension of native proteins (left) and the cross-linked network of denatured proteins (right). Inset: Measured elastic intensity $S(Q, |\omega| < \Delta\omega)$ versus Q^2 (circles) for the same sample at $T = 290$ K recorded at IN10. A quadratic fit [73] (solid line) was used to determine $\langle u^2 \rangle$. (B) $\langle u^2 \rangle - \langle u^2_{\rm diff} \rangle$ (circles), where $\langle u^2_{\rm diff} \rangle$ accounts for the apparent mean-squared displacement due to global diffusion in solution and has been obtained using neutron backscattering QENS data [73]. The transition regime from native to denatured proteins is denoted by the two vertical dashed lines. At $T_0 = (T_1 + T_2)/2$ a transition occurs, characterized by a kink in the curve (arrow). (Figure from [73])

dynamic critical phenomena [74] may be explored. Understanding the dynamic aspects of protein cluster formation and crystallization will contribute to understand aggregation phenomena for instance in silks, which are semicrystalline protein materials spun from aqueous solution [172] (see section 8.3), and other biological systems. Progress in this field may also help to elucidate pathological pathways in protein aggregate formation.

8.5.3 Unfolding and denaturing

Understanding protein folding poses one of the largest challenges in biological physics. The reverse process of protein unfolding from the native state toward and beyond the denaturing can be easily experimentally controlled and may be worth some further considerations. In particular, the reverse process can be closely monitored with various spectroscopy techniques. When a globular protein denatures, the associated unfolding is accompanied by a transition of the protein polypeptide chains from a helical to a random coil conformation [183]. The change in the conformation induces distinct changes in the protein subunit diffusion which can be resolved using neutron spectroscopy [71]. Further, depending on the

protein concentration in solution, vulcanization [32] or gelation may occur upon denaturing, since the unraveling polypeptide chains may crosslink. The conceptual link of the study of protein denaturing with the investigation of macromolecular crowding (see subsection 8.5.1) is important, since crowding is known to induce dramatic effects on the thermodynamics of denaturing [156]. Thus, crowding tends to entropically stabilize proteins and increase their denaturing temperature. Neutron backscattering can therefore be assumed to contribute importantly to the understanding of protein motion in solution near the denaturing transition. By separating different dynamic modes, namely the center-of-mass diffusion of the proteins in solution as well as the protein internal modes (both diffusive and vibrational), a framework can be provided to extract the purely vibrational modes of a denaturing protein in solution [73]. This framework is based on the scattering function for diffusing proteins in aqueous solution [73] assuming uncoupled diffusing and vibrational modes [41],

$$\begin{aligned} S(Q,\omega) &= \exp\left(-\frac{1}{3}\langle u^2_{\mathrm{vib}}\rangle Q^2\right)\mathcal{L}(\omega,\gamma) \\ &\quad \otimes\left\{A(Q)\,\delta(\omega)+[1-A(Q)]\,\mathcal{L}_\beta(\omega,\Gamma)\right\}, \end{aligned} \tag{8.1}$$

where $\langle u^2_{\mathrm{vib}}\rangle$ denotes the mean-squared displacement from vibrational modes, $A(Q)$ the elastic incoherent structure factor, $\mathcal{L}$ the Lorentzian describing the convolution of rotational and translational diffusion, and $\mathcal{L}_\beta$ a Kohlrausch-Williams-Watts function accounting for internal relaxation modes [73]. The experimentally observed apparent mean-squared displacement $\langle u^2\rangle = \langle u^2_{vib}\rangle + \langle u^2_{sub}\rangle + \left\langle u^2_{\mathrm{d}iff}\right\rangle$ recorded by fixed elastic-window scans (see section 4.3) consists of the contributions $\langle u^2_{vib}\rangle$ from vibrations, $\langle u^2_{sub}\rangle$ from internal relaxation modes, and $\left\langle u^2_{\mathrm{d}iff}\right\rangle$ from the global rotation and translation diffusion in solution. These contributions can be decomposed quantitatively using the new analytical framework by Hennig et al. [73] (figure 8.8). In figure 8.8, the application of this framework serves to illustrate the thermal denaturing of BSA proteins in an aqueous solution. The accurate knowledge of the self-diffusion of the proteins obtained from neutron backscattering QENS data (subsection 8.5.1) and of the elastic scattering obtained from backscattering fixed window data are both essential to extract and separate off the purely vibrational signal of a protein (figure 8.8) [73]. In the future, systematic studies to investigate the denaturing temperature as a function of the protein and salt concentration will be possible using this framework. The framework will also allow to deconvolute time-of-flight spectroscopy data, such that the center-of-mass motion of proteins can be separated from protein internal relaxation and vibration modes. This possibility points towards a further understanding of the elastic incoherent structure factor of proteins in solution [137]. The separation of internal modes from neutron spectroscopy data on solution samples will also simplify the comparison with molecular dynamics (MD) simulations by circumventing the necessity to simulate also the global motion of the proteins in solution. Ultimately, the accurate access to internal modes of motion of proteins in solution will permit to address configuration entropies.

Chapter 9

Perspectives

Soft condensed matter science and the understanding of disordered systems are amongst the large scientific challenges of the 21st century. Notably, living systems are based on disorder as well as on non-equilibrium phenomena [40]. In particular regarding disordered systems, a better understanding will certainly not rely solely on methods resolving structural information. Methods disclosing the molecular motion will be equally essential, and a direct access to intermolecular interactions through incoherent neutron scattering will be amongst these methods. Self-diffusion as probed by incoherent quasi-elastic neutron scattering provides such information on interaction. Biological function, transport processes, membrane transduction and also the transport of information in biological systems are essentially defined as dynamic phenomena governed to a large extent by diffusion. The unique direct access to self-diffusion complements the information on collective diffusion obtained at comparatively small scattering vectors using dynamic light scattering in the visible (DLS) and x-ray (XPCS) wavelength range, and also using spin-echo techniques. It is noted that with the latter, an approximation of the self-diffusion can be obtained at large scattering vectors. In comparison with many other techniques which can obtain equivalent results in suitable conditions, neutrons display a particularly robust character. All light scattering methods are sensitive to the stability and cleanliness of the entire experimental setup. This demand affects the requirements on the thermal stability of monochromators, mirrors and other components in the case of x-ray experiments and invokes a sensitivity to individual grains of dust in the case of visible light. By contrast, neutron techniques are rather insensitive to such instabilities and impurities. In comparison with Raman scattering, the absence of heat load on the sample in the case of neutrons is worth being highlighted. Soft-matter samples are often characterized by the absence of a long-range order. As noted in section 2.7, a particular strength of incoherent neutron spectroscopy in soft matter science is therefore that the method is sensitive to the local order of a sample. It is emphasized that incoherent neutron spectroscopy is rarely used as the only technique applied on a system. In the particular case of most of the examples presented in chapter 8, amongst others small-angle x-ray scattering is an essential complement (for a review on SAXS, see e.g. [114] and references therein).

9.1 Future science using neutron backscattering

Proteins are one prime example of soft-matter systems. Protein diffusion in aqueous solution under the conditions of molecular crowding is at the foundations of the function of biological cells. Protein diffusion is not only affected by the protein volume fraction in solution, but also by the ionic strength, and – remarkably – valency, of salts present in the

solution. Some multivalent salts such as YCl_3 can thus induce complex phase diagrams in some protein solutions such as those of *Bovine Serum Albumin*. These phase diagrams are characterized by precipitate and reentrance regimes [180], and the understanding of the parameters controlling the phase diagrams may have a fundamental impact for instance on understanding protein aggregation and crystallization. The effective hydrodynamic radius of the proteins with their hydration shells and surface charges plays an essential role in this context. The self-diffusion is the only model-free access to determine the hydrodynamic radius, and therefore neutron backscattering will be indispensable in exploring phase diagrams of protein solutions. The self-diffusion provides a unique access to interactions of proteins and other nanoscale colloidal particles in solution [7]. The recent work in the context of the PhD thesis by M. Hennig [71] points towards the future importance of charge tuning and charge-controlled interactions of proteins. For instance, protein clusters have initially been studied using static methods [157]. Phenomena such as transient or dynamic clusters of proteins forming in aqueous solutions can only be understood on the basis of neutron spectroscopic investigations [122]. Dynamic clusters can be assumed to have an impact on protein aggregation. Further, protein folding can also be understood only as a dynamic phenomenon, where it will be interesting to study the reverse process, i.e. protein unfolding, with spectroscopic methods. Here, neutron backscattering can provide information on the subunit diffusion of proteins as a function of temperature. The prominent topic of protein aggregation, besides its importance in achieving protein single crystals for structure determination, is also relevant in many biological processes such as silk fiber formation, and equally concerns pathological pathways known in medicine.

In the experimental "neighborhood" complementing the neutron backscattering technique, noteworthy methods are neutron spin-echo spectroscopy, dynamic light scattering using visible and x-ray photons, and nuclear magnetic resonance techniques. Also using future dynamic x-ray scattering experiments, the nanosecond dynamic window to investigate self-diffusion will probably remain unique to neutron methods. As static methods, x-ray and neutron diffraction and small-angle scattering experiments provide important complementary structural information. These and other methods are routinely combined to address questions in soft matter science. For instance, whilst opaque materials such as crowded colloidal suspensions are inaccessible by light scattering techniques, the latter can access the dilute-limit diffusion constant D_0. D_0 in turn is difficult to access by neutron techniques due to the insufficient neutron flux. SAXS and SANS techniques give access to nanoscale colloidal structure and form factors and to the osmotic compressibility, which are essential parameters to compare measured diffusion constants with colloid theory.

Nuclear magnetic resonance techniques (NMR) also have to be mentioned in the experimental neighborhood of neutron backscattering. Although NMR is not a scattering technique, it has some formal similarity [50] in that it can detect angle-time correlation functions as opposed to space-time correlation functions. A coordinate transformation then shows that information from NMR can be compared with incoherent neutron spectroscopy data at very small scattering vectors [50].

Future experiments can be expected to combine neutron spectroscopy and other spectroscopy experiments *in situ*. This combination can for instance be relevant if denaturing is observed by a temperature scan recording the elastically scattered neutrons and in parallel determining the characteristic footprint of the protein folding state using infrared or Raman spectroscopy. Both accurate humidity and temperature control are essential to control for instance protein aggregation in protein films. Therefore, an accurate *in situ* humidity control combined with temperature control will play an important role. The most accurate approach to define the humidity of a sample *in situ* would consist in measuring the water

adsorption isotherm when preparing the sample on the neutron spectrometer. Moreover, for some experiments *in situ* mechanical testing will also be of interest.

It is likely that the relevance of surface and interface studies will further increase, covering fields from catalytic chemistry to biological interactions at membranes. Due to the comparatively weak neutron sources, it is not straight-forward to carry out surface-sensitive neutron time-of-flight and backscattering spectroscopy. By contrast, using x-rays in a grazing incidence geometry, both structural and spectroscopic experiments can be carried out [38, 39, 64, 97, 98, 145, 146, 147, 153, 165]. The advantage of x-ray photon correlation spectroscopy (XPCS) is, however, not as significant as it may appear at first glance, since XPCS is a "photon hungry" technique. A correlation function can only be obtained by having a sufficient number of photons in the time interval relevant for the time scale of motion to be observed in a sample. I.e. the faster the motion in the sample, the higher the photon flux needs to be. Further, x-ray sources have an inherent time structure which has to be observed. By contrast, in the to some extent analogous neutron spin-echo technique, in principle only one neutron polarization needs to be successfully measured independent of the time scale of motion observed in a sample. XPCS and neutron spin-echo techniques can be combined to increase the overall dynamic range [150].

Already at present, powder samples with large effective surfaces are used to study for instance surface diffusion phenomena and interatomic potentials relevant in catalytical chemistry using neutron spectroscopy, including neutron backscattering [92, 91]. The use of stacked systems of many parallel surfaces to create a quasi-2D geometry for neutron spectroscopy has been pioneered only recently [112]. In the future, it may be considered whether the latter setups may be enhanced using resonant beam coupling principles. Resonant beam coupling of neutrons to multilayer waveguide structures has been demonstrated by Pfeiffer et al. [118] for alternating Nickel/Carbon multilayers. For this application, the stacked system would essentially need to form an alternating pattern of layers with a very low scattering cross section and layers with a high coherent scattering cross section. The former could consist of silicon when illuminated at a sufficiently large wavelength (e.g. 6.27 Å) in order to not excite Bragg peaks. The latter could be fully deuterated lipid membranes, which give a large critical angle of total external reflection. However, designing a suitable resonant beam coupling device based on soft matter will definitely pose a significant challenge.

9.2 Future backscattering instrument developments

We have reviewed the project of the high-resolution cold neutron backscattering spectrometer IN16B in detail in this work. In the context of the IN16B project, progress in neutron optics has been made by the quantitative understanding of the Phase Space Transformation for divergent neutron beams. IN16B is optimized for a reactor-based continuous neutron source. Hence, IN16B complements medium-resolution backscattering spectrometers at pulsed spallation neutron sources which are optimized for the time structure of the neutron source and therefore make a compromise in the energy resolution. Future backscattering instrument upgrades can include the combination of highest-resolution backscattering as is implemented at reactor-source backscattering spectrometers with a time-of-flight option at a reactor source. The latter closes the gap in the dynamic range towards dedicated time-of-flight spectrometers. Technically, this optional configuration will be achieved by defining a monochromatic incident beam through time-of-flight choppers which replace the Doppler monochromator. The Doppler monochromator as well as the Phase Space Transformer are therefore moved out of the beam path by rotating the secondary spectrometer cabin and putting the PST chopper

disk to an open position. In this way, the incoming TOF-monochromatic beam illuminates the sample directly. The scattered neutrons pass via the analyzer crystals to the detectors in the same way as in the high-resolution Doppler-monochromator setup. This optional future upgrade for IN16B corresponds to backscattering instruments existing at spallation neutron sources such as BASIS at the SNS. A further future upgrade of the backscattering technique consists in implementing neutron polarization analysis. Also, besides the standard Si(111), other monochromator/analyzer crystals such as Si(311) and later GaAs(200) will be included. GaAs(200) crystals, corresponding to an elastic wavelength in backscattering of 5.65 Å, are characterized by a relative extinction width which is by approximately one order of magnitude smaller compared to Si(111) crystals [5, 94]. Thus, GaAs analyzer crystals can be used to achieve a significantly enhanced energy resolution at a Q-range similar to Si(111). By contrast, Si(311) crystals are used to obtain a maximum scattering vector of approximately $3.8\,\text{Å}^{-1}$. This scattering vector can at present only routinely be achieved at the thermal neutron backscattering spectrometer IN13 at the ILL, where a recent example of diffusion in lipid membranes outlines the interest in QENS studies at large Q [8], being, however, limited by the low available flux. IN16B in the Si(311) mode can be expected to significantly outperform IN13 in neutron flux at $Q < 3.8\,\text{Å}^{-1}$. Besides the high-flux options of IN16B using the Phase Space Transformer, an additional optional side position for the secondary spectrometer will be implemented. In this side-position setup, the incident neutrons pass by a deflector crystal before entering the secondary spectrometer. The PST disk then takes on the role of a mere deflector chopper. The side position provides a reduced neutron flux and energy range, but also a reduced background and in combination with optimized deflector crystals a significantly reduced beam divergence. This low-divergence option is suitable for experiments where structure and coherent scattering are important.

9.3 Conclusion

Dynamic phenomena and motion on nanometer length scales in soft matter and biomaterials can be expected to be in the focus of research for many years to come. Future experiments will include membranes, fibers, proteins in solution to test colloid theories, protein denaturing, and many other soft materials of fundamental interest. Systematic experimental studies achieving a quantitative comparison of experiments with theory and simulation will further enhance our fundamental understanding of dynamics-function relationships in biological systems. Here, cold neutron backscattering takes a unique place in a neighborhood of complementary experimental techniques. An example of a very systematic investigation of a sample parameter dependence has very recently been provided by the volume-fraction dependence of the protein self-diffusion in aqueous solutions [135], which agrees quantitatively with predictions from colloid theory. The unique experimental possibilities of neutron backscattering are given by the access to a sub-micro-electron volt energy resolution and, thus, to nanosecond time scales of motion. Backscattering spectrometers reach this high energy resolution in a range of scattering vectors which, depending on the choice of the crystal setup, typically is within $0.2\,\text{Å}^{-1} < Q < 3.8\,\text{Å}^{-1}$. The accessible scattering vectors thus cover nanometer length scales. In this (Q, ω)-range, the elastic incoherent structure factor and the molecular self-diffusion can be detected through incoherent scattering. In addition, the backscattering technique is also sensitive to coherent scattering, which can be applied to detect collective molecular motion. The optimized use of these experimental approaches by backscattering spectrometers with enhanced flux will certainly inspire further new science.

Bibliography

[1] H. Abele, D. Dubbers, H. Häse, M. Klein, A. Knöpfler, M. Kreuz, T. Lauer, B. Märkisch, D. Mund, V. Nesvizhevsky, A. Petoukhov, C. Schmidt, M. Schumann, and T. Soldner. Characterization of a ballistic supermirror neutron guide. *Nuclear Instruments and Methods in Physics Research Section A: Accelerators, Spectrometers, Detectors and Associated Equipment*, 562(1):407 – 417, 2006.

[2] D. Adams. *The long dark tea-time of the soul*. Serious Productions Ltd., Heinemann, London, 1988.

[3] M.A. Adams, S.F. Parker, F. Fernandez-Alonso, D.J. Cutler, C. Hodges, and A. King. Simultaneous neutron scattering and Raman scattering. *Applied Spectroscopy*, 63:727–732, 2009.

[4] B. Alefeld, M. Birr, and A. Heidemann. A new high resolution neutron crystal spectrometer and its application. *Naturwissenschaften*, 56(8):410, 1969.

[5] B. Alefeld, L. Dohmen, and A. Heidemann. GaAs as a backscattering crystal. *Physica B: Condensed Matter*, 283(4):299 – 301, 2000.

[6] K.H. Andersen. private communication, 2010.

[7] T. Ando and J. Skolnick. Crowding and hydrodynamic interactions likely dominate in vivo macromolecular motion. *Proceedings of the National Academy of Sciences (USA)*, 107(43):18457–18462, 2010.

[8] C.L. Armstrong, M. Trapp, J. Peters, T. Seydel, and M.C. Rheinstädter. Short-range ballistic motion in fluid bilayers studied by quasi-elastic neutron scattering. *Soft Matter*, 7:8358, 2011.

[9] T. Arnold, A. Barbour, S. Chanaa, R.E. Cook, D. Fernandez-Canato, P. Landry, T. Seydel, P. Yaron, and J.Z. Larese. Melting of thin films of alkanes on magnesium oxide. *European Journal of Physics - Special Topics*, 167:143–150, 2009.

[10] S. Baechler, N. Kardjilov, M. Dierick, J. Jolie, G. Kühne, E. Lehmann, and T. Materna. New features in cold neutron radiography and tomography: Part I: Thinner scintillators and a neutron velocity selector to improve the spatial resolution. *Nuclear Instruments and Methods in Physics Research Section A: Accelerators, Spectrometers, Detectors and Associated Equipment*, 491(3):481 – 491, 2002.

[11] A.J. Banchio and G. Nägele. Short-time transport properties in dense suspensions: From neutral to charge-stabilized colloidal spheres. *Journal of Chemical Physics*, 128:104903, 2008.

[12] M. Bée. *Quasielastic neutron scattering. Principles and applications in solid state chemistry, biology and materials science.* A. Hilger, Bristol, PA, 1988.

[13] M. Bée. A physical insight into the elastic incoherent structure factor. *Physica B*, 182(4):323–336, 1992.

[14] M. Bée. Localized and long-range diffusion in condensed matter: State of the art of QENS studies and future prospects. *Chemical Physics*, 292:121 – 141, 2003.

[15] M.C. Bellissent-Funel. Status of experiments probing the dynamics of water in confinement. *European Physical Journal E*, 12(1):83–92, 2003.

[16] M. Birr, A. Heidemann, and B. Alefeld. Neutron crystal spectrometer with extremely high energy resolutuion. *Nuclear Instruments & Methods*, 95(3):435, 1971.

[17] H.N. Bordallo, L.P. Aldridge, G.J. Churchman, W.P. Gates, M.T.F. Telling, K. Kiefer, P. Fouquet, T. Seydel, and S.A.J. Kimber. Quasi-elastic neutron scattering studies on clay interlayer-space highlighting the effect of the cation in confined water dynamics. *Journal of Physical Chemistry C*, 112(36):13982–13991, 2008.

[18] H.N. Bordallo, B. Frick, H. Schober, and T. Seydel. Primary spectrometer neutron optics simulations for a new cold neutron backscattering spectrometer. *Journal of Neutron Research*, 16(1):39–54, 2008.

[19] W.L. Bragg. The diffraction of short electromagnetic waves by a crystal. *Proceedings of the Cambridge Philosophical Society*, 17:43 – 57, 1913.

[20] B.N. Brockhouse. Diffusive motions in liquids and neutron scattering. *Physical Review Letters*, 2(7):287–289, 1959.

[21] R. Brown. A brief account of microscopical observations made in the months of June, July and August 1827, on the particles contained in the pollen of plants; and on the general existence of active molecules in organic and inorganic bodies. *Philosophical Magazine Series 2*, 4(21):161 – 173, 1828.

[22] B. Brüning, M.C. Rheinstädter, A. Hiess, B. Weinhausen, T. Reusch, S. Aeffner, and T. Salditt. Influence of cholesterol on the collective dynamics of the phospholipid acyl chains in model membranes. *European Physical Journal E*, 31(4):419–428, 2010.

[23] I. Calvo-Almazán, T. Seydel, and P. Fouquet. Questions arising for future surface diffusion studies using scattering techniques - the case of benzene diffusion on graphite basal plane surfaces. *Journal of Physics - Condensed Matter*, 22(30):304014, 2010.

[24] C.J. Carlile and D.K. Ross. An experimental verification of the Chudley-Elliot model for the diffusion of hydrogen in α-phase Pd/H. *Solid State Communications*, 15(11-12):1923 – 1927, 1974.

[25] J. Chadwick. The existence of a neutron. *Proceedings of the Royal Society of London. Series A*, 136(830):692–708, 1932.

[26] T. Chatterji, J. Combet, B. Frick, and A. Szyula. Direct evidence for the magnetic ordering of Nd ions in $NdMn_2Si_2$ and $NdMn_2Ge_2$ by high resolution inelastic neutron scattering. *Journal of Magnetism and Magnetic Materials*, 324(6):1030 – 1033, 2012.

[27] C.T. Chudley and R.J. Elliott. Neutron scattering from a liquid on a jump diffusion model. *Proceedings of the Physical Society*, 77(2):353, 1961.

[28] S.M. Clarke and T. Arnold. Simultaneous coherent and incoherent neutron scattering of polyalcohols adsorbed on ice. *Applied Physics A - Materials Science & Processing*, 74(Part 2, S):S1371–S1372, 2002. International Conference on Neutron Scattering, Munich, Germany, Sep 09-13, 2001.

[29] J.C. Cook, W. Petry, A. Heidemann, and J.-F. Barthélemy. A dynamic range upgrade for neutron backscattering spectroscopy. *Nuclear Instruments and Methods in Physics Research Section A: Accelerators, Spectrometers, Detectors and Associated Equipment*, 312(3):553 – 560, 1992.

[30] C.G. Darwin. The theory of X-ray reflexion. *Philosophical Magazine Series 6*, 27(158):315–333, 1914.

[31] C.G. Darwin. The theory of X-ray reflexion. Part II. *Philosophical Magazine Series 6*, 27(160):675 – 690, 1914.

[32] P.G. de Gennes. Critical behaviour for vulcanization processes. *Journal de Physique Lettres*, 38(17):355–358, 1977.

[33] F. Demmel, T. Seydel, and S. Jahn. Sodium diffusion in cryolite at elevated temperatures studied by quasielastic neutron scattering. *Solid State Ionics*, 180(23-25):1257–1260, 2009.

[34] J.K.G. Dhont. *An introduction to the dynamics of colloids*. Elsevier Science B.V., Amsterdam, 1996.

[35] C. Dicko, I. Diddens, T. Seydel, A. Terry, and F. Vollrath. Report on experiment 8-04-484 on IN10. Technical report, ILL experimental report, 2008. http://club.ill.fr.

[36] C. Dicko, J.M. Kenney, and F. Vollrath. β-silks: Enhancing and controlling aggregation. In A.V. Kajava, J.M. Squire, and D.A.D. Parry, editors, *Fibrous proteins: Amyloids, prions and beta proteins*, volume 73 of *Advances in Protein Chemistry*, pages 17–53. Elsevier Academic Press, 2006.

[37] S.B. Dierker, R. Pindak, R.M. Fleming, I.K. Robinson, and L. Berman. X-ray photon correlation spectroscopy study of brownian motion of gold colloids in glycerol. *Physical Review Letters*, 75(3):449–452, 1995.

[38] A.K. Doerr, M. Tolan, W. Prange, J.-P. Schlomka, T. Seydel, W. Press, D. Smilgies, and B. Struth. Observation of capillary waves on liquid thin films from mesoscopic to atomic length scales. *Physical Review Letters*, 83(17):3470–3473, 1999.

[39] A.K. Doerr, M. Tolan, T. Seydel, and W. Press. The interface structure of thin liquid hexane films. *Physica B*, 248:263–268, 1998. 5th International Conference on Surface X-Ray and Neutron Scattering (SXNS-5), Oxford, England, Jul 13-17, 1997.

[40] H. Dosch. Zukunftsbaustelle Photonenfabrik. *Spektrum der Wissenschaft*, 8:92, 2011. Interview.

[41] W. Doster, S. Busch, A.M. Gaspar, and H. Scheer. Dynamical transition of protein-hydration water. *Physical Review Letters*, 104(9):098101, 2010.

[42] W. Doster, S. Cusack, and W. Petry. Dynamical transition of myoglobin revealed by inelastic neutron-scattering. *Nature*, 337(6209):754–756, 1989.

[43] J. Dunkel. Relativ heiß. *Physik Journal*, 10:49, 2011.

[44] A. Einstein. Über die von der molekularkinetischen Theorie der Wärme geforderte Bewegung von in ruhenden Füssigkeiten suspendierten Teilchen. *Annalen der Physik (Leipzig)*, 17:549–560, 1905.

[45] A. Einstein. Über einen die Erzeugung und Verwandlung des Lichtes betreffenden heuristischen Gesichtspunkt. *Annalen der Physik*, 17:132–148, 1905.

[46] A. Einstein. Zur Elektrodynamik bewegter Körper. *Annalen der Physik*, 17:891–921, 1905.

[47] R.J. Ellis. Macromolecular crowding: an important but neglected aspect of the intracellular environment. *Current Opinion in Structural Biology*, 11(4):500, 2001.

[48] B. Farago. Recent developments and applications of NSE in soft matter. *Current Opinion in Colloid and Interface Science*, 14(6):391 – 395, 2009.

[49] A. Fick. On liquid diffusion. *Philosophical Magazine Series 4*, 10:30–39, 1855.

[50] G. Fleischer and F. Fujara. NMR as a generalized incoherent scattering experiment. In P. Diehl, E. Fluck, H. Günther, R. Kosfeld, and J. Seelig, editors, *NMR - Basic Principles and Progress*, volume 30, pages 159–207. Springer, Berlin, 1994.

[51] T. Franosch, M. Grimm, M. Belushkin, F.M. Mor, G. Foffi, L. Forró, and S. Jeney. Resonances arising from hydrodynamic memory in brownian motion. *Nature*, 478:85–88, 2011.

[52] B. Frick, H.N. Bordallo, T. Seydel, J.-F. Barthelemy, M. Thomas, D. Bazzoli, and H. Schober. How IN16 can maintain a world-leading position in neutron backscattering spectrometry. *Physica B - Condensed Matter*, 385-386(Part 2):1101–1103, 2006. 8th International Conference on Neutron Scattering, Sydney, Australia, Nov 27-Dec 02, 2005.

[53] B. Frick and M.A. Gonzalez. Five years operation of the second generation backscattering spectrometer IN16–a retrospective, recent developments and plans. *Physica B: Condensed Matter*, 301(1-2):8 – 19, 2001.

[54] B. Frick and A. Heidemann. Web Site for Neutron Backscattering Spectroscopy. http://www.ill.eu/sites/BS-review/index.htm.

[55] B. Frick, A. Magerl, Y. Blanc, and R. Rebesco. The new backscattering spectrometer IN16 at the ILL. *Physica B: Condensed Matter*, 234-236(0):1177 – 1179, 1997. Proceedings of the First European Conference on Neutron Scattering.

[56] B. Frick, E. Mamontov, L. van Eijck, and T. Seydel. Recent Backscattering Instrument Developments at the ILL and SNS. *Zeitschrift für Physikalische Chemie*, 224(1-2):33–60, 2010.

[57] H. Friedrich, V. Wagner, and P. Wille. A high-performance neutron velocity selector. *Physica B: Condensed Matter*, 156-157:547 – 549, 1989.

[58] F. Gabel, D. Bicout, U. Lehnert, M. Tehei, M. Weik, and G. Zaccai. Protein dynamics studied by neutron scattering. *Quarterly Reviews of Biophysics*, 35(4):327–367, 2002.

[59] E. Del Gado, A. Fierro, L. de Arcangelis, and A. Coniglio. A unifying model for chemical and colloidal gels. *Europhysics Letters*, 63(1):1, 2003.

[60] D.J. Gardiner. *Practical Raman spectroscopy*. Springer-Verlag Berlin, Heidelberg, 1989.

[61] F. González-Sánchez, F. Jurányi, T. Gimmi, L. Van Loon, T. Seydel, and T. Unruh. Dynamics of supercooled water in highly compacted clays studied by neutron scattering. *Journal of Physics - Condensed Matter*, 20(41):415102, 2008.

[62] J.M. Gosline, M.W. Denny, and M.E. Demont. Spider silk as rubber. *Nature*, 309(5968):551–552, 1984.

[63] G. Grübel, D.L. Abernathy, D.O. Riese, W.L. Vos, and G.H. Wegdam. Dynamics of dense, charge-stabilized suspensions of colloidal silica studied by correlation spectroscopy with coherent X-rays. *Journal of Applied Crystallography*, 33(3 Part 1):424–427, 2000.

[64] C. Gutt, T. Ghaderi, V. Chamard, A. Madsen, T. Seydel, M. Tolan, M. Sprung, G. Grübel, and S.K. Sinha. Observation of heterodyne mixing in surface x-ray photon correlation spectroscopy experiments. *Physical Review Letters*, 91(7):076104, 2003.

[65] C. Gutt, O. Leupold, and G. Grübel. Surface XPCS on nanometer length scales - What can we expect from an X-ray free electron laser? *Thin Solid Films*, 515(14):5532–5535, 2007. 9th International Conference on Surface X-Ray and Neutton Scattering, Taipei, Taiwan, 2006.

[66] W. Häußler, O. Holderer, T. Unruh, and J. Wuttke. High-Resolution Neutron Spectroscopy at the FRM II. *Neutron News*, 22(3):24–30, 2011.

[67] A. Heidemann. New methods in high resolution neutron spectroscopy. *Physica B: Condensed Matter*, 202(3-4):207 – 214, 1994.

[68] M. Heinen, F. Zanini, F. Roosen-Runge, D. Fedunová, F. Zhang, M. Hennig, T. Seydel, R. Schweins, M. Sztucki, M. Antalik, F. Schreiber, and G. Nägele. Viscosity and diffusion: Crowding and salt effects in protein solutions. *Soft Matter*, 8:1404, 2012.

[69] R. Hempelmann. *Quasielastic Neutron Scattering and Solid State Diffusion*. Clarendon Press, Oxford, 2000.

[70] M. Hennig. Phase Space Transformation. ILL report, Institut Laue Langevin, Grenoble, France, 2005.

[71] M. Hennig. *Dynamics of Globular Proteins in Crowded Electrolyte Solutions*. PhD thesis, University of Tübingen, Germany, and Institut Laue-Langevin, Grenoble, France, 2011. http://nbn-resolving.de/urn:nbn:de:bsz:21-opus-58803.

[72] M. Hennig, B. Frick, and T. Seydel. Optimum velocity of a phase space transformer for cold neutron backscattering spectroscopy. *Journal of Applied Crystallography*, 44:467–472, 2011.

[73] M. Hennig, F. Roosen-Runge, F. Zhang, S. Zorn, M.W.A. Skoda, R.M.J. Jacobs, T. Seydel, and F. Schreiber. Dynamics of highly concentrated protein solutions around the denaturing transition. *Soft Matter*, 8:1628, 2012.

[74] P.C. Hohenberg and B.I. Halperin. Theory of dynamic critical phenomena. *Reviews of Modern Physics*, 49(3):435 – 479, 1977.

[75] A. Hüller, M. Prager, W. Press, and T. Seydel. Phase III of solid methane: The orientational potential and rotational tunneling. *Journal of Chemical Physics*, 128(3):034503, 2008.

[76] Figures courtesy of the ILL drawing office.

[77] C. Ishimoto and T. Tanaka. Critical behavior of a binary mixture of protein and salt water. *Physical Review Letters*, 39(8):474–477, 1977.

[78] M. Jasnin, M. Moulin, M. Haertlein, G. Zaccai, and M. Tehei. Down to atomic-scale intracellular water dynamics. *EMBO reports*, 9:543–547, 2008.

[79] H. Jobic. Molecular motions in zeolites. *Spectrochimica Acta Part A: Molecular Spectroscopy*, 48(3):293 – 312, 1992.

[80] H. Jobic, A. Methivier, and T. Seydel. On the adsorption and diffusion of water in BaX zeolite. *Comptes Rendus Chimie*, 8(3-4):411–417, 2005.

[81] S. Khan. Free-electron lasers. *Journal of Modern Optics*, 55(21):3469–3512, 2008.

[82] O. Kirstein, T. Kozielewski, M. Prager, and D. Richter. Status of the high-flux backscattering spectrometer RSSM for the FRM-II reactor in Munich. *Applied Physics A - Materials Science & Processing*, 74(Part 1 Suppl. S):S133–S135, 2002.

[83] O. Kirstein, M. Prager, H. Grimm, and D. Richter. Design and optimisation of a backscattering spectrometer using a phase space transformation and super mirror guides. *Journal of Neutron Research*, 8:119–132, 1999.

[84] O. Kirstein, M. Prager, T. Kozielewski, and D. Richter. Phase space transformation used at the FRM II backscattering spectrometer: concepts and technical realization. *Physica B: Condensed Matter*, 283(4):361 – 364, 2000.

[85] J. Klafter and I.M. Sokolov. Anomalous diffusion spreads its wings. *Physics World*, pages 29–32, August 2005.

[86] G. Kneller and K. Hinsen. Fractional Brownian dynamics in proteins. *Journal of Chemical Physics*, 121:10278, 2004.

[87] W. Knoll. Neutronenstreuexperimente an Seidenfasern: Spektroskopische Untersuchung molekularer Bewegungen unter Zugbelastung und in Abhängigkeit des Feuchtigkeitsgehalts. Master's thesis, University of Kiel, Germany, and Institut Laue-Langevin, Grenoble, France, 2009.

[88] K. Kölln. *Morphologie und mechanische Eigenschaften von Zellulosefasern : Untersuchungen mit Röntgen- und Neutronenstreuung*. PhD thesis, University of Kiel, Germany, 2004.

[89] I. Krasnov, I. Diddens, N. Hauptmann, G. Helms, M. Ogurreck, T. Seydel, S.S. Funari, and M. Müller. Mechanical properties of silk: Interplay of deformation on macroscopic and molecular length scales. *Physical Review Letters*, 100(4):048104, 2008.

[90] P. Langevin. Sur la théorie du mouvement brownien. *Comptes-Rendus de l'Académie des Sciences*, 146:530–532, 1908.

[91] J.Z. Larese. Structure and dynamics of physisorbed phases. *Current Opinion in Solid State and Materials Science*, 2(5):539 – 545, 1997.

[92] J.Z. Larese, D. Martin y Marero, D.S. Sivia, and C.J. Carlile. Tracking the evolution of interatomic potentials with high resolution inelastic neutron spectroscopy. *Physical Review Letters*, 87(20):206102, 2001.

[93] P.-A. Lemieux and D.J. Durian. Investigating non-gaussian scattering processes by using nth-order intensity correlation functions. *Journal of the Optical Society of America A*, 16(7):1651–1664, 1999.

[94] K.D. Liss, A. Magerl, and W. Gläser. A neutron diffraction study on the very narrow dynamical width of GaAs(200). *Nuclear Instruments & Methods in Physics Research Section A*, 335(3):523–527, 1993.

[95] Y. Liu, L. Porcar, J. Chen, W.-R. Chen, P. Falus, A. Faraone, E. Fratini, K. Hong, and P. Baglioni. Lysozyme protein solution with an intermediate range order structure. *Journal of Physical Chemistry B*, 115:7238 – 7247, 2011.

[96] S.W. Lovesey. *Theory of neutron scattering from condensed matter*. Clarendon Press, Oxford, 1984.

[97] A. Madsen, T. Seydel, M. Sprung, C. Gutt, M. Tolan, and G. Grübel. Capillary waves at the transition from propagating to overdamped behavior. *Physical Review Letters*, 92(9):096104, 2004.

[98] A. Madsen, T. Seydel, M. Tolan, and G. Grübel. Grazing-incidence scattering of coherent X-rays from a liquid surface. *Journal of Synchrotron Radiation*, 12(6):786–794, 2005.

[99] H. Maier-Leibnitz. Grundlagen für die Beurteilung von Intensitäts- und Genauigkeitsfragen bei Neutronenstreumessungen. *Nukleonik*, 8(2):61, 1966.

[100] H. Maier-Leibnitz and T. Springer. The use of neutron optical devices on beam-hole experiments. *Journal of Nuclear Energy. Parts A/B. Reactor Science and Technology*, 17(4-5):217 – 225, 1963.

[101] E. Mamontov and K.W. Herwig. A time-of-flight backscattering spectrometer at the Spallation Neutron Source, BASIS. *Review of Scientific Instruments*, 82(8):085109, 2011.

[102] E. Mamontov, M. Zamponi, S. Hammons, W.S. Kaener, M. Hagen, and K.W. Herwig. BASIS: A New Backscattering Spectrometer at the SNS. *Neutron News*, 19(3):22–24, 2008.

[103] S. Mayer, H. Rauch, P. Geltenbort, P. Schmidt-Wellenburg, P. Allenspach, and G. Zsigmond. New aspects for high-intensity neutron beam production. *Nuclear Instruments and Methods in Physics Research Section A: Accelerators, Spectrometers, Detectors and Associated Equipment*, 608(3):434 – 439, 2009.

[104] G.B. McKenna. Confit III. Summary and perspectives on dynamics in confinement. *European Physical Journal - Special Topics*, 141:291 – 301, 2007.

[105] A. Meyer, R.M. Dimeo, P.M. Gehring, and D.A. Neumann. The high-flux backscattering spectrometer at the NIST Center for Neutron Research. *Review of Scientific Instruments*, 74(5):2759–2777, 2003.

[106] F. Mezei, editor. *Neutron Spin Echo , Lecture Notes in Physics , Vol. 128*. Springer, Berlin, 1980.

[107] L. Mlodinow. *The Drunkard's Walk: How Randomness Rules Our Lives*. Pantheon Books, New York, 2008.

[108] S.G.J. Mochrie, A.M. Mayes, A.R. Sandy, M. Sutton, S. Brauer, G.B. Stephenson, D.L. Abernathy, and G. Grübel. Dynamics of block copolymer micelles revealed by x-ray intensity fluctuation spectroscopy. *Physical Review Letters*, 78(7):1275–1278, 1997.

[109] A. Mourchid, A. Delville, J. Lambard, E. LeColier, and P. Levitz. Phase diagram of colloidal dispersions of anisotropic charged particles: Equilibrium properties, structure, and rheology of laponite suspensions. *Langmuir*, 11(6):1942–1950, 1995.

[110] M. Müller, C. Czihak, H. Schober, Y. Nishiyama, and G. Vogl. All disordered regions of native cellulose show common low-frequency dynamics. *Macromolecules*, 33(5):1834–1840, 2000.

[111] M. Müller, I. Krasnov, M. Ogurrek, M. Blankenburg, T. Pazera, and T. Seydel. Hierarchically structured biomaterials investigated *in situ* with x-ray and neutron scattering. *Advanced Engineering Materials (AEM)*, 13(8):767, 2011.

[112] C. Münster, T. Salditt, M. Vogel, R. Siebrecht, and J. Peisl. Nonspecular neutron scattering from highly aligned phospholipid membranes. *Europhysics Letters*, 46(4):486–492, 1999.

[113] G. Nägele. On the dynamics and structure of charge-stabilized suspensions. *Physics Reports*, 272(5-6):215 – 372, 1996.

[114] T. Narayanan. High brilliance small-angle x-ray scattering applied to soft matter. *Current Opinion in Colloid & Interface Science*, 14(6):409 – 415, 2009.

[115] J. Pérez, J.-M. Zanotti, and D. Durand. Evolution of the internal dynamics of two globular proteins from dry powder to solution. *Biophysical Journal*, 77:454 – 469, 1999.

[116] F. Perrin. Mouvement brownien d'un ellipsoide - I. Dispersion diélectrique pour des molécules ellipsoidales. *Journal de Physique Radium*, 5(10):497–511, 1934.

[117] F. Perrin. Mouvement brownien d'un ellipsoide (II). Rotation libre et dépolarisation des fluorescences. Translation et diffusion de molécules ellipsoidales. *Journal de Physique Radium*, 7(1):1–11, 1936.

[118] F. Pfeiffer, P. Hoghoj, I.S. Anderson, and V. Leiner. Neutron waveguides: a new neutron optical device for the production of submicrometer neutron beams. *Proceedings of SPIE*, 4509:79, 2001.

[119] T.K. Phillips, T. Bhinde, S.M. Clarke, S.Y. Lee, K.S. Mali, and S.D. Feyter. Adsorption of aldehydes on a graphite substrate: Combined thermodynamic study of C6-C13 homologues with a structural and dynamical study of dodecanal. *The Journal of Physical Chemistry C*, 114(13):6027–6034, 2010.

[120] R. Piazza. Protein interactions and association: an open challenge for colloid science. *Current Opinion in Colloid & Interface Science*, 8(6):515–522, 2004.

[121] M.-O.M. Piepenbrock, G.O. Lloyd, N. Clarke, and J.W. Steed. Gelation is crucially dependent on functional group orientation and may be tuned by anion binding. *Chemical Communications*, 23:2644–2646, 2008.

[122] L. Porcar, P. Falus, W.-R. Chen, A. Faraone, E. Fratini, K. Hong, P. Baglioni, and Y. Liu. Formation of the dynamic clusters in concentrated lysozyme protein solutions. *The Journal of Physical Chemistry Letters*, 1(1):126–129, 2010.

[123] M. Prager and A. Heidemann. Rotational tunneling and neutron spectroscopy: A compilation. *Chemical Reviews*, 97(8):2933–2966, 1997.

[124] M. Prager, A. Pietraszko, L. Sobczyk, A. Pawlukojc, E. Grech, T. Seydel, A. Wischnewski, and M. Zamponi. X-ray diffraction and inelastic neutron scattering study of 1 : 1 tetramethylpyrazine chloranilic acid complex: temperature, isotope, and pressure effects. *Journal of Chemical Physics*, 125(19):194525, 2006.

[125] E.M. Purcell. Life at low reynolds number. *American Journal of Physics*, 45(1):3, 1977.

[126] J. Qvist, H. Schober, and B. Halle. Structural dynamics of supercooled water from quasielastic neutron scattering and molecular simulations. *Journal of Chemical Physics*, 134(14):144508, 2011.

[127] O.G. Randl, H. Franz, T. Gerstendörfer, W. Petry, G. Vogl, and A. Magerl. How to rejuvenate an old lady: New crystals for the backscattering spectrometer IN10. *Physica B: Condensed Matter*, 234-236:1064 – 1065, 1997. Proceedings of the First European Conference on Neutron Scattering.

[128] O. Rathore and D.Y. Sogah. Nanostructure Formation through β-Sheet Self-Assembly in Silk-Based Materials. *Macromolecules*, 34(5):1477–1486, 2001.

[129] M.C. Rheinstädter, J. Das, E.J. Flenner, B. Brüning, T. Seydel, and I. Kosztin. Motional Coherence in Fluid Phospholipid Membranes. *Physical Review Letters*, 101(24):248106, 2008.

[130] M.C. Rheinstädter, T. Seydel, F. Demmel, and T. Salditt. Molecular motions in lipid bilayers studied by the neutron backscattering technique. *Physical Review E*, 71(6):061908, 2005.

[131] M.C. Rheinstädter, T. Seydel, B. Farago, and T. Salditt. Probing dynamics at interfaces: options for neutron and x-ray spectroscopy. *Journal of Neutron Research*, 14(3):257–268, 2006.

[132] M.C. Rheinstädter, T. Seydel, and T. Salditt. Nanosecond molecular relaxations in lipid bilayers studied by high energy-resolution neutron scattering and in situ diffraction. *Physical Review E*, 75(1, Part 1):011907, 2007.

[133] H. Risken. *The Fokker-Planck-Equation. Methods of Solution and Applications*. 2nd edition. Springer-Verlag Berlin, Heidelberg, 1989.

[134] F. Roosen-Runge, M. Hennig, T. Seydel, F. Zhang, M.W.A. Skoda, S. Zorn, R.M.J. Jacobs, M. Maccarini, P. Fouquet, and F. Schreiber. Protein diffusion in crowded electrolyte solutions. *Biochimica et Biophysica Acta - Proteins and Proteomics*, 1804(1):68–75, 2010.

[135] F. Roosen-Runge, M. Hennig, F. Zhang, R.M.J. Jacobs, M. Sztucki, H. Schober, T. Seydel, and F. Schreiber. Protein Self-Diffusion in Crowded Solutions. *Proceedings of the National Academy of Sciences (USA)*, 108:11815, 2011.

[136] J. Rubio Retama, B. Frick, T. Seydel, M. Stamm, A. Fernandez Barbero, and E. Lopez Cabarcos. Polymer chain dynamics of core-shell thermosensitive microgels. *Macromolecules*, 41(13):4739–4745, 2008.

[137] D. Russo, J. Pérez, J.-M. Zanotti, M. Desmadril, and D. Durand. Dynamic transition associated with the thermal denaturation of a small beta protein. *Biophysical Journal*, 83:2792, 2002.

[138] D. Sapede, T. Seydel, V.T. Forsyth, M.M. Koza, R. Schweins, F. Vollrath, and C. Riekel. Nanofibrillar structure and molecular mobility in spider dragline silk. *Macromolecules*, 38(20):8447–8453, 2005.

[139] J. Schelten and B. Alefeld. Backscattering Spectrometer with Adapted Q-Resolution at the Pulsed Neutron Source. In R. Scherm and H.H. Stiller, editors, *Proceedings of the Workshop on Neutron Scattering Instrumentation for SNQ*, volume Jül-1954, page 378. Kernforschungsanlage Jülich, 1984.

[140] F. Schreiber, F. Roosen-Runge, R.M.J. Jacobs, M.W.A. Skoda, F. Zhang, M.Hennig, and T. Seydel. Report on experiment LTP 9-3. Technical report, ILL experimental report, 2011. http://club.ill.fr.

[141] V.F. Sears. Bragg reflection in mosaic crystals .1. General solution of the Darwin equations. *Acta Crystallographica Section A*, 53:35–45, 1997a.

[142] V.F. Sears. Bragg reflection in mosaic crystals .2. Neutron monochromator properties. *Acta Crystallographica Section A*, 53:46–54, 1997b.

[143] T. Seydel, W. Knoll, I. Greving, C. Dicko, M.M. Koza, I. Krasnov, and M. Müller. Increased molecular mobility in humid silk fibers under tensile stress. *Physical Review E*, 83(1):016104, 2011.

[144] T. Seydel, K. Kölln, I. Krasnov, I. Diddens, N. Hauptmann, G. Helms, M. Ogurreck, S.-G. Kang, M.M. Koza, and M. Müller. Silkworm silk under tensile strain investigated by synchrotron X-ray diffraction and neutron spectroscopy. *Macromolecules*, 40(4):1035–1042, 2007.

[145] T. Seydel, A. Madsen, M. Sprung, M. Tolan, G. Grübel, and W. Press. Setup for in situ surface investigations of the liquid/glass transition with (coherent) x rays. *Review of Scientific Instruments*, 74(9):4033–4040, 2003.

[146] T. Seydel, A. Madsen, M. Tolan, G. Grübel, and W. Press. Capillary waves in slow motion. *Physical Review B*, 63(7):073409, 2001.

[147] T. Seydel, M. Tolan, B.M. Ocko, O.H. Seeck, R. Weber, E. DiMasi, and W. Press. Freezing of capillary waves at the glass transition. *Physical Review B*, 65(18):184207, 2002.

[148] T. Seydel, L. Wiegart, F. Juranyi, B. Struth, and H. Schober. Unaffected microscopic dynamics of macroscopically arrested water in dilute clay gels. *Physical Review E*, 78(6, Part 1):061403, 2008.

[149] A. Shome, S. Debnath, and P.K. Das. Head group modulated pH-responsive hydrogel of amino acid-based amphiphiles: Entrapment and release of cytochrome c and vitamin B12. *Langmuir*, 24(8):4280–4288, 2008.

[150] I. Sikharulidze, B. Farago, I.P. Dolbnya, A. Madsen, and W.H. de Jeu. Surface and bulk elasticity determined fluctuation regimes in smectic membranes. *Physical Review Letters*, 91(16):165504, 2003.

[151] K.S. Singwi and A. Sjölander. Diffusive motions in water and cold neutron scattering. *Physical Review*, 119(3):863–871, 1960.

[152] T.L. Spehr, B. Frick, M. Zamponi, and B. Stühn. Dynamics of water confined to reverse AOT micelles. *Soft Matter*, 7:5745–5755, 2011.

[153] M. Sprung, T. Seydel, C. Gutt, R. Weber, E. DiMasi, A. Madsen, and M. Tolan. Surface roughness of supercooled polymer melts. *Physical Review E*, 70(5):051809, 2004.

[154] G.L. Squires. *Introduction to the theory of thermal neutron scattering*. Dover, Mineola, NY, 1978.

[155] A.M. Stadler, I. Digel, G.M. Artmann, J.P. Embs, G. Zaccai, and G. Büldt. Hemoglobin dynamics in red blood cells: Correlation to body temperature. *Biophysical Journal*, 95:5449, 2008.

[156] L. Stagg, S.-Q. Zhang, M.S. Cheung, and P. Wittung-Stafshede. Molecular crowding enhances native structure and stability of alpha/beta protein flavodoxin. *Proceedings of the National Academy of Sciences (USA)*, 104(48):18976–18981, 2007.

[157] A. Stradner, H. Sedgwick, F. Cardinaux, W.C.K. Poon, S.U. Egelhaaf, and P. Schurtenberger. Equilibrium cluster formation in concentrated protein solutions and colloids. *Nature*, 432:492 – 495, 2004.

[158] B. Struth, A. Vorobiev, T. Seydel, L. Wiegart, and J. Major. A neutron scattering study of hydrogel surfaces. *Physica B - Condensed Matter*, 350(1-3, Suppl. 1):E917–E919, 2004.

[159] J. Swenson, D. Engberg, W.S. Howells, T. Seydel, and F. Juranyi. Dynamics of propylene glycol and its oligomers confined to a single molecular layer. *Journal of Chemical Physics*, 122(24):244702, 2005.

[160] J. Teixeira, M.C. Bellissent-Funel, S.H. Chen, and A.J. Dianoux. Experimental determination of the nature of diffusive motions of water molecules at low temperatures. *Physical Review A*, 31(3):1913–1917, 1985.

[161] M.T.F. Telling, C. Neylon, S.H. Kilcoyne, and V. Arrighi. Anharmonic behavior in the multisubunit protein apoferritin as revealed by quasi-elastic neutron scattering. *Journal of Physical Chemistry B*, 112(35):10873–10878, 2008.

[162] T. Thurn-Albrecht, W. Steffen, A. Patkowski, G. Meier, E.W. Fischer, G. Grübel, and D.L. Abernathy. Photon correlation spectroscopy of colloidal palladium using a coherent x-ray beam. *Physical Review Letters*, 77(27):5437–5440, 1996.

[163] Y. Tian, M.M. Martinez, and D. Pappas. Fluorescence Correlation Spectroscopy: A Review of Biochemical and Microfluidic Applications. *Applied Spectroscopy*, 65(4):115A–124A, 2011.

[164] M. Tokuyama and I. Oppenheim. Dynamics of hard-sphere suspensions. *Physical Review E*, 50(1):R16–R19, 1994.

[165] M. Tolan, T. Seydel, A. Madsen, G. Grübel, W. Press, and S.K. Sinha. Investigation of surface dynamics on micro- and nanometer scales. *Applied Surface Science*, 182(3-4):236 – 243, 2001.

[166] J.T. Trevors and G.H. Pollack. Hypothesis: the origin of life in a hydrogel environment. *Progress in Biophysics and Molecular Biology*, 89:1, 2005.

[167] L. van Eijck, L. Gérard, B. Frick, T. Seydel, and H. Schober. A case study for using backscattering instruments at reactors in inverted time-of-flight mode. *Nuclear Instruments and Methods in Physics Research Section A*, 672:64–68, 2012.

[168] L. Van Hove. Correlations in space and time and born approximation scattering in systems of interacting particles. *Physical Review*, 95(1):249–262, 1954.

[169] H. Van Olphen. Rheological phenomena of clay sols in connection with the charge distribution on the micelles. *Discussions of the Faraday Society*, 11:82–84, 1951.

[170] G.H. Vineyard. Scattering of slow neutrons by a liquid. *Physical Review*, 110(5):999, 1958.

[171] F. Volino and A.J. Dianoux. Neutron incoherent-scattering law for diffusion in a potential of spherical symmetry – General formalism and application to diffusion inside a sphere. *Molecular Physics*, 41(2):271–279, 1980.

[172] F. Vollrath and D.P. Knight. Liquid crystalline spinning of spider silk. *Nature (London)*, 410(6828):541 – 548, 2001.

[173] M. von Smoluchowski. Über Brownsche Molekularbewegung unter Einwirkung äußerer Kräfte und den Zusammenhang mit der verallgemeinerten Diffusionsgleichung. *Annalen der Physik (Leipzig)*, 353:1103–1112, 1915.

[174] V. Wagner, H. Friedrich, and P. Wille. Performance of a high-tech neutron velocity selector. *Physica B: Condensed Matter*, 180-181(Part 2):938 – 940, 1992.

[175] L. Wiegart, P. Terech, C. Caronna, A. Duri, and T. Seydel. Report on experiment 9-10-973 on IN6 and IN16. Technical report, ILL experimental report, 2009. http://club.ill.fr.

[176] M.K. Wilkinson. Early history of neutron scattering at Oak Ridge. *Physica B+C*, 137(1-3):3 – 16, 1986.

[177] M. Wolff, B. Frick, A. Magerl, and H. Zabel. Flow cell for neutron spectroscopy. *Physical Chemistry Chemical Physics*, 7(6):1262–1265, 2005. 7th International Conference on Quasi-Elastic Neutron Scattering, Arcachon, France, 2004.

[178] G. Zaccai. Biochemistry - How soft is a protein? A protein dynamics force constant measured by neutron scattering. *Science*, 288(5471):1604–1607, 2000.

[179] F. Zhang, R. Roth, M. Wolf, F. Roosen-Runge, M.W.A. Skoda, R.M.J. Jacobs, M. Stzucki, and F. Schreiber. Charge-controlled metastable liquid-liquid phase separation in protein solutions as a universal pathway towards crystallization. *Soft Matter*, 8:1313, 2012.

[180] F. Zhang, M.W.A. Skoda, R.M.J. Jacobs, S. Zorn, R.A. Martin, C.M. Martin, G.F. Clark, S. Weggler, A. Hildebrandt, O. Kohlbacher, and F. Schreiber. Reentrant condensation of proteins in solution induced by multivalent counterions. *Physical Review Letters*, 101(14):148101, 2008.

[181] F. Zhang, S. Weggler, M.J. Ziller, L. Ianeselli, B.S. Heck, A. Hildebrandt, O. Kohlbacher, M.W.A. Skoda, R.M.J. Jacobs, and F. Schreiber. Universality of protein reentrant condensation in solution induced by multivalent metal ions. *Proteins: Structure, Function, and Bioinformatics*, 78(16):3450–3457, 2010.

[182] F. Zhang, G. Zocher, A. Sauter, T. Stehle, and F. Schreiber. Novel approach to controlled protein crystallization through ligandation of yttrium cations. *Journal of Applied Crystallography*, 44:755, 2011.

[183] B.H. Zimm and J.K. Bragg. Theory of the phase transition between helix and random coil in polypeptide chains. *Journal of Chemical Physics*, 31(2):526–535, 1959.

[184] R. Zorn, M. Mayorova, D. Richter, and B. Frick. Inelastic neutron scattering study of a glass-forming liquid in soft confinement. *Soft Matter*, 4:522–533, 2008.

Acknowlegdement

I have had the privilege to work in and with several different teams during the past eleven years at the ILL, and I would like to thank all teams for the very enjoyable spirit. This brief acknowledgement of course cannot mention everyone I am indebted to individually. In the time-of-flight/high-resolution group I would like to thank the group leaders Hannu Mutka, Helmut Schober, and José Dianoux, as well as my backscattering colleagues Bernhard Frick, Lambert van Eijck, Miguel Gonzalez, and Jérome Combet. In the IN16B instrument team scientifically led by Bernhard Frick, it was a pleasure to collaborate with Heloisa Nũnes Bordallo on instrument simulations during the year 2004/2005. The many IN16B technical and design meetings were always chaired by David Bazzoli and inspired a perfect exchange between the abstract side of numerical simulations of the neutron optics and the engineering "real-world" aspects of the project. Important interactions with Michael Kreuz, Emmanuel Farhi, Stéphane Fuard, and Roland Gähler led to a deeper understanding of the ILL's cold moderator neutron sources and successful implementation of the double-ballistic neutron guide H112 serving IN16B. I am also indebted to Michael Prager for many stimulating discussions on science and instrumentation. I am very grateful to the instrument technicians Paul Joubert, Matthias Elender, Roger Chung, and Richard Ammer, as well as to the TOF/HR-engineer Jean-François Barthélémy.

I would like to thank the students who worked with me at the ILL. The students' research projects have particularly strengthened the very enjoyable collaborations with partner universities, including Kiel, Göttingen, Tübingen and Oxford, as well as with the ESRF. Notably, I express my gratitude to the PhD students Daniel Sapède and Marcus Hennig who carried out their research at the ILL. Further, I would like to thank the Diploma students who carried out part of their thesis work at the ILL, namely Wiebke Knoll, Fabio Zanini, Felix Roosen-Runge, Elena Jordan, and Daniel Soraruf. I am equally grateful to the ILL summer students who worked with me, namely Claas Behrend, Lutz Wiegart, Onno Kortmann, Martin Göppl, Shin-Gyu Kang, Marcus Hennig, Suzanne Hamilton, Tobias Reusch, Andreas Russek, and Henrik Jacobsen.

The science at the ILL vitally depends on strong outside collaborations, and I am particularly grateful to the groups of Tim Salditt (Göttingen), Frank Schreiber (Tübingen), and Martin Müller (Kiel and Helmholtz-Zentrum Geesthacht) for continued collaborations during many years and the hospitality of the groups during my visits. I have had the privilege to be a guest of the Institute for X-ray Physics in Göttingen during several months in 2005/2006 and again in early 2008 and to participate in the lecture on "Scattering methods in soft condensed matter and biophysics". At the Universities of Kiel and Tübingen I am particularly indebted to the machine shop teams. They built the tensile machine with the humidity chamber (Kiel), as well as the crystostat center stick for optical spectroscopy and a very large number of sample holders (Tübingen). In Tübingen, I would further like to acknowledge the scientific project leader for proteins in solution, Fajun Zhang, as well as Klaus Hagdorn for technical support and logistics. I also thank the Tübingen group for the hospitality during the Oberjoch Klausurtagungen. At the ESRF, I would like to acknowledge Anders Madsen, Gerhard Grübel, Christian Riekel, Bernd Struth, and Lutz Wiegart for pleasant collaborations profiting from the neighbourhood of the ESRF and ILL on the joint European Photon and Neutron Science campus. Pleasant scientific collaborations on lipid membranes are active with the group of Maikel Rheinstädter (McMaster University). I also would like to thank John Larese (University of Tennessee) for the very enjoyable transatlantic collaboration which gave us the opportunity for many experiments and discussions on both sides of the ocean.